Nanometal inks for plastic electronics applications

Bibin Thomas Anto

In partial fulfillment of the requirements for the

Degree of Master of Science

Department of Physics

National University of Singapore

2010

For Bimal & family

For Nitha

Acknowledgments

First and foremost, I take immense pleasure to thank God as He never let me down throughout my life, especially during the last 2.5 years as graduate student in National University of Singapore. Secondly, I thank Dr Peter Ho for admitting myself as his full student in Organic Nano Device Lab (ONDL). I am grateful to Peter for his support and guidance throughout my tenure in ONDL, where the work described in this thesis has been performed. I also thank him for the financial assistance that he has provided during my stay at ONDL. My sincere gratitude to Dr Lay-Lay Chua for her assistance that helped me to carryout the chemistry aspects of my work at ease.

I want to thank Sivaramakrishnan, who helped me in settling down on initial stage my work at ONDL. I thank all the members of ONDL for making this period of my life more memorable and colourful. Finally, I am grateful to my family for their extensive support throughout my life and for their prayers.

Abstract

In order to use metal nanoparticle (NP) films in printable electronics applications, they have to be annealed to eliminate the protective monolayer ligand shell or displace the polymeric dispersant to effect coalescence to a nanocrystalline “bulk-like” continuous film. We demonstrate here a new concept of sparse monolayer protection of these metal NPs by ω-ionic functionalised alkylthiol ligands that offer both high water and alcohol solubility; and low coalescence temperature ($T_p \approx$ 145ºC for Au and 155ºC for Ag, which is the lowest reported sintering temperature to date) at the same time. This allows, for example, both Au and Ag NP films to be coalesced to continuous metallic films with conductivity near half the value of the bulk metal after only brief annealing (few min) at this temperature, far shorter than that required for commercial systems. This method is, therefore, compatible with commercially available plastic substrates that are sensitive to temperature and organic solvents. Detailed study by Fourier transform infrared spectroscopy reveals that the coalescence of metal nano-cores is not due to thermodynamic size effects on melting as widely speculated in the literature, but dominated by desorption of protective ligands. This therefore allows the possibility to control the insulator-to-metal transformation without restriction on NP size.

In chapter 1, we summarize about the present nanometal ink technologies and their potential applications in plastic electronics circuits, which forms the background for this thesis work.

In chapter 2, we describe several aspects of metal nanoparticle (NP) systems and their design considerations such as optimal core diameter, summary of the known methods of production /

synthesis, insulator to metal transformation temperature and epigrammatic picture of optical properties of these nanometals.

In chapter 3, we describe the evidence of sparse ionic monolayer ligand shell assembly on Au NP inks and controlled preparation methodology of sparse monolayer protected metal NPs by detailed analysis of Fourier transform infrared spectroscopy (FTIR), together with X-ray photoelectron spectroscopy, which shows the sparse monolayer protected NP systems have only 25% monolayer density of conventional NPs.

In chapter 4, we demonstrate the T_p value of 145ºC for sparse monolayer protected Au NP fims from the electrical conductivity measurements. The generality of this principle is further demonstrated by showing the similar T_p transformation in Ag NP films. We discuss the ligand shell transformation of metal NP films with respect to anneal temperature using FTIR spectroscopy. Effects of ligand shell structure on the T_p of metal NP films are discussed in detail.

In chapter 5, we address an aspect of core-core coalescence on monolayer protected metal NP films. We show that, contrary to frequent assertion in the literatures, the coalescence of metal NPs are not due to the thermodynamic size effect and surface melting. The evidence came from the invariance of T_p in NPs of different core diameter and same ligand shell protection. The coalescence is dominated by the ligand desorption process, immediately followed by the cold-neck formation between the adjacent nanocores due to surface diffusion of atoms. We further discuss this picture with differential scanning calorimetry of metal NPs, which shows the clear evidence of desorption of ligand shell at T_p.

TABLE OF CONTENTS

1 Introduction

1.1 Background

1.1.1 Plastic electronics

Plastic electronics has drawn much attention since the discovery of electroluminescence in conjugated polymers,[1, 2] Further understanding of science behind the device operations[3, 4] and subsequent developments advanced this technology to a stage viable for commercial applications such as organic light emitting diodes (OLEDs) and Organic Photovoltaics (OPVs). This technology offers potential opportunities to take the electronics to the places, where silicon is unable to go, including flexible plastics, paper and fabric.[5-9] The simplicity of solution processability makes plastic electronics attractive compared to conventional semiconductor devices, which demands complex vacuum and high-temperature processes. Relatively inexpensive printing methodologies, especially inkjet printing,[10-15] of electronic circuits using semiconducting polymer inks open-up the possibility of bringing the technology to its next level to large volume roll-to-roll (R2R) manufacturing.[16] This enables fast and continuous printing of electronic devices such as organic field effect transistors (OFETs), OLEDs, OPVs, and radio frequency identification (RFID) tags onto flexible plastic substrates on a large volume.

The key requirements for the printing of polymer electronic circuits revolves around the appropriate material systems such as printable highly conductive electrodes, efficient hole-injection layers such as poly(3,4-ethylenedioxythiophene):poly(styrenesulfonic acid) (PEDT:PSS), and novel conjugated polymer systems with desired functional properties depends on the applications. This can then be integrated onto appropriate processing methodologies with suitable solvent and thermal characteristics.

1.1.2 Metal nanoparticle films as electrodes

Numerous applications have been envisaged for printable metal NP films: as low–cost ambient–processed metal films for chemobiomolecular sensors,[17] microelectromechanical systems,[11] functional nanostructures,[18] and as catalysts,[19] and electrodes or interconnects in plastic electronic circuits.[20-23] Current-carrying interconnects in polymer semiconductor integrated circuits, [13, 24, 25] require a minimum dc conductivity (σ_{dc}) of the order of 10^4 S cm^{-1} to avoid severe resistive losses. The conductive polymers have reported a maximum $\sigma_{dc} \approx$ 10–100 S cm^{-1} hence not suitable for these applications. Conventional metal and graphite paints will not be suitable as they re-disperse during the solvent processing of organic circuit processing. Metallic electrical conductors are ubiquitous in all types of electrical devices and circuits. They serve as interconnects for the transport of electrical signal and power, electrodes in capacitors, resistors and diodes (including OLEDs and OPVs), antennas in RFID tags, mechanical structures and optical parts in microelectromechanical (MEMS) systems and buffer or barrier layers for a myriad of other applications.

Suitable metals include gold (Au), silver (Ag), copper (Cu), aluminum (Al), nickel (Ni), palladium (Pd), platinum (Pt) and others and their alloys depending on the application and the performance required. For example, Ag is widely thought to be suitable for RFID antennae and metal tracking applications in general, but Au which is chemically more inert is likely to be indispensable as the source–drain electrodes in OFETs and applications that cannot tolerate electrochemical oxidation, corrosion or ion formation at the metal surface.

1.2 Motivation

Although the future for plastic electronics looks promising, a lot of developments need to be done in order to realize the technology in commercial applications.[26, 27] There are numerous advantages to have the ability to deposit high-quality metal lines by printing, rather than by evaporation, lithography and etching processes, or electrochemical deposition or electroless plating that underpin much of the metal thin film and silicon industries. Printing, whether by inkjet, gravure, offset, screen or other forms, provides the possibility to deliver materials to the desired location over large, highly scalable, possibly flexible surfaces on a variety of substrates including plastics.[28] This is an inherently more effective use of materials, and the manufacturing process is environmentally greener and more energy-efficient than traditional lithography and etching. More importantly this also opens new niche applications not accessible by conventional technologies. For metallization, the obvious source is metal particles protected by a dispersant coating (referred here also as the ligand shell) typically of a self-assembled monolayer, and optionally admixed with a polymer binder. This derives from long-standing interests in metal nanoparticles (NPs), in particular for their optical properties. It has recently been considered very attractive to print such films or tracks of metal particles in the ambient at room temperature and then eliminate the protecting ligand shell in a subsequent annealing (or coalescence) step to give sintered continuous thin films with bulk-like metallic properties. The essential requirement for such applications is a high electrical conductivity, resistant to electromigration and electrochemical corrosion, and process compatibility with the substrate and underlayers and with the formation of the subsequent overlayers. Additionally, the metallization should be able to inject charge carriers efficiently into the semiconductor if used in those applications. For example nano-Ag inks are already available from several commercial sources, including Cabot, Nippon, Harima Chemical Inc.[29] Some of these

are large NPs (50-nm-diameter) protected by a 5-nm-thick polymeric dispersant (usually polyvinyl pyrrolidone or polyvinyl alcohol) which can be coalesced through long annealing in air at low temperatures (1 h at > 150ºC) to "burn-off" the dispersant, or more quickly at elevated temperatures (several min at > 220–260ºC) to reach one-tenth of the bulk conductivity (σ_{dc}) of Ag.[30-33] Temperatures > 300ºC are required to approach one-half of σ_{dc} of bulk-Ag. The use of molecular rather than polymeric dispersants is expected to provide finer control over the characteristics of NPs, and hence provide considerable scope to further develop metal NPs for high-end plastic electronics applications greatly beyond the use of micron-sized metal particles as screen-printed conductors.

Despite the widespread optimism, detailed investigations of the properties (optical, electrical and mechanical) of films of densely-packed metal NPs, and their insulator–to–metal transformation have begun only recently. In fact the challenges to combine certain key materials properties, such as of high particle dispersibility in solvents but low coalescence temperature (< 300ºC) are only beginning to be addressed.

1.3 Overview of metal NP films

These metal NP films, in contrast to those of conventional metal pastes, are initially formed as an insulating film because the metal NPs are each encapsulated by a monolayer (typically 1-nm-thick for molecular ligands and up to 5-nm-thick for polymeric ligands) of usually an insulating molecule.[34, 35] During thermal annealing, this protection monolayer is disrupted and removed by volatilization, which then allows some bare patches of the metal NPs to come into contact with neighboring NPs to develop "cold necks" that join these NPs into a metallic conduction network. When the volume fraction of the network exceeds the percolation limit, the dc electrical conductivity

(σ_{dc}) shows a sharp rise.[23] Further annealing can bring this σ_{dc} to within a factor of 2 of the bulk conductivity of the metal, even though the final morphology of the film comprises of nanocrystal domains, different from bulk metals. To distinguish between the first-formed film and the final annealed film, we shall refer to the first as metal NP films and the final as NP metal films. Therefore it is this cold "necking" that develops between metal NPs when they come into contact through the elimination of their protection monolayer and not their bulk or surface melting that is responsible for the sintering of the metal NP films to the desired NP metal films, and hence central to the science and technology of these materials. Surface diffusion[36] therefore plays a key role in controlling the transformation characteristics and properties of the resultant NP metal film. This implies that the final film is nanocrystalline in morphology with vestiges of the domains and orientations of the NPs in the first-deposited, metal NP films. From a technological perspective, this is very interesting as it implies the percolation temperature can be much lower than the core or surface thermodynamic melting temperatures of the NPs, which themselves are depressed from the bulk values, and unlike these thermodynamic values, does not have to depend on NP radius.

1.4 Advantages of nanometal inks over traditional metal pastes

Stable metal pastes of Ag, Au and Pt have been available for some time as electrically conductive adhesives. These typically comprise micron-sized metal flakes protected by a dispersant (typically a surfactant material such as long-chain thiols or carboxylic acids) and dispersed at a volume fraction of > 50% in a polymer binder and diluted in an organic solvent for deposition. The dried films can have conductivities up to a few 10^4 S cm^{-1} which is limited by the relatively poor physical contacts between the metal flakes. Recently, increasing efforts have been dedicated to developing nanometal inks comprising ligand-shell stabilized metal nanoparticles (NP) in the 2–100-nm dia.

size range for use in printed electronics. Alternative names for these NPs are “colloids” and “nanocrystals”, which are less accurate as these NPs are smaller than conventional colloids, and are not necessarily formed in the completely crystalline state. Like the metal pastes, these NPs are also protected by a dispersant which may be a molecular material in the form of a protective ligand shell of a self-assembled monolayer, or a polymeric material. Unlike metal pastes, metal NPs can be used “pure” without any admixed polymeric binder, because the molecular-scale ligand shell on these metal NPs which are formed during the synthesis of the NPs impart sufficient thermodynamic stability to the dispersed NPs (i.e., they can remain permanently suspended under earth’s gravity) and repeatedly precipitated using a bad solvent and redispersed at will without requiring agitation or ultra-sonication.

These metal NPs have several crucial advantages over the traditional metal pastes that make them suitable candidates for metallization in advanced technologies:

(i) The attainable conductivity in NP metal films is considerably higher than from micron-sized metal pastes (10^4 S cm^{-1}) and closer to the bulk conductivity (> 10^5 S cm^{-1}) of the macroscopic metal films because good inter-particle contact is achieved by a subsequent relatively low-temperature NP coalescence process.

(ii) The final mechanical strength of the film comes from this cold sintering of the metal NPs, rather than from an admixed polymeric binder.

(iii) The achievable critical dimension line width is considerably better because of the smaller size of these NPs. This is particularly important in metal thin film applications (film thickness < 1 μm), for example as electrodes which are sensitive to resultant surface topography, as distinct from metal thick film applications (film thickness 1-100

μm, line width 50–1000 μm) such as bus lines, antennae, and power interconnects. Clearly one cannot in general have particle sizes much larger than about one-tenth of the intended final film thickness to avoid large attendant film microroughness.

(iv) Metal NPs can be formulated more readily with advanced dispersant and binders that are more compatible with the requirements of electronics. More crucially the binder can be selected advantageously to impart the desired functionality to the metal film, for example to modify the surface of the resultant metal NP film to give improved wettability or charge carrier injection.

1.5 Reference

1. Burroughes, J.H., D.D.C. Bradeley, A.R. Brown, R.N. Marks, K. Mackay, R.H. Friend, P.L. Burns, A.B. Holmes, *Light-emitting diodes based on conjugated polymers.* Nature, 1990. 347: p. 539-541.
2. Friend, R.H., R.W. Gymer, A.B. Holmes, J.H. Burroughes, R.N. Marks, C. Taliani, D.D.C. Bradley, D.A. Dos Santos, J.L. Brédas, M. Lögdlund & W.R. Salaneck, *Electroluminescence in conjugated polymers.* Nature, 1999. 397: p. 121-128.
3. Burroughes, J.H., C.A. Jones, and R.H. Friend, *New semiconductor device physics in polymer diodes and transistors.* Nature, 1988. 335: p. 137-141.
4. Sirringhaus, H., *Device physics of solution-processed organic field-effect transistors.* Adv. Mater., 2005. 17: p. 2411–2425.
5. Crawford, G.P., *Flexible Flat Panel Displays*. Wiley-SID Series in Display Technology, ed. A.C. Lowe. 2005: John Wiley & Sons, Ltd.
6. Whitmarsh, J., *Flexible electronics: silicon meets paper and beyond.* Microelectron. Int., 2005. 22: p. 16-19.
7. Choi, M.C., Y. Kim, and C.S. Ha, *Polymers for flexible displays: from material selection to device applications.* Prog. Polym. Sci., 2008. 33: p. 581-630.
8. Gustafsson, G., Y. Cao, G.M. Treacy, F. Klavetter, N. Colaneri and A.J. Heeger, *Flexible light-emitting diodes made from soluble conducting polymers.* Nature, 1992. 357: p. 477 - 479.
9. Yoshida, A., A. Sugimoto, T. Miyadera, S. Miyaguchi, *Organic light emitting devices on polymer substrates.* J. Photopolym. Sci. Technol., 2001. 14: p. 327 - 332.
10. Cheng, K., M.H. Yang, W.W.W. Chiu, C.Y. Huang, J. Chang, T.F. Ying, Y. Yang, , *Ink-jet printing, self-assembled polyelectrolytes, and electroless plating: low cost fabrication of circuits on a flexible substrate at room temperature.* Macromol. Rapid Commun., 2005. 26: p. 247 - 264.
11. Fuller, S.B., E.J. Wilhelm, and J.M. Jacobson, *Ink-jet printed nanoparticle microelectromechanical systems.* J. Microelectromech. Syst., 2002. 11: p. 54 - 60.
12. Kamyshny, A., M. Ben-Moshe, S. Aviezer, S. Magdassi, Ink-jet printing of metallic *nanoparticles and microemulsions.* Macromol. Rapid Commun., 2005. 26: p. 281 - 288.
13 Sirringhaus, H., T. Kawase, R.H. Friend, T. Shimoda, M. Inbasekaran, W. Wu and E. P. Woo, *High-resolution ink-jet printing of all-polymer transistor circuits.* Science, 2000. 290: p. 2123 - 2126.
14. Tekin, E., B.J. de Gans, and U.S. Schubert, *Ink-jet printing of polymers – from single dots to thin film libraries.* J. Mater. Chem., 2004. 14: p. 2627 - 2632.

15 Burgold, J., F. Weise, M. Fischer, G. Schlingloff, T. Henkel, J. Albert, G. Mayer, A. Schober, *Evolution and operating experiences with different drop-on-demand systems.* Macromol. Rapid Commun., 2005. 26: p. 265 - 280.

16. Smith, W.F., *Organic electronics: Self-assembly is ready to roll.* Nat. Nanotechnol., 2007. 2: p. 77-78.

17. Kubitschko, S., J. Spinke, T. Brückner, S. Pohl and N. Oranth, *Sensitivity enhancement of optical immunosensors with nanoparticles.* Anal. Biochem., 1997. 253: p. 112-122.

18. Brust, M. and C.J. Kiely, *Some recent advances in nanostructure preparation from gold and silver particles: a short topical review.* Colloids and Surf. A, 2002. 202: p. 175–186.

19. Hirai, H., H. Wakabayashi, and M. Komiyama, *Polymer-protected copper colloids as catalysts for selective hydration of acrylonitrile.* Chem. Lett., 1983. 12: p. 1047-1050.

20 Gamerith, S., A. Klug, H. Scheiber, U. Scherf, E. Moderegger, E.J.W. List, *Direct ink-jet printing of Ag–Cu nanoparticle and Ag-precursor based electrodes for OFET applications.* Adv. Funct. Mater., 2007. 17: p. 3111-3118.

21. Zhao, N., M. Chiesa, H. Sirringhaus, Y. Li, Y. Wu, and B. Ong, *Self-aligned inkjet printing of highly conducting gold electrodes with submicron resolution.* J. Appl. Phys, 2007. 101: p. 064513(1-6).

22. Ko, S.H., J. Chung, H. Pan, C.P. Grigoropoulos and D. Poulikakos, *Fabrication of multilayers passive and active electric components on polymer using inkjet printing and low temperature laser processing.* Sensors and Actuators A, 2007. 134: p. 161-168.

23. Sivaramakrishnan, S., P. J. Chia, Y.C. Yeo, L.L. Chua and P.K.-H. Ho, *Controlled insulator-to-metal transformation in printable polymer composites with nanometal clusters.* Nature Materials, 2007. 6.

24. Crone, B.K., Davids, P.S, Campbell, I.H, Smith, D.L, *Device model investigation of single layer organic light emitting diodes.* J. Appl. Phys., 1998. 84: p. 833-842.

25. Huitema, H.E.A., G.H. Gelinck, J.B.P.H. van der Putten, K.E. Kuijk, C.M. Hart, E. Cantatore, P.T. Herwig, A.J.J.M. van Breemen and D.M. de Leeuw, *Plastic transistors in active-matrix displays.* Nature, 2001. 414: p. 599.

26. Logothetidis, S. and A. Laskarakis, *Towards the optimization of materials and processes for flexible organic electronics devices.* Eur. Phys. J. Appl. Phys., 2009. 46: p. 12502.

27. Nakada, H., *The status of development of organic light emitting diodes / organic thin-film transistors.* J. Photopolym. Sci. Technol., 2007. 20: p. 35 - 38.

28. Calvert, p., *Inkjet printing for materials and devices.* Chem. Mater., 2001. 13: p. 3299 – 3305.

29. See for example: Cima Nanotech: http://www.cimananotech.com/; Harima Chemicals: http://www.harima.co.jp/en/index.html; Ulvac Technologies: http://www.ulvac.com/; Advanced Nano

Products: http://www.anapro.com/english/default.asp; Cabot corporation: http://www.cabot-corp.com/GlobalGateway.aspx. [*accessed on 15th June 2009*].

30. Greer, J.R. and R.A. Street, *Mechanical characterisation of solution-derived nanoparticle silver ink thin films.* J. Appl. Phys., 2007. 101: p. 103529(1-5).
31. Lee, H.H., K.S. Chou, and K.C. Huang, *Inkjet printing of nanosized silver colloids.* Nanotechnol., 2005. 16: p. 2436-2441.
32. Perelaer, J., A.W.M. de Laat, C.E. Hendriks and U.S. Schubert, *Inkjet-printed silver tracks: low temperature curing and thermal stability investigation.* J. Mater. Chem., 2008. 18: p. 3209-3215.
33. van Osch, T.H.J., J. Perelaer, A.W.M. de Laat, U.S. Schubert, *Inkjet printing of narrow conductive tracks on untreated polymeric substrates.* Adv. Mater., 2008. 20: p. 343–345.
34. Brust, M., D. Bethell, C.J. Kiely, and D.J. Schiffrin, *Self-assembled gold nanoparticle thin films with nonmetallic optical and electronic properties.* Langmuir, 1998. 14: p. 5425-5429.
35. Terrill, R.H., T.A. Postlethwaite, C.h. Chen, C.D. Poon, A. Terzis, A. Chen, J.E. Hutchison, M.R. Clark, G. Wignall, J.D. Londono, R. Superfine, M. Falvo, C.S. Johnson Jr., E.T. Samulski, and R.W. Murray, *Monolayers in three dimensions: NMR, SAXS, thermal, and electron hopping studies of alkanethiold stabilised gold clusters.* J. Am. Chem. Soc., 1995. 117: p. 12537-12548.
36. Stoltze, P., *Simulation of surface defects.* J. Phys.: Condens. Matter, 1994. 6: p. 9495-9517.

2 Overview Metal Nanoparticles

2.1 Introduction

The advancement in the understanding of the science behind nanoparticles (NPs) and its potential for various applications, based on the physics and chemistry at nanoscale, rests on the size dependence and other physical properties. Preferably it requires ideal preparation & processing conditions and isolation of monodisperse metal NPs with great measure of control over size, composition, structure, and stability. Polydisperse metal NPs have wide range of technological applications, but the methods of producing metal NPs were defined by the functionality and not developed with the aim of producing well–defined NPs. The preparation methodologies and processing parameters tend to produce metal NPs with range of sizes and morphologies that are broad enough to diminish the unique physico-chemical properties which monodisperse metal nanoparticle could exhibit. On these directions physicists and chemists addressed the metal NPs research that spill over century, right from Michael Faraday in 1857[1] to Brust & Schiffrin in 1994.[2]

2.1.1 Historical background

Colloidal metal NPs science has begun with the experiments of Michael Faraday in the 19th century, where he has studied the experimental relations of gold and other metals to light. Deep red solutions of gold precursor [$AuCl_4^-$] was reduced by phosphorous,[1] and later the method was repeated by J.M. Thomas in Faraday's laboratory that produced gold (Au) NPs of size 3 – 30 nm.[3] Turkevitch's detailed study together with early electron microscopic characterization on this field yielded more insights on the nucleation, growth and agglomeration of NPs that are soluble in water.[4] [$AuCl_4^-$] precursor solution was reduced by sodium citrate in water in different proportions,

which yielded NPs of varying sizes from from 20 – 200 nm with limited control on size distribution. In general these methods produced NPs of long range sizes, depending on processing conditions, and most of the examples falling in the larger diameter range (d >>20 nm). In 1994, Brust and Schiffrin reported the two-pahse reduction of [$AuCl4^-$] precursor by $NaBH_4$ in the presence of alkyl thiols to produce stable toluene soluble Au NPs of particle size d = 2 nm. As the metal NPs have wide range of applications such as catalysis and medicine, research has been focused on various aspects such as its morphology & structural properties that are relevant only to these applications.[2, 5-7] The importance of metal NPs in plastic electronics as printable electrodes and interconnects requires an understanding of insulator-to-metal transformation (T_p) and coalescence of metal NPs, which has drawn the attention only recently.[8-11]

2.2 Requirements of nanometal "inks" for plastic electronics

The printability of monolayer (ligand shell) protected Au, Ag and other metal NPs in the ambient and eliminating the protective ligand shell by heat treatment to give continuous nearly-bulk metal films[12] are significant for various applications especially as electrodes, conductors, interconnects and bus lines in plastic electronics,[11, 13-16] radiofrequency identification circuits (RFID tags), and large-area solar and lighting panels. In order to materialize this potential, it is essential to develop metal NPs with low T_p and high dispersibility in polar solvents such as water and high-boiling alcohols. These will be compatible with substrates and underlying structures that may not withstand aromatic hydrocarbon solvents, and/or high temperatures. For these applications, therefore, it is crucial to achieve metallic conductivity σ_{dc} > 10^5 S cm^{-1} at T_p < 170ºC for short annealing times. However the T_p cannot also be too low, otherwise premature sintering of the NPs, e.g. at the print head, becomes another issue.

The T_p is an operationally defined temperature at which the metal NP film undergoes an insulator-to-metal transformation, can be best represented on a temperature–time–transformation (TTT) diagram. This transformation is of morphological nature as the metal NPs initially isolated by insulating shells sinter to give bulk percolated metallic structures.

It is also learnt that, from the work done by my colleague in our laboratory, Wong Loke Yuen on the ink–jet printable inks, low surface tension solvents (≈30x10^{-3} N m^{-1}) such as xylenes spread very fast on the substrates; hence it is difficult to inkjet print with controlled line width. On this direction, high surface tension solvents as the dispersing agents (such as water–ethylene glycol mixtures) are important to achieve the acceptable line width according to application functionalities. Therefore it becomes critical to develop metal NP systems that are dispersible in high surface tension polar solvents at high concentration of commercial standards, > 100 mg mL^{-1}.

2.3 Fundamental physical considerations

2.3.1 Spherical particle approximation and magic clusters

Because of the small particle core radii (r), these metal NPs have a surface-area-to-volume ratio and a volume fraction (in the film) that are very sensitive to r and to the thickness of the dispersant layer (t). Fig.2.1 shows the total number of atoms in the bulk (open circles) and on the surface (open squares) for perfect or truncated octahedrons with magic number of atoms, which are the idealized shapes for Au (and other fcc) NPs, [7, 17] superimposed on analytic lines computed for spheres. The number of atoms per core was computed from:

$$v = \frac{\frac{4}{3}\pi r^3}{v_{atom}} \qquad \text{eq. 2.1}$$

where the atomic volume can be computed from the crystallographic density and atomic weight of the metal (for Au, it is 1.69×10^{-23} cm^3).

The number of surface atoms was computed from:

$$n_{surf} = \frac{4}{3}\pi(r^3 - (r - \delta_{atom})^3)v_{atom}^{-1} \qquad \text{eq. 2.2}$$

where δ_{atom} is the thickness of an atomic layer which can be computed from crystallographic data. For face-centred cubic lattice, this is one third of the body diagonal, also given by $\delta = \sqrt{\frac{8}{3}}r$, where r is the atomic radius (for Au and Ag, δ_{atom} is 2.60 Å).

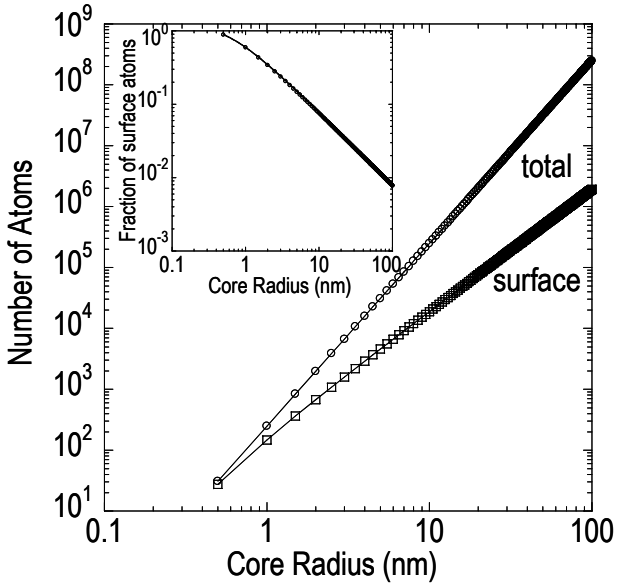

Figure 2.1 Particle size effect on number of atoms: Representation of total number of atoms and the number surface atoms on spherical NPs with respect to its core-radius. Inset shows how the fraction of surface atoms decrease with increase in core-radius

Thus for a practical NP r of 0.6–100 nm, the number of atoms varies from 55 to 2.5×10^8 per NP. The inset shows the fraction of atoms on the surface for these octahedrons, and also that predicted for spheres.

It is clear from both plots that the simple analytical relations for spheres are sufficient to predict the atom number and surface fraction of the actual polyhedrons the NPs often adopt. For the small NPs with r < 2 nm, more than one-third of the atoms resides on the surface. For the smallest practical NP of 55 atoms (r = 0.6 nm), 76% of the atoms reside on the surface.

Very small metal nanoparticles with less than 100 atoms (radius r < 0.75 nm) are more appropriately referred to as clusters, because their electronic structure turns discrete and molecular in character. It is known that 55-atom clusters (55 is a cluster magic number) of Au, Pt and Pd are not fully metallic as the Fermi surface breaks up, but NPs with r > 0.75 nm are practically metallic, although the surface layer atoms which are strongly coordinated to the ligand may still be in a different (non-metallic) environment.[18, 19]

2.3.2 Fill factor and porosity effect

NPs are typically protected by a molecular dispersant layer. Because of the small size of the NPs, the thickness (t) of the dispersant layer corresponds to a significant volume fraction of the NPs. It is the ratio of this thickness to the core radius (t/r) that is important. Because t has a finite value, it sets the lower practical limit for the size of the NPs determined by porosity effects. This consideration is unique to NP metal films and not found in electrochemical or evaporated films or in films of metal pastes. The mechanical integrity and electrical conductivity degrade severely as this limit is approached. It is known that the hardness and Young's modulus of NP Ag films are lower than that of bulk films of a similar grain size.[8]

As-deposited NPs are expected to be packed in a random-closed packing (rcp) structure.[20, 21] This is also suggested by transmission electron microscopy.[11] The metal fill factor (i.e. volume fraction of the metal cores) in the deposited film is given by:

$$v_f = F(1+\frac{t}{r})^{-3} \qquad \text{eq. 2.3}$$

Where F is the packing fill factor for the NPs, which for a rcp of monodispersed spheres is 0.634[22] (and 0.740 for face-centred-cubic or hexagonal close-packing), and t/r is the dispersant shell thickness-to-core radius ratio. Note that the NP radius $r_{NP} = r + t$.

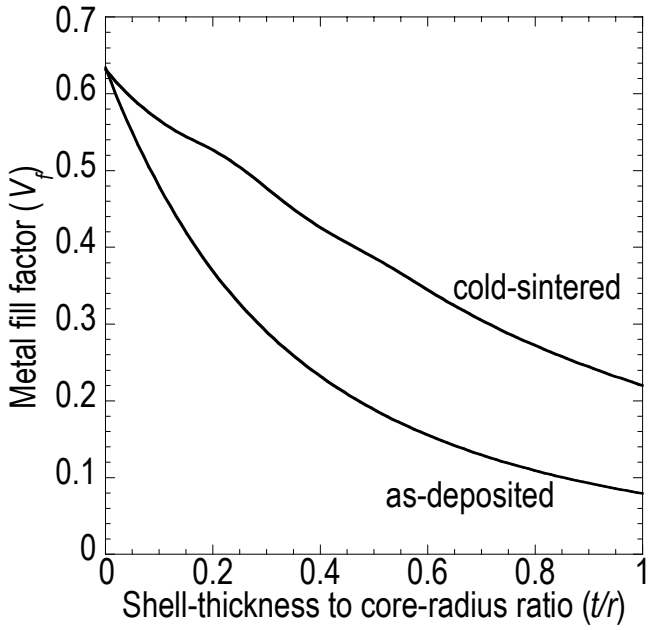

Fig 2.2 Metal Fill factor: Metal fill factor of as-deposited and cold-sintered metal NP film, after annealing at T_p, as a function of ratio of shell-thickness to core-radius.

Figure 2.2 shows how rapidly the metal fill factor decreases with t/r. For t/r = 0.40, the as-deposited film contains only 23 vol% metal, which decreases to 8 vol% at t/r = 1. For an rcp structure, 36% of the volume is void and the rest occupied by the dispersant shell. The important parameter is the fill factor after coalescence. It is shown in Chapter 4 that the coalescence of the metal NPs arises from cold-sintering of the metal cores that come into physical contact upon

desorption (or volatilization) of the ligand shell and not melting and fusion of the metal cores. This cold-sintering is accompanied by significant densification of the NP metal film but does not completely eliminate porosity in the films. A model for this process is as follows: As the ligand shell disappears, the metal cores become free to explore of its vicinity by Brownian motion and under the influence of gravity. When two neighboring cores touch, a metal neck forms, and the cores are fixed in its place. Overall therefore the metal cores settle downwards into a random "loose" packing, and the film contracts locally in all directions. However, because the lateral extension of the metal film is fixed, only the film thickness direction can show an overall (macroscopic) contraction. Large voids and crevices are opened up in the lateral directions which contribute to the porosity. This process is immensely difficult to simulate precisely. However we develop here a useful approximate analytical result for the metal fill factor after cold-sintering. From simulations the rcp structure locally can be considered an average of the close-packed (cp, 12-coordinated) and non-close-packed simple cubic (sc, 6-coordinated) structures. The fill factor for the rcp (0.634) is within 0.3% of the mean of the cp (0.740) and sc (0.524) structures. The radial distribution function for rcp is also in between that of the cp and sc structures.[20, 23] Therefore the contraction of the rcp network in the thickness direction can be obtained from the behavior of the local cp and sc structures. This can be obtained by simple geometric considerations of the vertical relaxation of vertical (along high symmetry directions) atomic plane spacing in the hard sphere approximation as r_{NP} changes from $r + t$ to r without allowing the lateral dimensions to relax from the initial state. The results are:

For fcc in the (111) direction,

$$v_f = \frac{\pi}{3\sqrt{3}(1+\frac{t}{r})^2\sqrt{1-\frac{1}{3}(1+\frac{t}{r})^2}} \qquad \text{for } \frac{t}{r} \le \frac{1}{2} \qquad \text{eq. 2.4}$$

$$v_f = \frac{2\pi}{3\sqrt{3}(1+\frac{t}{r})^2} \quad \text{for} \quad \frac{t}{r} > \frac{1}{2} \qquad \text{eq. 2.5}$$

For fcc in the (100) direction,

$$v_f = \frac{\pi}{3\sqrt{2}(1+\frac{t}{r})^2\sqrt{2-(1+\frac{t}{r})^2}} \quad \text{for} \quad \frac{t}{r} \le \sqrt{\frac{3}{2}} - 1 \qquad \text{eq. 2.6}$$

$$v_f = \frac{\pi}{3(1+\frac{t}{r})^2} \quad \text{for} \quad \frac{t}{r} > \sqrt{\frac{3}{2}} - 1 \qquad \text{eq. 2.7}$$

For sc in the (110) direction,

$$v_f = \frac{\pi}{6(1+\frac{t}{r})^2\sqrt{2-(1+\frac{t}{r})^2}} \quad \text{for} \quad \frac{t}{r} \le \sqrt{\frac{3}{2}} - 1 \qquad \text{eq. 2.8}$$

$$v_f = \frac{\pi}{3\sqrt{2}(1+\frac{t}{r})^2} \quad \text{for} \quad \frac{t}{r} > \sqrt{\frac{3}{2}} - 1 \qquad \text{eq. 2.9}$$

For sc in the (100) direction,

$$v_f = \frac{\pi}{6(1+\frac{t}{r})^2} \qquad \text{eq. 2.10}$$

By taking the mean of these results weighted to the probability factor for the different directions, and applying a smoothing to damp out oscillations, and then averaging with the initial structure to account for a nanostructure that is evolved halfway towards the vertically “close-packed” structure, we obtained the curve labeled “cold-sintered” in Fig. 2.2.

For *t/r* = 1, the final metal fill factor is only 16% (far below the random loose packing value of 55%[22] due to the open structure in the film plane resulting in large voids and cracks) and the film is highly porous. Such films will undoubtedly have poor mechanical properties and poor electrical conductivity. Electrical conductivity is proportional to the density of percolation paths, which in a

first approximation is given by the fill factor. This increases to 40% for *t/r* = 0.3, indicating that nearly compact film can be produced by cold sintering. It may be noted that conductivity should be anisotropic in such distorted rcp networks. The porosity of the film is 37% before and 1 – v_f after cold sinter. The porosity increases after sintering (due to loss of the protection shell) to 60 vol% for t/r = 0.3 and 84 vol% for t/r = 1 after sinter, which increases film stress and weakens film mechanical properties accordingly. There is experimental data supporting this model. For t/*r* = 0.2, for example, the contraction is 13%, which has been measured experimentally for *r*=25 nm Ag NPs protected by a 5-nm-thick polymeric dispersant after long anneal in air.[8] Prolonged anneal or at elevated temperatures can destroy the nanoparticulate nature to give further densification by Ostwald ripening. However this inevitably leaves macroscopic voids that break film conductivity.[9, 24]

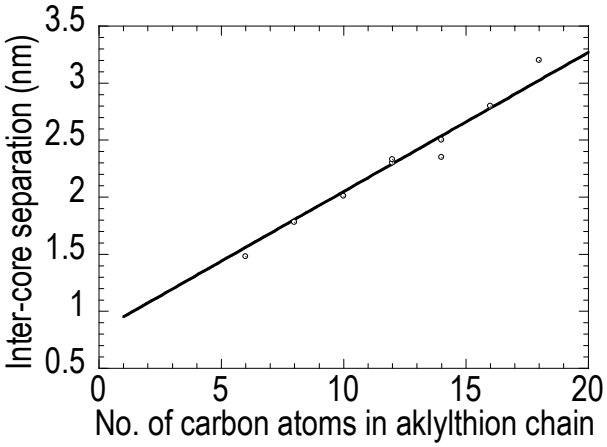

Fig 2.3 Inter-core separation of metal NPs: Inter-particle gap as a function of number carbon atoms in protective monolayer, alkylthiol chain (data replotted from ref.[25 & 26]

It is also known that the inter-particle spacing (inter-core gap) increases with increase in number of carbon atoms present on the protective ligand shell. Fig. 2.3 shows how the inter-particle spacing increases with respect to number of carbon atoms on the alkylthiol protective ligand shell.[25, 26]

The inter-particle gap follows the trend $L = 0.83 + 0.122n$, where L is the inter-core separation and n is the number of carbon atoms in the protective alkylthiol chain.

2.3.3 Matrix dilution effect

The presence of a polymer binder, which may improves certain properties such as cohesion and adhesion and resistance to micro-cracking in the final NP metal film, opens up an average inter-particle gap d_{gap} due to the matrix dilution. This gap scales directly with metal core radius r assuming the homogeneous dispersion of the particles in the matrix (i.e., no clumping or phase segregation occurs). Such a homogeneous dispersion can be readily achieved in the case of water-soluble NPs dispersed in a polyelectrolyte matrix of the same charge sign as the ligand shell of the NP.[11, 27] If phase separation occurs due to incompatibility between the NPs and the binder, then the dispersion can become very heterogeneous and the film quality becomes very poor. The exact relation is very difficult to compute, as it may depend on details of the hydrodynamics, rheology of the final-stage drying of the films, and any subsequent reflow.

The essential feature to note is that the average gap due to the spacing out by the binder fraction is proportional to the particle size. As the cold sintering depends on the physical contact between the metal cores, the crude picture suggests that it is rapidly degraded by increasing metal core sizes in the presence of a fixed non-volatile binder polymer volume fraction. Such a sensitivity has in fact been found experimentally for Au cores, which suggests an upper limit to $r < 4$ nm.[11]

Fig. 2.4 replotted from Ref.[11] shows a 25ºC rise in the coalescence temperature as the Au core diameter increases from 2.2 to 4.2 nm in the presence of a constant 30 vol% of poly(3,4-

ethylenedioxythiophene)–polystyrenesulfonic acid as compatible matrix. It is learnt that the increase in coalescence temperature of 25 ºC, from r = 2.2 nm to r = 4.2 nm, is due to the matrix dilution effect, and not due to the thermodynamic size effect of metal NPs.

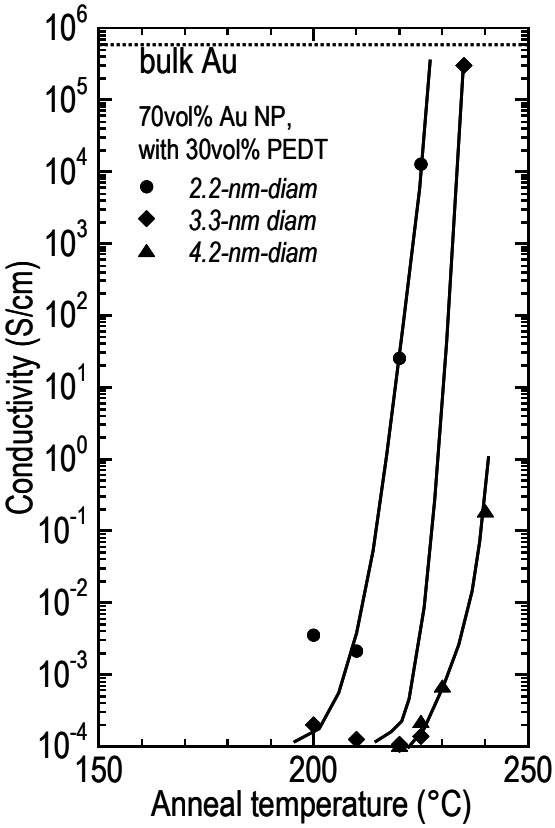

Fig 2.4 Matrix dilution effect: Coalescence behaviour of mixed monolayer protected Au NPs as a function of core-diameter of NPs at constant volume of matrix, 30% v/v of poly(3,4-ethylenedioxythiophene):poly(4-styrenesulfonic acid) (PEDT:PSSH). Data replotted from ref. [11].

2.3.4 Summary: the optimal nanoparticle core size.

From the above discussion, optimal core radius for nanometal inks rests on several factors. Metal NPs achieve metallic character for r > 0.8 nm; and the porosity effect practically requires r > 2 nm depends on the dispersant shell thickness. Matrix dilution effect, if there is any, sets an upper limit for r < 4 nm for a matrix volume fraction of 0.2. When the metal NPs are formulated with much

higher dispersant and binder content (>25 weight% binder, corresponding to >70 vol% binder in some commercial preparations), a long heat-treatment time at high temperatures will be required to "burn off" the binder in air before satisfactory sintering can be achieved. This will be associated with large volume contraction that leads to stress and micro-cracking of the sintered film, which will deteriorate the final σ_{dc}.

2.4 Solvent dispersibility

The required metal concentration in the dispersion can be estimated simply from the desired final film thickness and the dimensions of the liquid film. If a metal NP line of thickness *d* and width *w* is to be deposited by a single-pass printing, all the metal is contained in the initial deposited liquid volume. Due to the small dimensions *w*, effects of gravity (acceleration due to gravity *g*) is negligible compared to the surface tension σ (the Bond number $B = \rho g w^2 / \sigma \approx 10^{-3}$), so the cross-section of the liquid line is a truncated cylinder bounded by contact angle θ.[28] The cross-section area is given by $\frac{w^2(\theta - \sin\theta\cos\theta)}{4\sin^2\theta}$.[28] The required metal content can be readily found to be $n_{metal} = \frac{4\sin^2\theta}{(\theta - \sin\theta\cos\theta)}\frac{d\rho}{w}$, for *d* = 100 nm, *w* = 50 μm, ρ = 19 g cm^{-3} (Au), $\theta = \pi/2$, n_{metal} = 0.1 g cm^{-3}. Au NPs stabilized by molecular dispersants such as alkyl thiols via the Brust–Schiffrin process,[2] which are soluble in organic solvents at such high concentrations are not available; however water soluble Au NPs, at high concentration, are protected by ω-functionalized alkylthiol via a modified Brust–Schiffrin process,[11] and Ag NPs stabilized by polymeric dispersants which are already available (e.g., Nippon and Cabot's Ag conductive inks). Some of

the latter however have very high dispersant content (> 25 weight% binder, corresponding to > 70 vol% binder) for stability which then necessitates high coalescence temperature.

It will be very desirable to be able to achieve high dispersabilities in the three main classes of solvents. Three important classes of solubility behavior can be distinguished: those that are hydrophilic and dispersible in water and other polar-solvents (e.g., ethylene and propylene glycols), those that are oleophilic and dispersible in non-polar aliphatic and aromatic solvents (e.g., tetradecane, mesitylene), and those that are fluorophilic and dispersible in the fluorocarbon solvents. Nano-metal inks are preferred in the first class as stated in section 2.2.

Solvent dispersibility of metal NPs are mainly controlled by the functionality of terminal end group of protective monolayer chains. Table 2.1 summarises the solubility characteristics of metal NPs protected by alkylchains with different terminal end groups.

Table 2.1 Solubility characteristics of metal NPs protected by ligand shells of difference terminal functional groups

Ligand shell termination	Solubility
Methyl ($–CH_3$)	Toluene, hexane, THF, chloroform
Carboxylic acid (–COOH)	Methanol, ethanol
Carboxylate (sodium salt) ($–COO^- Na^+$)	Water
Carboxylate (tetraoctylammonium salt) ($–COO^- Oc_4N^+$)	Methanol, toluene, hexane
Hydroxyl group (–OH)	Toluene, hexane, THF
Sulfonate (sodium salt) ($–SO_3^- Na^+$)	Water
Sulfonic acid	Water, Methanol

2.5 Depression of the nanocore melting temperature

It is well-known that metal NPs have depressed melting point transition that depends on radius of the NP, *r*.[29-35] Several simple phenomenological thermodynamic equations have been proposed in the literature, as described below. A popular equation is the Pawlow eqn formulated for the equilibrium between a solid NP, a liquid NP and the vapor phase:

$$\frac{T_m}{T_m^o} = 1 - \frac{2}{\rho_S L_o r}(\gamma_S - \gamma_l(\frac{\rho_S}{\rho_l})^{2/3}) \qquad \text{eq. 2.11}$$

where T_m is the melting temperature of the NP, T_m^o is the melting temperature of the bulk metal, ρ_s and ρ_l are the solid and liquid densities respectively, γ_s and γ_l are the solid and liquid surface energies, L_o is the enthalpy of fusion, all taken for the bulk solid at T_m^o. Therefore there is no free parameter in this form. However, it severely overestimates T_m particularly of the smaller NPs and requires the second-order terms to reproduce the experimental results, but the resultant equation becomes massive, and involves several unknown parameters.[30]

Another popular equation is the Hanszen–Wronski equation formulated for equilibrium between a solid NP core and liquid over-layer:

$$\frac{T_m}{T_m^o} = 1 - \frac{2}{\rho_S L_o}(\frac{\gamma_{sl}}{r - \delta_l} - \frac{\gamma_l}{r}(1 - \frac{\rho_S}{\rho_l})) \qquad \text{eq. 2.12}$$

where γ_{sl} is the solid-liquid interface energy, and δ_l is the thickness of the liquid over-layer.

A third popular equation is the Sambles equation formulated from the same theory but with different approximation:

$$\ln\frac{T_m}{T_m^o} = -\frac{2}{\rho_S L_o r_S^*}\left(\frac{\rho_l}{\rho_S}\right)^{1/3}\left(\gamma_l\left(1-\frac{\rho_S}{\rho_l}\right)+\gamma_{sl}\left(1-\frac{\delta_l}{r_S^*}\left(\frac{\rho_S}{\rho_l}\right)^{1/3}\right)^{-1}\right) \qquad \text{eq. 2.13}$$

where r_S^* is the hypothetical radius of the NP in the completely solid form.

All these theories neglect the dependence of ρ_s, ρ_l, γ_s, γ_l, γ_{sl} and L on T and r, and are thus at best useful but empirical descriptions of the data through a small number of physically intuitive parameters. We re-evaluated the fitting of experimental data to these equations in Fig. 2.5. Both the Hanszen–Wronski and Sambles equations are equivalent in describing these data, while the Pawlow equation is a distinctly inferior choice. The simpler Hanszen–Wronski equation seems more desirable. The extracted values of δ and γ_{sl} are given in Table 2.2 below.

Table 2.2

	T_m^o (K)	ρ_s (g cm^{-3})	ρ_l (g cm^{-3})	γ_s (J m^{-2})	γ_l (J m^{-2})	γ_{sl} (J m^{-2})	L_o (J g^{-1})	δ_l (Å)
Au	1337	18.4	17.4	1.38	1.14	0.30	63.7	3
Ag	1235	9.82	9.32	1.14	0.95	0.35	104.5	6
Sn	505	7.18	6.98	0.66(estm)	0.58	0.080	59.2	22
Pb	601	11.04	10.66	0.53(estm)	0.47	0.055	23.0	20

The values of $\gamma_{sl} \approx \gamma_s - \gamma_l$, are thus reasonable. For Au, it is larger than the experimental value for macroscopic surfaces (0.13 J m^{-2}), which suggests a possible size effect in the NPs. Numerous molecular dynamic simulations for Au NPs[33, 36, 37] have demonstrated the presence of a liquid layer 1–2 atomic layers (i.e., 2.6–5.2 Å) thick at the surface of the NPs. This liquid-like layer (with high diffusivity and no long-range correlation) appears at a temperature ≈ 0.8 * T_m for the medium-size NPs, which can be taken to be the surface-melting temperature.[33, 37] Therefore the best-fit

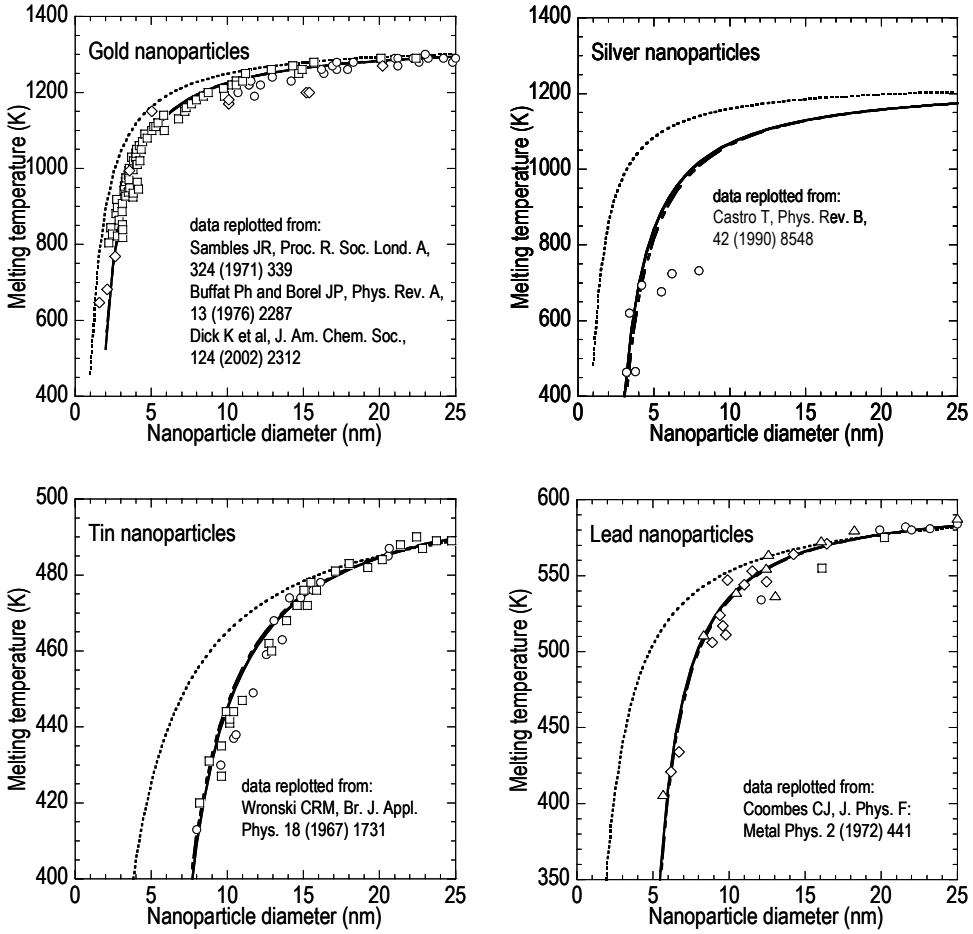

Figure 2.5 Thermodynamic size-effect of NPs: Thermodynamic size effect on the melting point depression of Au, Ag, Sn and Pb NPs: re-evaluated and replotted from the literatures

δ_l value (which is 6 Å for the Sambles equation and 3 Å for the Hanszen–Wronski equation, probably as a result of their differing treatment of what constitutes the liquid layer) is very reasonable. For Sn, calorimetry of the size dependence of melting enthalpy is in agreement with the notion of a disordered overlayer of thickness 20 Å, and appears to follow:[34]

$$\frac{L}{L_o} = (1 - \frac{\delta_l}{r})^3 \qquad \text{eq. 2.14}$$

2.6 Synthesis of metal nanoparticles

These NPs can be prepared by several methods in both gas and solution phases. The gas phase methods involve either spray pyrolysis or evaporation–condensation. The solution processes are often based on reduction of a metal precursor salt in the presence of the protection monolayer to obtain dispersed NPs in the solvent. This can often generate better controlled and narrower particle size distribution (PSD) which is expected to be technologically important, and at the same time also provide useful models to understand metal NP films. Thus solution processes form the focus of this section. In particular the phase-transfer Brust–Schiffrin[2] method can reproducibly give high-quality, narrowly-dispersed and isolable NPs with controlled mean diameter. This allows for direct molecular control over the ligand shell that stabilizes the NPs. This can be readily applied to Au and Ag NPs, but has the potential to be generalized further.

Purity of the NPs is an important consideration for electronic applications. The presence of non-volatile materials (both organic and ionic) trapped in between the NPs prevents the essential coalescence to the metal film. In addition, ions can be expected to lead to migration, corrosion and other problems. Therefore it is useful to be able to rigorously purify the particles by repeated precipitation, recrystallization or Soxhlet extraction. Also, the dispersibility of the NPs is an important figure-of-merit, although this is often not measured in the literature. In the following, we will attempt a non-exhaustive survey of some of the key methods. We briefly survey the range of procedures mainly for Au NPs that are available in the literature noting the properties of the obtained products. The traditional difference in approaches to the Ag and Au NPs provide an interesting contrast. While it is well known that Ag NPs prepared with polymeric dispersants are dispersible in water and polar organic solvents to very high concentrations required for printing, Au

NPs prepared with molecular dispersants too can reach similar high concentrations. Most of these work have not be conducted with the aim of producing robust and highly concentrated dispersions for nano-metal ink technologies, therefore their applicability is not known. By providing an overview, we wish to draw out some common strands.

2.6.1 Gold nanoparticles

A few reviews have recently been published on the preparation of Au NPs.[38, 39] The essential features of selected processes are summarized in Table 2.3. Traditionally, the most important substrate (starting material / precursor) for preparation of Au NPs is the tetrachloroaurate (III) $AuCl_4^-$ ion. Stable Au NPs can be prepared by citrate reduction of $HAuCl_4$ in boiling water,[4] with typical broad PSD in the 15 to a few hundred nm diameter range. To obtain better control over the PSD, a separate nucleation and growth method[40] has been used in which the smaller NPs initially formed by citrate reduction (15–20-nm-diameter) are then grown by reduction in sulfonated phosphine as dispersant.[19] However phosphine dispersants tend to hydrolyze in water or oxidized by air and results in de-stability of colloid.[41] Au NPs also have been prepared by using surfactant (e.g. cetyltrimethylammonium chloride, sodium dodecylsulfate, cetylpyridinium chloride) as dispersant.[42] The citrate-stabilized Au NPs can be ligand-exchanged by alkylthiols or ω-functionalized alkylthiols,[43, 44] oleate,[45] or long-chain alkylamine[46] to give Au NPs that are soluble in the organic phase. The $AuCl_4^-$ can also be reduced with $NaBH_4$ in the presence of bulky thiol groups (e.g. tripeptide glutathione,[47] 4-mercaptobenzoate,[43]) thiol ionic liquids[48] N,N-trimethyl(undecylmercapto)ammonium,[49] tiopronin or coenzyme[50] stabilized Au NPs also have been reported.

Table 2.3 Summary of preparation of Au NPs & its properties

Conditions	NPs	Ref.
Gold: Chemical reduction in aqueous or polar organic solvents		
Substrate: $HAuCl_4$ Reductant: sodium citrate Solvent: water Temperature: 100ºC, Dispersant: sodium citrate; ratio: 1.5	Shape: sphere Mean: 20nm Polydispersity: 20 Solubility: water Coalescence temp: - Stability:	[4]
Substrate: Citrate Au NPs Reductant: Citrate, seed growth Solvent: water Temperature: 22ºC, Dispersant: $(C_6H_5)_2PC_2H_4SO_3Na$; ratio: 1	Shape: sphere Mean: 20nm Polydispersity: 15 Solubility: water Coalescence temp: - Stability: unstable	[41]
Substrate: $HAuCl_4$ Reductant: N_2H_4 Solvent: water Temperature: 22ºC, 15hrs Dispersant: cetyltrimethylammonium chloride or sodium dodecylsulfate, or cetylpyridinium chloride; ratio: 0.25	Shape: sphere Mean: 1-4nm Polydispersity: 20 Solubility: water Coalescence temp: - Stability: Stable	[42]
Substrate: $NaAuCl_4$ Reductant: PVA or PEG Solvent: Water Temperature: 22ºC, 6days Dispersant: - ; ratio: -	Shape: - Mean: - Polydispersity: - Solubility: water Coalescence temp: - Stability: stable	[51]
Substrate: $HAuCl_4$ Reductant: $NaBH_4$ Solvent: water Temperature: 22ºC Dispersant: thiol ionic liquid; ratio:0.1	Shape: sphere Mean: 3nm Polydispersity: 15 Solubility: water Coalescence temp: Stability: few months stability	[48]
Substrate: $HAuCl_4$ Reductant: $NaBH_4$ Solvent: methanol/acetic acid (6:1) Temperature: 22ºC Dispersant:tiopronin; ratio:0.3	Shape: sphere Mean: 3nm Polydispersity: 35 Solubility: water Coalescence temp: Stability:	[50]
Substrate: $HAuCl_4$ Reductant: $NaBH_4$ Solvent: mixture of water and methanol Temperature: 22ºC Dispersant: tripeptide glutathione; ratio:0.3	Shape: sphere Mean: 1nm Polydispersity: - Solubility: water Coalescence temp: Stability:	[47]
Substrate: $HAuCl_4$ Reductant: $NaBH_4$ Solvent: water Temperature: 22ºC Dispersant: trimethyl(undecylmercapto)ammonium; ratio:0.3 equiv	Shape: sphere Mean: 5nm Polydispersity: 35 Solubility: water Coalescence temp: 225ºC Stability:	[49]

Substrate: $HAuCl_4$ Reductant: $NaBH_4$ Solvent: water Temperature: 22ºC dispersant: cetylpyridinium chloride; Phase-transfer dispersant: dodecylamine; ratio:0.3 equiv	Shape: sphere Mean: 15 nm Polydispersity: 15 Solubility: hexane Coalescence temp: Stability:	[46]
Gold: Phase-transfer to a non-polar organic phase, followed by chemical reduction		
Substrate: $HAuCl_4$ Reductant: $NaBH_4$ Phase-transfer agent: TOAB Solvent: water/toluene Temperature: 22ºC Dispersant: dodecanethiol; ratio: 1	Shape: sphere Mean: 2 Polydispersity: 10 Solubility: toluene Coalescence temp: - Stability: stable	[2]
Substrate: $HAuCl_4$ Reductant: $NaBH_4$ Phase-transfer agent: TOAB Solvent: water/toluene Temperature: 22ºC Dispersant: dodecylamine, oleylamine; ratio: 1	Shape: sphere Mean: 3nm Polydispersity: 25 Solubility: toluene,hexane Coalescence temp: Stability: stable	[52]
Substrate: $HAuCl_4$ Reductant: $NaBH_4$ Phase-transfer agent: TOAB Solvent: water/toluene Temperature: 22ºC Dispersant: mercaptosuccinic acid; ratio:0.5	Shape: sphere Mean: 3.5nm Polydispersity: 20 Solubility: water Coalescence temp: - Stability: stable	[53]
Substrate: $HAuCl_4$ Reductant: $NaBH_4$ Phase-transfer agent: TOAB Solvent: water/toluene Temperature: 22ºC Dispersant: PEG-SH; ratio: 0.1	Shape: sphere Mean: 3nm Polydispersity: 35 Solubility: water Coalescence temp: 320ºC Stability:	[54]

The phase-transfer Brust–Schiffrin method is presently the most important and convenient method to prepare high-quality isolable Au NPs.[2] The Au NPs are protected by a thiol monolayer by first transferring the $AuCl_4^-$ to organic phase (usually toluene) using a phase transfer agent tetraoctylammonium bromide, then mixing with the desired thiols and then the reductant (usually aqueous $NaBH_4$). These are dispersible typically in aromatic hydrocarbon solvents (e.g. toluene and other aromatic hydrocarbons) at the extremely high weight concentrations required for practical printing (> 50 mg mL^{-1}, due to high metal density) without requiring a polymeric dispersant. The PSD is considerably narrower than citrate reduction,[4] and the mean of the

distribution can be controlled simply through the mole ratio of the thiol to the gold between 1.5–5-nm-diameter,[7] as shown in Fig. 2.6.

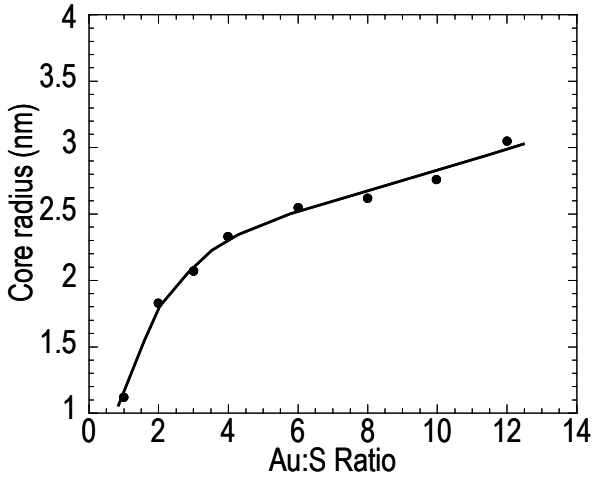

Fig 2.6 Core-radius as a function of metal-to-ligand ratio: Core-radius of Au NPs as a function of gold-to-thiol (Au:S) ratio, adapted from ref. [7].

Au NPs can also be prepared in the same way with amines,[52] ω-functionalized alkylthiols,[53, 55] thiolated poly(ethylene glycol)[54, 56] as dispersant by this phase transfer method.

2.6.2 Mixed ionic monolayer protected Au NPs

The Brust–Schiffrin phase-transfer process is eminently suited to the production of NPs dispersible in the organic hydrocarbon phase. To take advantage of the size control inherent in this process with molecular ligand protection but to produce NPs that are dispersible in water and polar organic solvents, two extensions have been developed. Highly water-dispersible Au NPs can be produced using mixed monolayers of an ω-carboxyl-terminated alkylthiol and an ω-hydroxyl-terminated alkyl thiol, after ion-exchange of the proton to alkali-metal cations.[11] The obvious strategy of using pure ω-carboxyl-terminated alkylthiol does not produce robust water-dispersible NPs. Dispersibility

in water exceeds 5 wt% for these NPs. Other mixed monolayer systems reported by Uzun et al that gives highly water–dispersible Au NPs.[57]

2.7 Polymer–nanometal composites

2.7.1 Percolation

Its also understood that for films with lower Au content down to 30:70 v/v, the percolative transformation can still occur, but the maximum σ_{dc} is greatly reduced (to 2×10^3 S cm^{-1} for 50:50 v/v; and 6×10^1 for 30:70).[11] This suggests that the volume percolation threshold (v_c) is near 0.3.[58, 59] It appears broadly consistent with the random–lattice percolation model which predicts $v_c = 0.3$ and the simple–cubic lattice model for bond percolation predicts $v_c = 0.25$.[58, 59] Just above percolation, σ_{dc} is expected to scale as $(v - v_c)^p$ where p is the critical exponent.[58, 59] Sivaramakrishnan et al deduced that $p \approx 2$ and $v_c \approx 0.26$ from the limited data.[11] Even with a dielectric polymer as matrix (e.g. poly(hydroxyl styrene)), the films still exhibit the conductive percolation transition.

Therefore these materials provide means to regulate the final film conductivity between 10^{-4} and a few 10^5 S cm^{-1} depending on volume fraction and cluster diameter. This is the organic analogue of the well–known inorganic cermets, and allows practical resistors 1–10^7 Ω to be fabricated by printing. Without the polymer matrix, this is not readily possible because of the more rapid transformation to the metallic state.

2.7.2 Suppression of microcrack formation

Films of these metal NPs have a tendency to develop cracks during solvent evaporation and particularly during annealing because of the large volume reduction. Substrate adhesion is poor and film cohesion could also be poor. Related to this is the dewetting of NP metal film, tend to dewet at high temperatures. One way to overcome all these is by employing a homogeneous polymeric binder that is intermixed at the molecular level that is also thermally robust, hence does not phase separate from the metal NPs.[11] An example is poly(3,4-ethylenedioxythiophene): poly(styrenesulfonic acid) (PEDT:PSS), which is air stable to > 150ºC and nitrogen stable to > 200ºC. Dispersion into polyelectrolyte matrices gives homogeneous films with "tuneable" conductivity[11] with only a small increase in T_p depending on volume fraction,[11] due to compatibilization (interaction) through the surface ionic groups. The molecular mixing has been demonstrated by TEM. This is distinct from the conventional role and characteristic of polymer binders in conventional electrically conductive adhesives. The 70:30 v/v Au–PEDT films with d = 2.2–3.3 nm, Au NP film transform between 210–230ºC to the highly conductive state with $\sigma_{dc} \approx 3 \times 10^5$ S cm^{-1}.[11] After the transformation, the conductivity is expected to be determined by the length and density of the percolated metallic paths. These appear to be sufficiently high for large σ_{dc} to be reached even in the presence of the PEDT polymer matrix. The matrix thus appears to retard T_p marginally by only 15–20ºC, and has no detrimental effect on the final σ_{dc} for films with high Au volume fraction of ≈ 0.7 and small Au size of 3.3 nm or less.[11] This also proves that the Au–polymer films are homogeneous; otherwise the percolated paths would break in the macroscopic regions that have low cluster density. This effectively suppresses microcrack formation which occurs in as-deposited thin films of metal NPs due to solvent evaporation, and

which becomes severe above about 250ºC for Ag NPs[9, 24] and Au NP[11] depending on film thickness, due to porosity at the higher temperatures.

For the larger Au clusters, T_p is further retarded, and the attainable σ_{dc} is decreased, as confirmed by data taken out to higher temperatures.[11] This is not unexpected, since the films with larger Au clusters have a proportionally larger mean inter–cluster spacing,[11] which adversely affects the development of the percolation paths. In these homogeneous composites, the mean inter–cluster spacing is set by the matrix volume fraction spanning the inter–cluster space and the cluster diameter, in addition to the ligand shell thickness.[11] The volume fraction and cluster diameter therefore provide a sensitive means to adjust the overall conductive properties of the nanocomposite.

2.7.3 Improved film adhesion to substrate and other advantages

The nano–Au and in particular the Au–polymer films have passed the scotch-tape peel test on appropriately–treated substrates (*e.g.*, $HOOCCH_2CH_2SiO_3$-treated silicon substrates),[11] in contrast to those obtained from alkylthiolate–protected Au NPs. This adequate substrate adhesion is essential for electrode and device integrity on flexible substrates to be achieved.

A further advantage of using PEDT is the improvement in hole injection valuable to a host of devices including organic light–emitting diodes and field–effect transistors.

2.8 Plasmon resonance band in metal NPs – theory and simulation

The most distinctive spectroscopic feature of metal NPs is the presence of a plasmon resonance band in the optical spectrum that is not present in continuous thin films. Plasmons are coherent

longitudinal oscillations of the free-electron density. The absorption appears as a structureless broad band whose position, intensity, and shape depend on the NP and its surroundings. This band is readily measured in standard UV-Vis spectroscopy and provides useful characterization of the NPs..

2.8.1 The dielectric function

The complex dielectric function of metal NPs can be obtained from the dielectric function of the bulk metal in a surprisingly simple way by correcting for the effects of electron confinement on its collision frequency. The dielectric function of bulk metal can be written as the sum of a bound response and a free-electron response:[60]

$$\tilde{\varepsilon}_{bulk} = \tilde{\varepsilon}_{bound} + \tilde{\varepsilon}_{free}, \qquad \text{eq. 2.15}$$

where $\tilde{\varepsilon}_{bound}$ is the dielectric function of the bound electrons and $\tilde{\varepsilon}_{free}$ is the contribution from the free electrons.

The free electron contribution can be written explicitly from Drude theory for free-electron-like metals:

$$\tilde{\varepsilon}_{bulk} = \tilde{\varepsilon}_{bound} - \frac{\omega_p^2}{\omega^2 + i\omega\gamma_{bulk}} \qquad \text{eq. 2.16}$$

where ω_p is the plasma frequency of the metal; ω is the frequency of the incident light and γ_{bulk} is the scattering frequency of bulk metal. The results show that this plasmon resonance becomes severely smeared out for NPs with core diameter less than 1 nm due to strong scattering of the conduction electrons by confinement to a space much shorter than their natural mean free path, as confirmed by experiments. [7, 61]

For the nanocores of these metals, the free electron contribution is modified in a simple way in the nanocore by the increased scattering frequency within the core:[60, 62-65]

$$\tilde{\varepsilon}_{nano} = \tilde{\varepsilon}_{bulk} + \frac{\omega_p^2}{\omega^2 + i\omega\gamma_{bulk}} - \frac{\omega_p^2}{\omega^2 + i\omega\gamma_{nano}} \qquad \text{eq. 2.17}$$

where $\gamma_{nano} = \gamma_{bulk} + C\frac{v_F}{r}$, in which C is the scattering factor including electron–electron, electron–phonon, electron–defect interactions in the nanocore, v_F is the bulk Fermi velocity, r is the NP radius, and ω_p is the plasmon frequency. $\tilde{\varepsilon}_{bulk}$ can be obtained from spectroscopic ellipsometry, and are extensively tabulated in data books.[66] For Au, fitting of the optical data to Drude theory gives ω_p = 1.3 x 10^{16} s^{-1}, γ_{bulk} = 1.64 x 10^{14} s^{-1}, while its v_F can be deduced from electronic heat capacity to be 14.1x10^{14} nm s^{-1}.

The complex dielectric function of the solid film of a dense packing of nanocores or solution of dilute nanocores can be computed using an appropriate effective medium approximation for the system.[67] Once the dielectric function is known, the optical transmission and reflection spectra can be computed self-consistently using Fresnel transfer matrices.[68]

2.8.2 Core-shell effect.

For dilute dispersions in a solvent, it is obvious that the appropriate effective medium approximation (EMA) is the Maxwell–Garnet approximation since the microstructure is clearly one of NP "guests" dispersed in a host. For a three component system of a metal nanocore surrounded by a ligand shell, and embedded in a medium, the dimensionless complex polarizability of core–shell NP is given by the Van de Hulst result to be:[63, 69]

$$\tilde{\alpha} = 3\frac{(\tilde{\varepsilon}^{shell} - \tilde{\varepsilon}^{matrix})(\tilde{\varepsilon}_{nano} + 2\tilde{\varepsilon}^{shell}) + q^3(2\tilde{\varepsilon}^{shell} + \tilde{\varepsilon}^{matrix})(\tilde{\varepsilon}_{nano} - \tilde{\varepsilon}^{shell})}{(\tilde{\varepsilon}^{shell} + 2\tilde{\varepsilon}^{matrix})(\tilde{\varepsilon}_{nano} + 2\tilde{\varepsilon}^{shell}) + q^3(2\tilde{\varepsilon}^{shell} - 2\tilde{\varepsilon}^{matrix})(\tilde{\varepsilon}_{nano} - \tilde{\varepsilon}^{shell})} \qquad \text{eq. 2.18}$$

where $q = \frac{r}{r+t}$ is the ratio of the core radius (r) to the sum of core radius and shell thickness (r + t) and so q^3 is the volume ratio of the core to the NP, $\tilde{\varepsilon}^{matrix}$ is the dielectric function of the matrix in which the NPs are dispersed, and $\tilde{\varepsilon}^{Shell}$ is that of the ligand shell that can be obtained experimentally or from standard published results.[66] The initial average value of q can be obtained from TEM images. This relation has been used to describe the behavior of a wide variety of metal NPs.

2.8.3 Dilute dispersions.

In dilute dispersions of the NPs in a dielectric (i.e., non-absorbing) media, the thickness absorption coefficient can be directly found from:

$$z_o^{-1} = \frac{2\pi}{\lambda_o}\sqrt{\varepsilon^{matrix}}\, f\alpha_2 \qquad \text{eq. 2.19}$$

where α_2 is the imaginary component of the polarizability, ε^{matrix} is the dielectric constant of dispersing media, and f is the combined volume fraction of core and shell. This can be written as an absorption cross-section per NP,

$$\sigma_{NP} = \frac{z_o^{-1}}{\rho_{NP}} \qquad \text{eq. 2.20}$$

where ρ_{NP} is the number density of the NPs. This can be converted to molar absorptivity ε used traditionally in solution-state spectroscopy where “molar” here refers to a concentration of 1 mol of metal atoms per liter of solution:

$$\varepsilon = \log e \frac{\sigma_{NP}}{c_{mol}} \qquad \text{eq. 2.21}$$

where log e = 0.43429.., c_{mol} is the number of moles of the metal atoms per NP. This quantity is thus normalized to the amount of metal atoms in solution, but is found both experimentally and theoretically to vary slightly with the NP core size, shell thickness and medium.

2.8.4 Concentrated dispersion or solid films.

Maxwell–Garnet effective medium approximation: It is useful to consider further the behavior of a concentrated dispersion of these NPs in a matrix as in solid films. The Maxwell-Garnett dielectric function ($\tilde{\varepsilon}^{MG}$) of the composite can then be obtained from the Clausius–Mosotti relation to be:

$$\tilde{\varepsilon}^{MG} = \tilde{\varepsilon}^{matrix} \frac{1+\frac{2}{3}f\alpha}{1-\frac{1}{3}f\alpha} \qquad \text{eq. 2.22}$$

where f is the volume fraction of the NPs (i.e., volume fraction of core and shell) with $f + f_{matrix} = 1$.

For a polydispersed or a composite system, this is readily extended to give:

$$\tilde{\varepsilon}^{MG} = \tilde{\varepsilon}^{matrix} \frac{1+\frac{2}{3}\sum_j f_j \alpha_j}{1-\frac{1}{3}\sum_j f_j \alpha_j} \qquad \text{eq. 2.23}$$

where j denotes the NPs of size or type j, with $\sum_j f_j + f_{matrix} = 1$.

Bruggeman effective medium approximation: In the case of nano–Au inks, near percolation temperature (T_p), nano–cores begin to coalesce to cause a sharp onset of dc conductivity in a percolative transition that generates a bi-continuous “smeared-out” morphology for which the MG EMA can fail. In this case we can consider the Bruggeman (Br) EMA to be more appropriate to

reproduce the experimental results.[10] The Br dielectric function ($\bar{\varepsilon}_r^{Br}$) can then be computed according to[10]

$$f_{Au}\frac{\varepsilon_r^{Au}-\bar{\varepsilon}_r^{Br}}{\varepsilon_r^{Au}+2\bar{\varepsilon}_r^{Br}}+(1-f_{Au})\frac{\varepsilon_r^{m}-\bar{\varepsilon}_r^{Br}}{\varepsilon_r^{m}+2\bar{\varepsilon}_r^{Br}}=0 \qquad \text{eq. 2.24}$$

where f_{Au} is the volume fraction of Au and (1 – f_{Au}) of the matrix (or air). The ligand shell is largely desorbed around this stage and so was neglected. We still need to use $\varepsilon_r^{Au} = \varepsilon_{r,nano}^{Au}$ as the nanostructure texture persists even after the percolative transition.

2.8.5 Simulation results

Dependence on core radius, shell thickness and medium refractive index. In the limit of small NP sizes (2r < 20 nm, much smaller than the wavelength of light so the assumption of homogeneous field is valid), the above theory is valid. $\tilde{\alpha}$ depends only slightly on the dielectric function of the solvent $\tilde{\varepsilon}^{matrix}$ (Fig. 2.7), the plasmon band position and intensity could vary with solvent. Figure 2.7 shows the computed plasmon resonance spectra for a range of solvents spanning optical refractive indices of 1.30 (trifluoroacetic acid) to 1.57 (trichlorobenzene) and for different sizes. It is clear that the dependence on practical solvent refractive indices is tiny. The plasmon band maximum redshifts by less than 1% from 534 nm (2.32 eV) at n = 1.3 to 537 nm (2.31 eV) at n = 1.6 for Au NPs with d = 2.8 nm, t = 0.72 nm and C = 2, on the other hand enhances the absorption cross-section by 20%.

Agreement with experiments: Experimentally, Alvarez et al[61] have noticed similar results, however the λ_{max} remain unchanged for gold nanoparticles with d = 2, 2.1, 2.2, 2.4, 2.5 and 3.2 nm protected separately by hexanethiol, octanethiol and dodecanethiol monolayers. In fact our

theory predicts the λ_{max} of only a small blue–shift of 3nm from d = 2 nm to d = 3 nm for C = 0.75 which is insignificant, however this 3nm shift may be useful for some sensing applications.

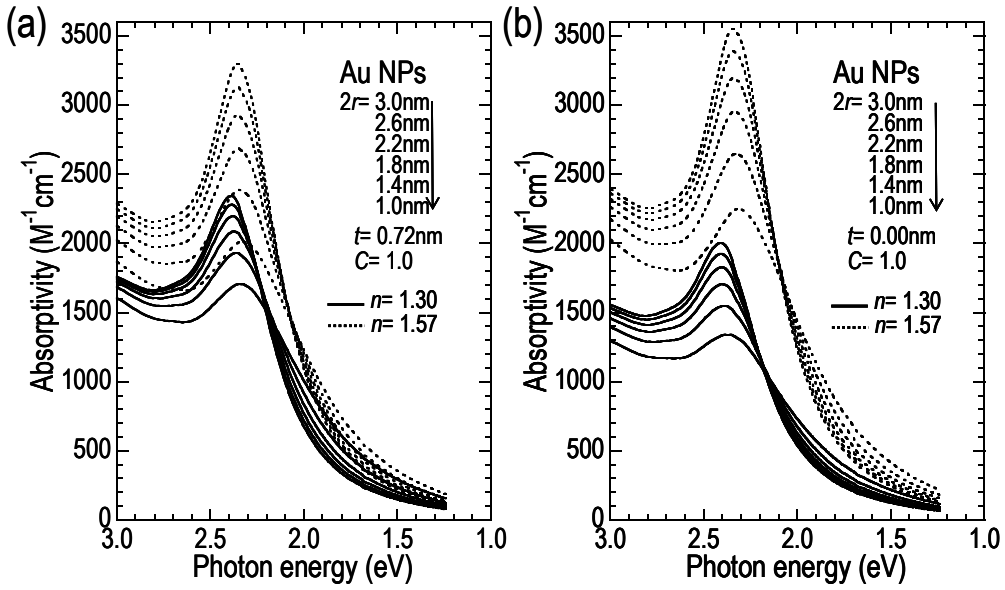

Fig 2.7 Plasmon resonance spectra of Au NPs as a function of varying NP-core-diameter, dielectric environment and shell thickness with scattering factor of 1.0 (a) Calculated spectra with shell thickness t = 0.72 nm (b) with shell thickness t = 0.0 nm.

Similar behavior was noticed by Hostetler et al as well that the λ_{max} doesn't change significantly for gold clusters of d = 2.2 – 4.4 nm protected by dodecanethiol monolayers.[7] Scaffardi et al also reported the same constant λ_{max} for particles of d = 1.2 to 3.6 nm protected by N-[3-(trimethoxysilyl)propyl]diethylenetriamine monolayers.[64] However they used core radius r to fit the experimental data while keeping C = 1.1, also to be noted. Link et al have reported that the λ_{max} red–shifts with increase in core–diameter for the particles with d = 9, 15, 22, 48 and 99 nm which was prepared by reducing Au ions with sodium citrate.[64, 70, 71] However the difference in λ_{max} between d = 9 nm to d = 22 nm was not much ($\Delta\lambda_{max}$ = 4 nm) and close to our theoretical

case study (not shown here). The red–shift of plasmon peak for d = 48 – 99 nm is in a regime where the mean free path of free electrons are no more limited by boundary restrictions.

This has been confirmed experimentally. Hostetler et al have found the consistency in λ_{max} (518nm) for the Au NPs of d = 2.2 – 4 nm, protected by dodeccanethiol in different solvents hexane (n = 1.375), THF (n = 1.407) and benzene (n = 1.501).[7] Templeton et al have observed a slight red–shift of 8nm on the position of λ_{max} on Au NPs in hexane (n = 1.375) and dichlorobenzene (n = 1.5515).[72] They also theoretically modeled their results using d = 5.2 nm, t = 1 nm and considering C = 1 as fitting parameter that produced near self–consistent results with the experiment. Gosh et al have found slightly different behavior of cytylpyridinium chloride stabilized Au NPs of d = 6±2nm prepared in toluene where they observed that the λ_{max} oscillates between 520 to 550 nm in wide range of solvents of refractive indices 1.3441 to 1.5054.[73] Underwood et al have reported the red–shift of ≈20 nm from cyclohexane (n = 1.376) to carbon–disulfide (n = 1.602) for Au NPs of d = 16±1.2 nm with a long chain length protecting ligand of copolymers of methylmethacrylate and gylcidylmethacrylate backbones with pendent side chain of poly(12–hydroxystearic acid).[74] Gómez et al, have found the λ_{max} (397 – 411 nm) doesn't vary significantly for poly(N–vinyl pyrolidone) protected Ag NPs of different core–diameter prepared in different solvents such as methanol (d = 4.9±1.2 nm), water (d = 6.3±2.7 nm), acetone and ethylene glycol (d = 4.3±2.5 nm).[75] Experimentally this effect has been noticed by Hostetler et al that the plasmon band intensity decreases from d = 4.4 nm to d = 2.2 nm and it disappears for d = 1.5 nm Au NPs protected by dodecanethiol monolayers dispersed in hexane solvent.[7] Alvarez et al also have observed the same effect that the plasmon band broadens with decrease in diameter and become unidentifiable for d = 1.7 and 1.4 nm.[61] The plasmon peaks (λ_{max}) remain unaltered

with increase in shell thickness except the negligible difference in absorption intensities of plasmon band. This makes sense that the dielectric function of nanoparticle dominates than the medium and shell dielectric functions. Experimentally Alvarez et al have noticed the same effect of constant λ_{max} centered at ≈518 nm (2.4eV) with an onset at 730 nm (1.7eV) for particles of diameter 1.4–3.2 nm protected by hexanethiol ($CH_3(CH_2)_5SH$), dodecanethiol ($CH_3(CH_2)_{11}SH$) and octadecanethiol ($CH_3(CH_2)_{17}SH$) which is consistent with our theoretical results.[61] Hostetler et al also reported that the λ_{max} unchanged (at 518nm) for Au NPs protected by butanethiol, octanethiol and dodecanethiol of d = 2 – 4 nm.[7] However Gosh et al reported a red–shift of ≈25 nm for Au NPs of d = 6.5 nm protected by cationic ligands of decyltrimethylammoniumchloride (t = 1.8 nm) and hexadecyltrimethylammoniumchloride (t = 2.57 nm).[73] Similar effect was noticed by them that the plasmon peak red–shifted (≈25 nm) when the anionic ligands of decylsodium sulfate (t = 1.82 nm) and sodiumdodecylbenzene sulfonate (t = 2.2 nm) were used as protection monolayers. However they have noted that the plasmon peaks remain unchanged for the particles protected by zwitterionic ligands of glycine and leucine. We can understand from these effects that the local field acts on the nanoparticle depends on the environment / shell atmosphere and hence the polarization.

In the case of metal NPs, the mean free path of free electrons is smaller, compared to that of the bulk metal, due to the boundary restrictions. Moreover the presence of crystal imperfections, defect sites and grain boundaries varies with respect to the preparation procedure and processing conditions of nanometal inks that can be attributed to core–quality, which comprises within scattering constant C. This can significantly alters the mean free path of free electrons that results in slight difference in λ_{max} in different results reported in the literatures.

2.9 Summary

We have studied the requirement of nanometal inks in terms of physical considerations such as optimal nanoparticle core diameter, insultor to metal transformation temperature of metal NP films, and its dispersibility in water and other polar solvents. The synthetic methodologies of metal NPs are reviewed with great care and the plasmon resonance band of metal films also understood. This helps us to design and develop a suitable nanometal ink system for printed and plastic electronics applications.

2.10 References

1. Faraday, M., *The Bakerian lecture: experimental relations of gold (and other metals) to light.* Phil. Trans. Roy. Soc. Lond., 1857. 147: p. 145 - 181.
2. Brust, M., M. Walker, D. Bethell, D.J. Schiffrin, and R. Whyman, *Synthesis of thiol-derivatised gold nanoparticles in a two-phase Liquid–Liquid system.* J. Chem. Soc., Chem. Commun., 1994: p. 801 - 802
3. Thomas, J.M., *Colloidal metals: past, present and future.* Pure Appl. Chem., 1988. 60: p. 1517-1 528.
4. Turkevitch, J., P.C. Stevenson, and J. Hillier, *A study of the nucleation and growth processes in the synthesis of colloidal gold.* Discuss. Faraday. Soc., 1951. 11: p. 55-75.
5. Brust, M., D. Bethell, C.J. Kiely, and D.J. Schiffrin, *Self-assembled gold nanoparticle thin films with nonmetallic optical and electronic properties.* Langmuir, 1998. 14: p. 5425-5429.
6. Hostetler, M.J., J.J. Stokes, and R.W. Murray, *Infrared spectroscopy of three-dimensional self-assembled monolayers: n-alkanethiolate monolayers on Au cluster compounds.* Langmuir, 1996. 12: p. 3604-3612.
7. Hostetler, M.J., J.E. Wingate, C.J. Zhong, J.E. Harris, R.W. Vachet, M.R. Clark, J.D. Londono, S.J. Green, J.J. Stokes, G.D. Wignall, G.L. Glish, M.D. Porter, N.D. Evans, and R.W. Murray, *Alkanethiolate gold cluster molecules with core diameters from 1.5 to 5.2 nm: Core and monolayer properties as a function of core size.* Langmuir, 1998. 14: p. 17-30.
8. Greer, J.R. and R.A. Street, *Mechanical characterisation of solution-derived nanoparticle silver ink thin films.* J. Appl. Phys., 2007. 101: p. 103529(1-5).
9. Perelaer, J., A.W. M. de Laat, C.E. Hendriks and U.S. Schubert, *Inkjet-printed silver tracks: low temperature curing and thermal stability investigation.* J. Mater. Chem., 2008. 18: p. 3209-3215.
10. Sivaramakrishnan, S., B.T. Anto, and P.K.H. Ho, *Optical modeling of the plasmon band of monolayer-protected nanometal clusters in pure and in polymer matrix thin films as a function of heat treatment.* Appl. Phys. Lett., 2009. 94: p. 091909.
11. Sivaramakrishnan, S., Chia P.J., Yeo Y.C., Chua L.L., and Ho P.K-H., *Controlled insulator-to-metal transformation in printable polymer composites with nanometal clusters.* Nat. Mater., 2007. 6: p. 149-155.
12. Wuelfing, W.P., F.P. Zamborini, A.C. Templeton, X. Wen, H. Yoon, and R.W. Murray, *Monolayer-protected clusters: Molecular precursors to metal films.* Chem. Mater., 2001. 13: p. 87 – 95.
13. Gamerith, S., A. Klug, H. Scheiber, U. Scherf, E. Moderegger, E.J.W. List, Dir*ect ink-jet printing of Ag–Cu nanoparticle and Ag-precursor based electrodes for OFET applications.* Adv. Funct. Mater., 2007. 17: p. 3111-3118.

14. Huang, D., F. Liao, S. Molesa, D. Redinger, and V. Subramanian, *Plastic-compatible low resistance printable gold nanoparticle conductors for flexible electronics.* J. Electrochem. Soc., 2003. 150: p. G412-G417.
15. Ko, S.H., J. Chung, H. Pan, C.P. Grigoropoulos and D. Poulikakos, *Fabrication of multilayers passive and active electric components on polymer using inkjet printing and low temperature laser processing.* Sensors and Actuators A, 2007. 134: p. 161-168.
16. Zhao, N., M. Chiesa, H. Sirringhaus, Y. Li, Y. Wu, and B. Ong, *Self-aligned inkjet printing of highly conducting gold electrodes with submicron resolution.* J. Appl. Phys, 2007. 101: p. 064513(1-6).
17. Terrill, R.H., T.A. Postlethwaite, C.-H. Chen, C.-D. Poon, A. Tarzis, A. Chen, J.E. Hutchison, M.R. Clark, G. Wignall, J.D. Londono, R. Superfine, M. Falvo, C.S. Johnson, Jr., E.T. Samulski, and R.W. Murray, *Monolayers in three dimensions: NMR, SAXS, thermal, and electron hopping studies of alkanethiold stabilised gold clusters.* J. Am. Chem. Soc., 1995. 117: p. 12537-12548.
18. Schmid, G. and B. Corain, *Nanoparticulated gold: synthesis, structures, electronics, and reactivities.* Eur. J. Inorg. Chem., 2003: p. 3081-3098.
19. Schmid, G. and A. Lehnert, *The complexation of gold colloids.* Angew-. Chem. Int. Ed. Engl., 1989. 28: p. 780-781.
20. Zallen, R., *The Physics of Amorphous Solids*. 1998: Wiley-VCH Verlag GmbH.
21. Shapiro, A.P. and R.F. Probstein, *Random packing of spheres and fluidity limits of monodisperse and bidisperse suspensions.* Phys. Rev. Lett., 1992. 68: p. 1422 - 1425.
22. Song, C., P. Wang, and H.A. Makse, *A phase diagram for jammed matter.* Nature, 2008. 453 p. 629 - 632.
23. Powell, M.J., *Computer-simulated random packing of spheres.* Powder Technol., 1980. 25: p. 45-52.
24. Lee, H.H., K.S. Chou, and K.C. Huang, *Inkjet printing of nanosized silver colloids.* Nanotechnol., 2005. 16: p. 2436-2441.
25. Chen, C.F., S.-D. Tzeng, H.-Y. Chen, K.-J. Lin, and S. Gwo, *Tunable plasmonic response from alkanethiolate-stabilized gold nanoparticle superlattices: Evidence of near-field coupling.* J. Am. Chem. Soc., 2008. 130: p. 824-826.
26. Martin, J.E., J.P. Wilcoxon, J. Odinek, and P. Provencio, *Control of the interparticle spacing in gold nanoparticle superlattices.* J. Phys. Chem. B, 2000. 104: p. 9475-9486.
27. Ho, P.K.H., J.-S. Kim, N. Tessler, and R.H. Friend, *Photoluminescence of poly(p-phenylenevinylene)-silica nanocomposites: evidence for dual emission by Franck-Condon analysis.* J. Chem. Phys., 2001. 115: p. 2709-2720.

28. Duineveld, P.C., *The stability of ink-jet printed lines of liquid with zero receding contact angle on a homogeneous substrate.* J. Fluid Mech., 2003. 477: p. 175-200.
29. Borel, J.-P., *Thermodynamical size effect and the structure of metallic clusters.* Surf. Sci., 1981. 106: p. 1-9.
30. Buffat, P. and J.P. Borel, *Size effect on the melting temperature of gold particles.* Phys. Rev. A, 1976. 13: p. 2287-2296.
31. Castro, T., Reifenberger, R., Choi, E., Andres, R. P., *Size-dependent melting temperature of individual nanometer-sized metallic clusters.* Phys. Rev. B, 1990. 42: p. 8548-8556.
32. Coombes, C.J., *The melting of small particles of lead and indium.* J. Phys. F: Metal Phys., 1972. 2: p. 441-449.
33. Ercolessi, F., W. Andreoni, and E. Tosatti, *Melting of small gold particles: mechanism and size effects.* Phys. Rev. Lett., 1991. 66: p. 911-914.
34. Lai, S.L., Guo J.Y., Petrova V.V., Ramanath G, Allen L.H., *Size-dependent melting properties of small tin particles: nanocalorimetric measurements.* Phys. Rev. Lett., 1996. 77: p. 99-102.
35. Wronski, C.R.M., *The size dependence of the melting point of small particles of tin.* Br. J. Appl. Phys., 1967. 18: p. 1731-1737.
36. Arcidiacono, S., S. Arcidiacono, N.R. Bieri, D. Poulikakos, C.P. Grigoropoulos, *On the coalescence of gold nanoparticles* Int. J. Multiphase Flow 2004. 30: p. 979–994.
37. Lewis, L.J., P. Jensen, and J.L. Barrat, *Melting, freezing, and coalescence of gold nanoclusters.* Phys. Rev. B, 1997. 56: p. 2248-2257.
38. Brust, M. and C.J. Kiely, *Some recent advances in nanostructure preparation from gold and silver particles: a short topical review.* Colloids and Surf. A, 2002. 202 p. 175–186.
39. Daniel, M. and D. Astruc, *Gold nanoparticles: assembly, supramolecular chemistry, quantum-size-related properties, and applications toward biology, catalysis, and nanotechnology.* Chem. Rev. , 2004. 104: p. 293-346.
40. Jana, N.R., L. Gearheart, and C.J. Murphy, *Seeding growth for size control of 5−40 nm diameter gold nanoparticles.* Langmuir, 2001. 17: p. 6782–6786.
41. Schmid, G., *Large clusters and colloids: Metals in the embryonic state.* Chem. Rev., 1992. 92: p. 1709-1727.
42. Ishizuka, H., et al., *Preparation of monodispersed colloidal gold by reduction of $AuCl_4^-$-cationic surfactant complexes.* Colloids Surf., 1992. 63: p. 337-340.
43. Giersig, M. and P. Mulvaney, *Preparation of ordered colloid monolayers by electrophoretic deposition.* Langmuir, 1993. 9: p. 3408-3413.

44. Weisbecker, C.S., M.V. Merritt, and G.M. Whitesides, *Molecular self-assembly of aliphatic thiols on gold colloids.* Langmuir, 1996. 12: p. 3763-3772.
45. Hirai, H. and H. Aizawa, *Preparation of stable dispersions of colloidal gold in hexanes by phase transfer.* J. Colloid Interface Sci. , 1993. 161: p. 471-474.
46. Swami, A., A. Kumar, and M. Sastry, *Formation of water-dispersible gold nanoparticles using a technique based on surface-bound interdigitated bilayers.* Langmuir, 2003. 19: p. 1168-1172.
47. Schaaff, T.G., G. Knight, M.N. Shafigullin, R.F. Borkman, and R.L. Whetten, *Isolation and selected properties of a 10.4 kDa gold:glutathione cluster compound.* J. Phys. Chem. B, 1998. 102(10643–10646).
48. Kim, K.-S., D. Demberelnyamba, and H. Lee, *Size-selective synthesis of gold and platinum nanoparticlesusing novel thiol-functionalised ionic liquids.* Langmuir, 2004. 20: p. 556-560.
49. Cliffel, D.E., F.P. Zamborini, S.M. Gross, and R.W. Murray, *Mercaptoammonium-monolayer-protected, water-soluble gold, silver, and palladium clusters.* Langmuir, 2000. 16: p. 9699-9702.
50. Templeton, A.C., S. Chen, S.M. Gross, and R.W. Murray, *Water-soluble, isolable gold clusters protected by tiopronin and coenzyme A monolayers.* Langmuir, 1999. 15: p. 66-76.
51. Longenberger, L. and G. Mills, *Formation of metal particles in aqueous solutions by reactions of metal complexes with polymers.* J. Phys. Chem. B, 1995. 99: p. 475-478.
52. Leff, B., L. Brandt, and J.R. Heath, *Synthesis and characterization of hydrophobic organically soluble gold nanocrystals functionalized with primary amines.* Langmuir, 1996. 12: p. 4723-4730.
53. Chen, S. and K. Kimura, *Synthesis and characterization of carboxylate-modified gold nanoparticle powders dispersible in water.* Langmuir, 1999. 15: p. 1075-1082.
54. Wuelfing, W.P., Gross S.M., Miles D.T., Murray R.W., *Nanometer gold clusters protected by surface-bound monolayers of thiolated poly(ethylene glycol) polymer electrolyte.* J. Am. Chem. Soc., 1998. 120: p. 12696-12697.
55. Kimura, K., H. Yao, and S. Sato, *Self-assembling of gold and silver nanoparticles at a hydrophilic/hydrophobic interface: A synthetic aspect and superstructure formation.* Synth. React. Inorg. Met.-Org. Chem. , 2006. 36: p. 237-264.
56. Zubarev, E.R., J. Xu, A. Sayyad, and J.D. Gibson, *Amphiphilic gold nanoparticles with v-shaped arms.* J. Am. Chem. Soc., 2006. 128: p. 4958-4959.
57. Uzun, O., Y. Hu, A. Verma, S. Chen, A. Centrone and F. Stellacci, *Water-soluble amphiphilic gold nanoparticles with structured ligand shells.* Chem. Commun., 2008.
58. Pike, G.E., Seager,C.H., *Percolation and conductivity : a computer study II.* Phys.Rev.B, 1974. 10: p. 1435-1446.

59. Pike, G.E. and C.H. Seager, *Percolation and conductivity : a computer study I.* Phys. Rev. B, 1974. 10: p. 1421-1434.
60. Kreibig, U. and L. Genzel, *Optical absorption of small metallic particles.* Surf. Sci., 1985. 156: p. 678-700.
61. Alvarez, M.M., J.T. Khoury, T.G. Schaaff, M.N. Shafigullin, I. Vezmar, and R.L. Whetten, *Optical absorption spectra of nanocrystal gold molecules.* J. Phys. Chem. B, 1997. 101: p. 3706-3712.
62. Mohamed, M.B., K.Z. Ismail, S. Link, and M.A. El-Sayed, *Thermal reshaping of gold nanorods in micelles.* J. Phys. Chem. B, 1998. 102: p. 9370-9374.
63. Granqvist, C.G. and O. Hunderi, *Optical properties of ultrafine gold particles.* Phys. Rev. B, 1977. 16: p. 3513-3534.
64. Scaffardi, L.B., N. Pellegri, O. de Sanctis and J.O. Tocho, *Sizing gold nanoparticles by optical extinction spectroscopy.* Nanotechnology, 2005. 16: p. 158-163.
65. Scaffardi, L.B. and J.O. Tocho, *Size dependence of refractive index of gold nanoparticles.* Nanotechnology, 2006. 17: p. 1309-1315.
66. Palik, E.D., *Handbook of optical constants of solids*. Vol. 1. 1998: New York: Academic press.
67. Aspnes, D.E., *Optical properties of thin films.* Thin Solid Films, 1982. 89: p. 249-262.
68. Born, M. and E. Wolf, *Principles of optics: electromagnetic theory of propagation, interference and diffraction of light*. 7 ed. 1999, Cambridge: Cambridge University Press.
69. Van de Hulst, H.C., *Light scattering by small particles*. 1957, New York: John Wiley & Sons.
70. Link, S. and M.A. El-sayed, *Shape and size dependence of radiative, non-radiative and photothermal properties of gold nanocrystals.* Int. Rev. Phys. Chem., 2000. 19: p. 409-453.
71. Link, S., M.B. Mohamed, and M.A. El-Sayed, *Simulation of the optical absorption spectra of gold nanorods as a function of their aspect ratio and the effect of the medium dielectric constant.* J. Phys. Chem. B, 1999 103: p. 3073-3077.
72. Templeton, A.C., J.J. Pietron, R.W. Murray, and P.Mulvaney, *Solvent refractive index and core charge influences on the surface plasmon absorbance of alkanethiolate monolayer-protected gold clusters.* J. Phys. Chem. B, 2000. 104: p. 564-570.
73. Gosh, S.K., S. Nath, S. Kundu, K. Esumi, and T. Pal, *Solvent and ligand effects on the localised surface plasmon resonance (LSPR) of gold colloids.* J. Phys. Chem. B, 2004. 108: p. 13963-13971.
74. Underwood, S. and P. Mulvaney, *Effect of the solution refractive index on the colour of gold colloids.* Langmuir, 1994. 10: p. 3427-3430.
75. Gómez, de Araújo C.B., Brito-Silva A.M., Galembeck A. , et al., *Solvent effects on the linear and nonlinear optical response of silver nanoparticles.* Appl. Phys. B, 2008. 92: p. 61-66.

3 Sparse ionic monolayer protected metal NPs: preparation and characterization

3.1 Introduction

Printable monolayer-protected metal nanoparticle (NP) inks have numerous potential applications especially as conductive electrodes and inter-connects in plastic electronics. As a processing requirement for these applications, the deposited (or printed) NP film has to be annealed to eliminate the protection monolayer and coalesce the film to a highly conductive bulk-like continuous metallic state. On this note a new concept of metal NPs protected by sparse monolayer of ionic ligands that can achieve extremely high water- and polar-solvent-dispersibility together with low solid-state coalescence temperature (for Au NPs as low as 145ºC) has been developed. The sparse assembly of ionic monolayers on metal NPs has been prepared through a controlled synthetic route, unlike the monolayer assembly of densely packed mixed ligand protection.[1] The metal NPs were initially protected by a two-component mixed ligand shell comprising a ω-functionalized ionic ligand and a labile ligand which was then selectively desorbed to give a sparse shell of the ω-ionic ligands of *ca*. 25% coverage. Until the demonstration of this current study, the possibility of low solid-state coalescence temperature and water or polar solvent dispersibility were regarded as mutually incompatible goals because the required ionic or ethylene glycol ligands raise coalescence temperature above 200ºC.[1-5] The sparse monolayer approach therefore greatly extends the application of NP metal films to organic substrates that are temperature and/or solvent sensitive. The concept is general (as it demonstrated also with Ag NPs), and thus opens up further interesting possibilities to "backfill" the NP surfaces with other self-assembled monolayers (SAMs) to develop novel functional materials. Detailed Fourier-transform infrared spectroscopy and X-ray

photoelectron spectroscopy of Au NPs protected by different ligand shells reveal the concept of sparse monolayer assembly on NPs and its significance in the insulator-to-metal transformation temperature (T_p).

3.2 Experimental

3.2.1 Preparation of Au NPs

Several key details of the Brust–Schiffrin process[6] have been modified in our approach. In a typical preparation, (150 mg, 0.44 mmol) of $HAuCl_4$ was dissolved in Millipore water (10 mL). Tetraoctylammonium bromide ("TOAB", 362 mg, 0.66 mmol, 1.5 eq) was dissolved in HPLC toluene (25 mL) in an Erlenmeyer flask. $HAuCl_4$ was added to the TOAB solution and stirred for a few min. After complete phase transfer of $AuCl_4^-$ to the organic phase, the acidic aqueous phase (pH 2.5) was optionally removed and the toluene phase was washed with Millipore water twice. [For reproducibility, we found it is best to remove the aqueous layer after complete phase transfer of $AuCl_4^-$ to the toluene layer before addition of the thiols.] The desired thiol was then added. 6-mercaptohexanoic acid (MHA) (2.97 mg, 0.020 mmol) and 3-mercaptopropanol (MPL) (18.5 mg, 0.20 mmol) was added for example, to make Au NPs protected by a feed ratio of 1:10 MHA and MPL. The Au to S mol ratio was kept in all cases at 2 for 3-nm-diam, and 6 for 13-nm-diam Au NPs. Freshly-prepared sodium borohydride (134 mg, 3.53 mmol, 8 eq) in Millipore water (5 mg mL^{-1}), followed optionally by another 10 mL Millipore water, was added dropwise over tens of min. Increasing the $NaBH_4$ concentration causes premature aggregation of the Au NPs to give intractable products. The NPs were first formed in the toluene layer and then transferred to the aqueous layer as reduction proceeds. The aqueous layer was collected, washed with methanol and precipitated with THF. The precipitate was re-dispersed in water and precipitated with THF typically for 5–7 times, until small aliquots extracted from the dispersion give the correct T_p after

drying. During these purification cycles, the tetraoctylammonium bromide surfactant was progressively removed. The material was finally dispersed in water or another solvent (e.g., ethylene glycol) to the desired concentration. Typical yield is > 80 % of its theoretical yield. Acidification with concentrated HCl leads to precipitation of the acid form of the ligand-protected Au NPs from water. Basification with NaOH leads to complete re-dispersion.

3.2.2 Preparation of Ag NPs

In a typical preparation, 100 mg of $AgNO_3$ was dissolved in a Millipore water–methanol mixture (1:1 v/v, 20 mL). The desired thiol was added. MHA (3.62 mg, 0.024 mmol) and MPL (24.9 mg, 0.27 mmol) were added. The Ag/S mol ratio was 2:1 for 14-nm-diameter Ag NPs. Freshly-prepared $NaBH_4$ (112 mg, 2.96 mmol, 5 eq.) was added dropwise immediately with stirring. The solution turned dark brown, and was further stirred for 2 h at room temperature. Excess methanol (200 mL) was added to precipitate the Ag NPs, which were then purified by repeated re-dispersion in water (20 mL), and precipitation with THF (200 mL), typically 4–5 times, until small aliquots of the dispersion give the desired T_p after drying.

3.2.3 Ligand shell characterization spectroscopy

The sparse monolayer assembly on metal NPs was decoded using Fourier transform infrared (FTIR) spectroscopy by analyzing the key molecular vibrational bands present in the protective monolayers. FTIR spectra were taken on Nicolet 8700 FTIR spectrometer at a resolution of 4 cm^{-1} / 150 scans. Samples of Au NP films were deposited onto the intrinsic silicon wafers at ambient conditions and annealed at different temperatures in a N_2 glove box. The relative empirical

integrated absorption cross-sections, vide infra, of various functional groups were determined from model compounds to be: $\nu_{as}COO^-$ (1.0), $\nu C{=}O_{acid}$ (0.9), $\delta C\text{-}OH_{alcohol}$ (0.35), and δCH_2 (0.42).

Relative integrated absorption cross-sections: We compared the absorption band intensities of the following pairs of model compounds (solid-state spectra in KBr): (i) hexanoic acid and sodium hexanoate, and (ii) lactic acid and lithium lactate, to obtain the relative cross-sections of the $\nu_{as}COO^-$, $\nu C{=}O_{acid}$ and δCH_2 bands using the CH_3 band intensity as internal reference. We then checked for self-consistency using the following compounds: 3-mercaptopropionic acid, hydroxypropionic acid, and sodium hydroxbutyrate, from which we also determined the relative cross-section of the $\delta C\text{-}OH_{alcohol}$ band. The relative integrated absorption cross-sections per functional group were thus determined to be: $\nu_{as}COO^-$ (1.0), $\nu C{=}O_{acid}$ (0.9), $\delta C\text{-}OH_{alcohol}$ (0.35), and δCH_2 (0.42). As the actual cross-sections can vary with the local molecular environment, in particular hydrogen-bonding, these values are only semi-quantitative, but sufficiently accurate for our purpose. From the self-consistency achieved, we estimated the error to be ±20 % from such effects. It is known from the literature that there will be a significant shift in the absorption band position with respect to counter ions of carboxylate salts.[8] However the band position's linear relation with the electronegativity of counter ions[8] is not general, as the relation between the mass of the counter ions and frequency was also reported.[9, 10] However these effects don't affect our calculation of integrated absorption cross-sections. To ensure whether there is any such effects in absorption cross-sections of carboxylate salts of different counter ions, we cross verified with FTIR spectra of the phenyl stearic acid, and its salts of Li, Na, K and Ca. It is found that the results were self-consistent. Furthermore, the presence of the metal NPs can enhance the FTIR absorption cross-sections of the ligand shell. We found experimentally that the normalized integrated band intensities of key functional groups in the ligand shell increase weakly with

decreasing average distance of the Au NPs diluted in a polyelectrolyte matrix. Thus as ligand shell desorption occurs, the core–core separation decreases, and we expect FTIR sensitivity to the residual SAM shell to increase slightly. However this effect is weak and applies to all the absorption bands and so FTIR provides valid quantitative comparisons of the molecular composition of the shell.

3.2.4 X-ray photoelectron spectroscopy

Core-level and survey X-ray photoelectron spectra were acquired on a ESCALAB MKII spectrometer at a base pressure better than 10^{-9} mbar using Mg $K\alpha_{1,2}$ X-ray photons (1253.6 eV) irradiating 54.7° relative to electron analyzer entrance. The photoejected electrons were analyzed by a concentric hemispherical analyzer operated at constant pass energy of 20 eV for core level spectra and 50 eV for survey spectra. The photoemission angle (θ) was set at 90° (normal). The X-ray gun was operated at 150 W and emission distributed over an area of about 5 mm diameter on the substrate at θ = 90°. Sample charging was insignificant as the conductive silver paint provides better contact for samples that were on polycrystalline gold coated silicon substrates, and electron flood gun operation was not necessary.

Core-level spectra were processed by linear background subtraction and displayed normalized to the intensity of the specified core levels. For atomic stoichiometries, the integrated intensities were corrected with empirical sensitivity factors taking into account the atomic photoionization cross sections, the electron inelastic mean free path, and the spectrometer intensity-energy response function. The quantification error is expected to be ±10% from systematic effects. The relative empirical sensitivity factors of various atomic elements from model compounds to be: F 1s(1.00),

Au 4f (6.42), S 2p (0.693), C 1s (0.32), O 1s (0.727), Na 1s (1.652), N 1s (0.496) and Br 3d (1.08). We can argue that the XPS may not be a good method to calculate the monolayer density on Au NPs, as only the surface atoms of NPs and ligand shells are exposed to x-rays. However the relative error, after empirical atomic sensitivity factor and differential escape depth corrections, are uniform throughout and self sufficient for our purpose to calculate sparse & dense ligand shells. And we also found that the results are self-consistent with the FTIR analysis.

3.2.5 Optical transmission spectroscopy

Optical transmission spectra of (i) MHA & MPL and (ii) MHA & and 4-mercaptobutanol (MBL) mixed monolayer protected pure Au NPs in water was collected in a UV-Vis spectrometer and normalized to 1 @ 350nm.

Thin film spectra: The MHA+MPL_Au NP sample on a fused silica substrate was dried at ambient and its spectrum recorded in a N_2-purged UV-Vis spectrometer. Initial film thickness was 55 nm; final thickness was 35 nm.

3.3 Results and discussion

Recent development demonstrates stable dispersions at the required concentrations can be achieved in water and other polar solvents by using mixed ω-carboxy- and ω-hydroxy-alkylthiols (ω-mercaptohexadecanoic acid MHDA and ω-mercaptoundecanol MUL).[1] The mixed monolayer apparently promotes dispersibility by decreasing intra-shell ionic bonding. Other mixed ionic monolayers of mercaptoundecane-sodiumsolfonate and octanethiol also give highly water-dispersible Au NPs.[3] These materials can be further homogeneously blended at very high volume ratios (>70 vol%) into polyelectrolyte matrices to give good film cohesion and substrate adhesion.[1] This overcomes the tensile stress from the large sintering volume loss. The

MHDA+MUL–Au NPs exhibit a percolative insulator-to-metal transition $T_p \approx 210$ºC (in the dc electrical conductivity σ_{dc}).[1] This is a practical measure of the coalescence temperature. However the sparse-monolayer-protected metal NPs can achieve the desired solubility characteristics and low T_p.

Nearly monodispersed (standard deviation ±30%) monolayer-protected Au NP systems with similar core diameters were prepared through a modified Brust–Schiffrin process with different thiols. Table 3.1 summarizes the ligand shell structure, combination, and other properties obtained. Contamination with the tetraoctylammonium bromide surfactant used in the synthesis is only ≈ 3 mol% of ligands (calculated from the XPS measurements), as in other reports.[7]

Table 3.1: Summary of sparse and dense monolayer protected Au NPs

S/No	Shell notation	Protection thiol (feed mol ratio, if relevant)	T_p (ºC)[a]	Actual ligand shell composition (mol ratio)[b]	Remarks[c]
1a	MHA_{salt}	$HOOC(CH_2)_5SH$	220	$COOH(0.3)$, $COO^-(0.7)$	d = 28 ± 09 t = 7.8± 0.75
1b	MHA_{acid}	$HOOC(CH_2)_5SH$	170	COOH (1.0)	
2	BT	$CH_3(CH_2)_3SH$	130		d = 38 ± 12
3	MHA+BT	$HOOC(CH_2)_5SH$: $CH_3(CH_2)_3SH$ 1 : 10	200	MHA:BT = 1:11.5 $COOH(0.04)$, $COO^-(0.04)$, BT(0.92)	d = 24 ± 8 t = 9.3 ± 1.4
4	MHA+MPL	$HOOC(CH_2)_5SH$: $HO(CH_2)_3SH$ 1 : 10	145	MHA:MPL = 5:1 $COOH(0.31)$, $COO^-(0.52)$, $OH(0.17)$	d = 32 ± 10 t = 6.7 ± 0.75
5	MHA+MBL	$HOOC(CH_2)_5SH$: $HO(CH_2)_4SH$ 1 : 10	180	MHA:MBL = 2.2:1 $COOH(0.66)$, $COO^-(0.03)$, $OH(0.31)$	d = 27 ± 07
6	MHDA+MUL	$HOOC(CH_2)_{16}SH$: $HO(CH_2)_{11}SH$ 1 : 5.5	210	MHDA:MUL = 1: 3.8 $COOH(0.15)$, $COO^-(0.06)$, $OH(0.79)$	d = 33 ± 10 [d]

[a] T_p is the percolation temperature taken to be the mid-point of the morphological insulator-to-metal transition measured in dc electrical conductivity plotted on the log scale.

[b] Composition mole ratio of the ligand shell obtained from FTIR terminal group analysis: COOH = acid and COO^- = salt forms of ω-carboxyl groups, and OH = ω-hydroxyl groups; expressed as mol ratio of the total SAM.

[c] *d* is the average NP Au-core diameter in Å, measured by TEM; *t* is the average shell thickness in Å, taken to be half of the inter-particle spacing for contact pairs.

[d] Data re-evaluated from Ref. [1]

3.3.1 Densely packed mixed monolayer protected Au NPs

The MHA–Au NPs were produced and purified in a mixed acid+salt form. XPS corrected by empirical atomic sensitivity factors (see Experimental)[11] gave the stoichiometry to be $S_{1.0}O_{2.9}C_{9.5}N_{0.05}Br_{0.10}Na_{0.85}Au_{3.3}$, while Na/S and Na/O ratios corrected for differential escape depths gave 60±5 mol% of MHA in the Na^+ salt form (i.e., Na^+ $^-OOC(CH_2)_5S$–Au, the balance being $HOOC(CH_2)_5S$-Au) (table 3.1, entry 1a). Integrated FTIR intensities deduced from FTIR spectra (fig 3.1) of the $\nu_{as}COO^-$ (1567 cm^{-1}) and $\nu C{=}O_{acid}$ (1700 cm^{-1}) bands, corrected also by empirical absorption cross-sections, are in agreement (70±15 mol% salt form). These MHA-Au NPs are extremely soluble in water (> 50 mg mL^{-1}) to give dark brown solutions.

To understand the quantitative aspects of the FTIR spectra of these ligand shells, it is important to consider the effects of the metal nanocores on their vibrational absorption cross-sections. We learnt from the work done along with my colleague Sivaramakrishnan on optical modeling of vibrational spectra of the shell assuming isotropic cross-sections in the van de Hulst polarization formalism in a transfer matrix to describe overall reflection, interference and absorption effects.[12]

We found that the absorption cross-sections are uniformly enhanced across the vibrational spectrum by a significant factor depending on shell thickness (enhancement ratio ≈ 2 for a shell

thickness (*t*) of 1 nm, increasing to ≈ 5 for *t* = 0.2 nm).[12] This enhancement factor is practically constant across the entire vibration spectrum. As ligand-shell elimination progresses, core separation decreases, the shell absorption cross-section increases. Absorption intensities thus track the amount of residual functional groups in the shell although non-linearly but the relative effect is similar across all groups.

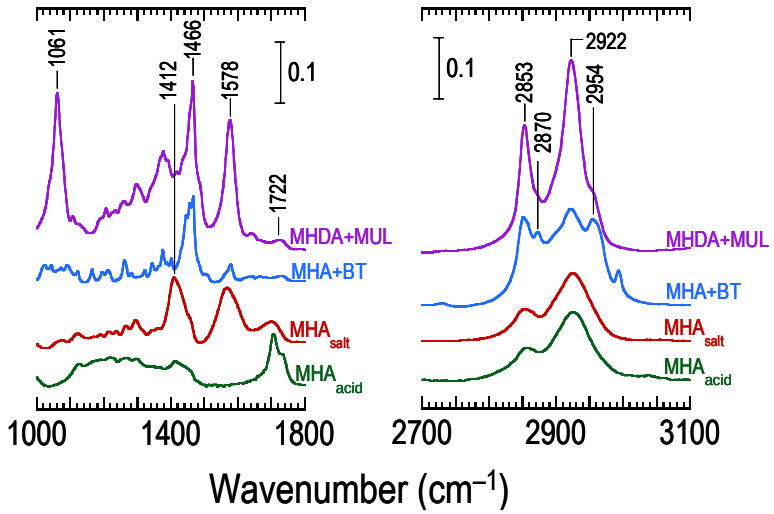

Figure 3.1 Dense monolayer protected Au NPs: FTIR spectra of Au NPs protected by dense monolayers of (i) 6-mercaptohexanoic acid, as prepared (MHA_{salt}) (ii) 6-mercaptohexanoic acid, post synthesis acidification (MHA_{acid}) (iii) 6-mercaptohexanoic acid-butanethiol (1:10 mol/mol) mixed monolayers (MHA+BT) (iv) 16-mercaptohexadecanoic acid-11-mercaptoundecanol (1:5.5 mol/mol) mixed monolayers (MHDA+MUL) *((iv) data replotted from ref.[1])*

Acidification with concentrated HCl produces a black precipitate of COOH-terminated Au NPs (i.e., MHA_{acid}–Au). This was confirmed by complete disappearance of ν_s and $\nu_{as}COO^-$ bands and emergence of $\nu C{=}O_{acid}$ (1708, 1738 cm^{-1}), $\nu C{-}OH_{acid}$ (1299 cm^{-1}) and $\delta CO{-}H_{acid}$ (1414 cm^{-1}) bands[13] (fig. 3.1). However these NPs are no longer dispersible in H_2O, but in MeOH and alcohols. Thus the tail group controls solubility characteristics.[1] In both MHA_{salt}– and MHA_{acid}–Au NPs, the alkyl chain conformations are disordered (ν_sCH_2 2854–2858 and $\nu_{as}CH_2$ 2924 cm^{-1};

compared with all-*trans* values of 2846–2850 and 2915–2920 cm^{-1}, and liquid values of 2856 and 2928 cm^{-1} respectively).[14-18]

We further our investigation with Au NPs protected by a mixture of MHA and hydrophobic BT ligands in the molar ratio of 1:10 (Table 3.1, entries 2 & 3) as BT ligand protected Au NPs are known for lower T_p but soluble in toluene. These MHA+BT–Au NPs are however not dispersible in H_2O or MeOH but in toluene. From the integrated band intensities of δCH_2, $\nu_{as}COO^-$ and $\nu C{=}O_{acid}$, the ligand ratio [MHA]/[BT] incorporated into the ligand shell was found to be 0.085±0.015 (with 50 mol% of MHA in salt form) for a feed ratio of 0.10. Therefore these two thiols are assembled nearly statistically into the shell. The $\nu C{=}O_{acid}$ gives non hydrogen-bonded (1730 cm^{-1}) species, as the MHA ligands were separated by the BT ligands, which supports this picture (fig. 3.1). This suggests a preferred ionic and/or hydrogen bonding between MHA on neighboring NPs that hold apart the Au cores and suppress coalescence, which could be useful for some applications.

In case of Au NPs protected by a mixture of MHDA and MUL ligands (Table 3.1, entry 6), FTIR integrated band intensities of δCH_2, $\nu_{as}COO^-$ and $\nu C{=}O_{acid}$ gives the actual ligand shells composition [MHDA]/[MUL] = 0.26, comparable to feed ratio of [MHDA]/[MUL] = 0.18, which is self consistent with the behaviour of MHA+BT–Au NPs ligand shells composition. It is also evidenced from XPS, by considering the O/S and C/S ratios, that the actual [MHDA]/[MUL] ratio is 0.2, which is closer to the feed ratio.

3.3.2 Sparse monolayer protected Au NPs

The investigation was furthered to Au NPs protected by a mixture of MHA and hydrophilic 3-mercaptopropan-1-ol (MPL) ligands. For reproducibility, the aqueous layer of this particular synthesis has to be removed after phase-transfer of $AuCl_4^-$ to the toluene layer and before addition of the thiols. Otherwise MPL gets extracted into water, with which it is freely miscible in all proportions. These MHA+MPL–Au NPs are extremely dispersible in water and alcohols (> 60 mg mL^{-1} in water and >200 mg ml^{-1} in ethylene glycol), and can be repeatedly isolated and purified by THF precipitation and H_2O dispersion in the "wet" state. Crucially, they exhibit $T_p \approx 145$ºC (Table 3.1, entry 4), which is the lowest temperature achieved to date for water-dispersible Au NPs. The final purified water dispersion is stable for ≈ 6 months in ambient, and indefinitely stable in the presence of a polyelectrolyte such as PEDT:PSSH (vide infra).

FTIR and XPS interestingly reveal that these NPs are protected by only a sparse monolayer (i.e., a sub-monolayer of *ca*. 10% coverage) of partially-ionized MHA. XPS gave a stoichiometry of $S_{1.0}O_{2.45}C_{6.5}N_{0.0}Br_{0.0}Na_{0.3}Au_{14}$, with a Au/S ratio that is 4 times as high as in conventional monolayer-protected NPs (3.3 ± 0.05, for MHA– and MHDA+MUL–Au NPs). Sulfur atom has the foot print area (≈ 28 Å), which is three times that of Au atomic foot print area. Hence the Au/S ratio should be about 3, as the photoelectron can only be able to see the Au atoms on the surface of NPs, for the maximum monolayer density on the NP surface. This effect has been evidenced for other dense monolayer protected Au NPs such as MHA, MHDA+MUL and MHA+BT from XPS. FTIR (fig. 3.2) shows the diminishing $\delta C–OH_{alcohol}$ band in MHA+MPL–Au NPs compared to strong $\delta C–OH_{alcohol}$ band (1061cm^{-1}) corresponds to MUL ligand shell in the dense assembly of MHDA+MUL–Au NPs. This suggests a thiol surface coverage of only *ca*. 25% of the conventional

NPs. Furthermore XPS O/S and C/S ratios gave a shell [MHA]/[MPL] = 4.5±0.5, for a feed [MHA]/[MPL] = 0.10. This shows the sparse shell is mainly MHA even though the feed is MPL-rich. This effect is confirmed by FTIR intensities (fig. 3.2) of the $\nu C{=}O_{acid}$, $\nu_{as}COO^-$ and $\delta C{-}OH_{alcohol}$ bands[13] which found a shell [MHA]/[MPL] = 5±1. Therefore although as-synthesized the Au NPs are likely to have a shell composition imposed by the thiol feed ratio, during purification they become severely depleted in MPL to leave a sparse monolayer of the ionized MHA ligands. The reason for this is the selective desorption of MPL during purification (solubility of MHA, 12 mg mL^{-1}; MPL, ∞ in water) as it has been established that thiol SAM desorption becomes increasingly favorable in solvents in which they are soluble.[19] Previously, this has been exploited to exchange thiols at defect sites and grain boundaries.

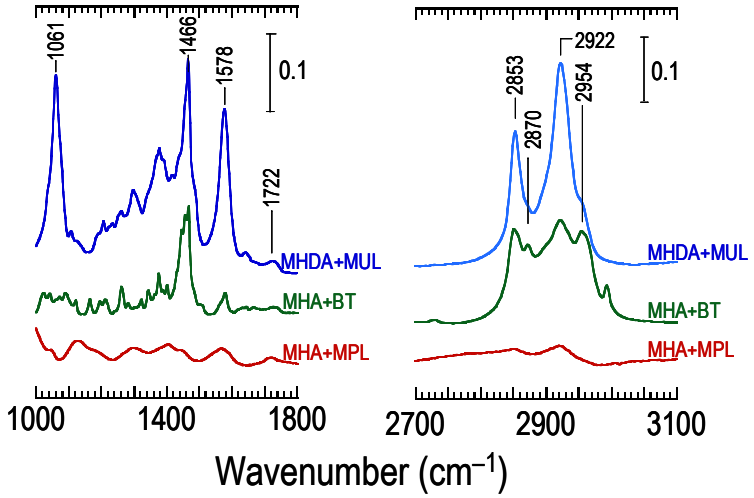

Figure 3.2 Sparse monolayer protected Au NPs: (bottom to top) FTIR spectra of Au NPs protected by (i) 6-mercaptohexanoic acid-3-mercaptopropanol ligands (for 1:10 mol/mol feed) sparse monolayers (MHA+MPL) (ii) 6-mercaptohexanoic acid-butanethiol (for 1:10 mol/mol feed) mixed dense monolayers (MHA+BT) and (iii) 16-mercaptohexadecanoic acid-11-mercaptoundecanol (for 1:5.5 mol/mol feed) mixed dense monolayers (MHDA+MUL) are plotted for comparison *((iii) data replotted from ref.[1])*

Here an extensive selective desorption turns out to be the key to provide a sacrificial template for assembly of a controlled low density of MHA SAM through desorption of the intervening sacrificial

SAM. This successfully reduces the effective shell thickness while keeping sufficient ion density for dispersibility in polar solvents. A schematic picture of these sparse-ionic monolayer NPs is shown in Fig. 3.3.

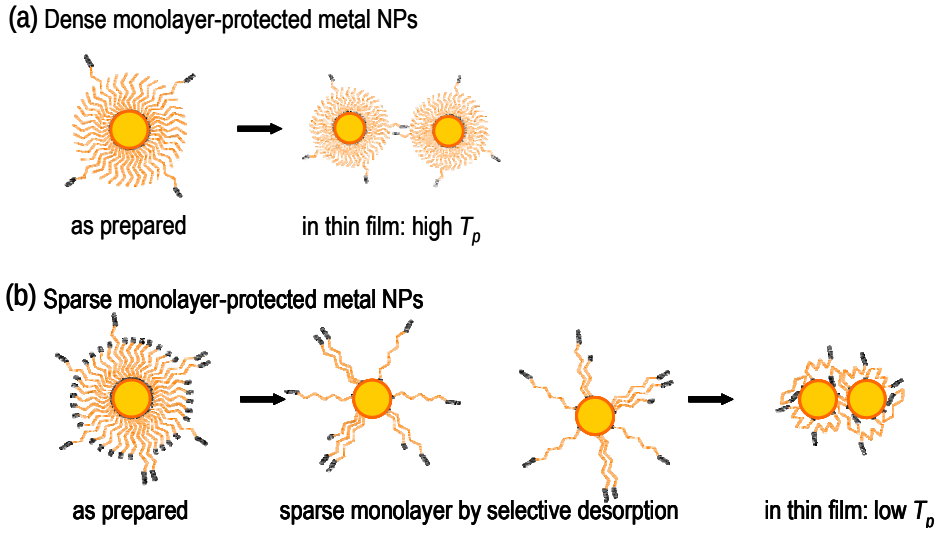

Fig 3.3 Sparse monolayer protected metal NPs: Schematic diagram of a) dense monolayer-protected, and, b) sparse monolayer-protected metal NPs.

When a mixture of MUL and MHDA is used (Table 3.1 entry 6),[1] the shell [MHDA]/[MUL] = 0.26 ± 0.05 (FTIR) and 0.20 ± 0.02 (XPS), which is practically the same as the feed ratio of 0.18. Therefore as in the case of MHA+BT for which desorption in water does not occur significantly, the shell composition follows the feed composition without any significant discrimination between ω-hydroxy- and ω-carboxy-alkylthiols. It is also clear there is no significant phase separation within the shell. The $\nu C{=}O_{acid}$ for MHA+BT (1645–1730 cm^{-1}), MHA+MPL (1720 cm^{-1}), MHDA+MUL (1725 cm^{-1}) are similar but not identical with MHA (1708, 1736 cm^{-1}). Therefore there is interaction between the ω-COOH probably in statistical clusters, but not large patches, as in previous work

showing molecular-level mixing[14, 20] or at most nanometer-sized domains,[21, 22] even between very dissimilar SAMs.

3.3.3 Suppression of micro-crack formation in Au NP films

In case of Au NP-polymer composites, polymer chains passes over several NPs through the interparticle spaces to bind them together. In this role, it is distinct from polymeric dispersants that are associated only with the NP and so is not effective to bind neighbors together. Intimate molecular mixing is confirmed by FTIR for Au NP systems with anionic surface groups due to favorable interaction with the cations. The protection monolayers are in the ionic $–COO^-$ form, confirmed by FTIR spectroscopy, which should afford favorable ionic interactions with the PEDT polyelectrolyte complex. This is confirmed by the upshift in $\nu_{as}COO^-$ from 1567 to 1594 cm^{-1} by counterion exchange with PSS anions and downshift in $\nu C{=}O_{acid}$ from 1720 to 1709 cm^{-1} by hydrogen bonding with PSSH.

In case of sparse–monolayer protected nano–Au–PEDT films, the insulator–to–metal transformation up–shifted by 10°C for Au–90vol% due to compatibilization through the surface ionic groups.[1]

3.3.4 Generality of sparse monolayer approach on metal NPs

Au NPs protected by the mixture of MHA and MBL ligands, in which MBL is less soluble (60 mg mL^{-1}) than MPL, but more than MHA, was studied (Table 3.1, entry 5). FTIR integrated abosprtion intensities gave shell composition, [MHA]/[MBL] = 2.2 ± 0.4, which though still considerably depleted in MBL than the feed ratio of [MHA]/[MBL] = 0.1, is less than that with MPL as co-ligand.

The generality of the principle is further examined by preparing MHA+MPL (1:10, feed ratio) protected Ag NPs, which also polar solvent-soluble and low-T_p. These Ag NPs were prepared by a $NaBH_4$ reduction of $AgNO_3$ in a single-phase 1:1 vol/vol water/methanol solvent mixture in the presence of a feed mixture of 1:10 MHA/MPL with a Ag/S mol ratio of 2. We obtained 14 nm diameter Ag NPs, which showed similar $T_p \approx 155$ ºC (see chapter 4 for details) and extremely high solubility in ethylene glycol, 250 mg mL^{-1}.

3.3.5 Inter-particle separation in sparse monolayer protected Au NPs

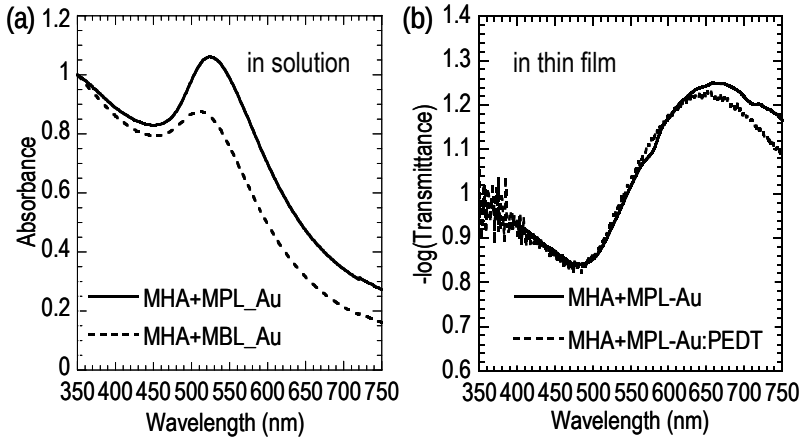

Figure 3.4 Sparse monolayer protected metal NPs: Plasmon resonance spectra of Au NPs (a) MHA+MPL–Au NPs and MHA+MBL–Au NPs in water. (b) MHA+MPL–Au NPs and MHA+MPL–Au NP:PEDT, 70:30 vol/vol. Both spectra are normalized to 1 at 350 nm

The primary effect of the sparse monolayer is then to reduce the core separation in the as-deposited films. This is confirmed by a large red shift of the plasmon band of MHA+MPL–Au NP thin films to 650 nm (Fig. 3.4) from 540 nm for the MHDA+MUL-Au NPs.[1] However the plasmon band of these NPs in solution (526 nm) is similar to the dense monolayer protected NPs, (fig. 3.4) which suggests that the sparse monolayer chains of MHA is not lying on the NP surface. The optical modeling of plasmon band shows that this band red shifts with increased coupling between

Au NPs.[2] The as-deposited film is already golden in color (however this does not necessarily imply core-core coalescence)[2], with $\sigma_{dc} \approx 60$ S cm^{-1} due to short tunneling gap ($2t$ = 1.3 nm) between the NPs.

In the solid state, the sparse monolayer is compacted on the surface of the NP, as evidenced by direct measurement of the shell thickness (t) by transmission electron microscopy (TEM). This was obtained as half of the separation of the cores at contact. The results gave for the MHA+MPL shell t = 6.7±0.75 Å, which is limited by the van der Waals thickness of a CH_2 chains lying on the NP surface. This is consistent with FTIR (fig 3.1 & 3.2) which indicates the presence of all-*trans* CH_2 chains, $\nu_{as}CH_2$ 2920 cm^{-1}, which is more red-shifted than MHA+MBL (2924 cm^{-1}) MHA (2924 cm^{-1}), BT (2925 cm^{-1}) and even DT (2922 cm^{-1}) and MHDA+MUL (2922 cm^{-1}) protected Au NPs. For comparison, MHA shell gave t = 7.8±0.75 Å; MHDA+MUL shell, 8.2±1.2 Å; BT shell, 8.6±1.4 Å; DT shell, 7.3±0.9 Å, MHA+BT shell, 9.3±1.4 Å. Thus ω-carboxy-alkylthiols give thinner shells than alkylthiols, probably as a result of end-group hydrogen- and/or ionic-bonding that constrained the in-plane density of the chains.

3.4 Summary

In summary, we have developed the sparse-ionic monolayer protected water soluble Au NPs. The sparse-assembly of the monolayers has been understood by the systematic characterization and analysis through FTIR, XPS and UV-Vis spectroscopic techniques. The principle is general as it has been demonstrated also for Ag NPs.

3.5 References

1. Sivaramakrishnan, S., Chia P.J., Yeo Y.C., Chua L.L., and Ho P.K-H., *Controlled insulator-to-metal transformation in printable polymer composites with nanometal clusters.* Nat. Mater., 2007. 6: p. 149-155.
2. Sivaramakrishnan, S., B.T. Anto, and P.K.H. Ho, *Optical modeling of the plasmon band of monolayer-protected nanometal clusters in pure and in polymer matrix thin films as a function of heat treatment.* Appl. Phys. Lett., 2009. 94: p. 091909.
3. Uzun, O., Y. Hu, A. Verma, S. Chen, A. Centrone and F. Stellacci,, *Water-soluble amphiphilic gold nanoparticles with structured ligand shells.* Chem. Commun., 2008.
4. Wuelfing, W.P., Gross S.M., Miles D.T., Murray R.W., *Nanometer gold clusters protected by surface-bound monolayers of thiolated poly(ethylene glycol) polymer electrolyte.* J. Am. Chem. Soc., 1998. 120: p. 12696-12697.
5. Wuelfing, W.P., F.P. Zamborini, A.C. Templeton, X. Wen, H. Yoon, and R.W. Murray, *Monolayer-protected clusters: Molecular precursors to metal films.* Chem. Mater., 2001. 13: p. 87 – 95.
6. Brust, M., M. Walker, D. Bethell, D.J. Schiffrin, and R. Whyman, *Synthesis of thiol derivatised gold nanoparticles in a two phase liquid-liquid system.* J. Chem. Soc., Chem. Commun., 1994: p. 801-802.
7. Waters, C.A., Mills A.J., Johnson K.A., Schiffrin D.J., *Purification of dodecanethiol derivatised gold nanoparticles.* Chem. Commun., 2003: p. 540-541.
8. Kagarise, R.E., *Spectroscopic studies on the soaps of phenylstearic acid. I. Infrared absorption spectra and the hydrolysis of soap films.* J. Phys. Chem., 1955. 59: p. 271–277.
9. ELLIS, B. and H. PYSZORA, *Effect of the metallic ion on the infra-red spectra of salts of carboxylic acids.* Nature, 1958. 181: p. 181 - 182.
10. Miller, F.A. and C.H. Wilkins, *Infrared spectra and characteristic frequencies of inorganic ions.* Anal. Chem., 1952. 24: p. 1253–1294.
11. Kim, J.S., P.K.-H. Ho, C.E. Murphy, and R.H. Friend, *Phase separation in polyfluorene-based conjugated polymer blends: lateral and vertical analysis of blend spin-cast thin films.* Macromolecules, 2004. 37: p. 2861-2871.
12. Sivaramakrishnan, S., B.T. Anto, and P.K.H. Ho, *Unpublished results*. 2009.
13. Colthup, N.B., L.H. Daly, and S.E. Wiberley, *Introduction to infrared and Raman spectroscopy*. 1990, San Diego: Academic Press, Inc.
14. Bertilsson, L. and B. Liedberg, *Infrared study of thiol monolayer assemblies on gold: preparation, characterisation, and functionalisation of mixed monolayers.* Langmuir, 1993. 9: p. 141-149.

15. Hostetler, M.J., J.J. Stokes, and R.W. Murray, *Infrared spectroscopy of three-dimensional self-assembled monolayers: n-alkanethiolate monolayers on Au cluster compounds.* Langmuir, 1996. 12: p. 3604-3612.

16. Porter, M.D., T.B. Bright, D.L. Allara, C.E.D. Chidsey, *Spontaneously organized molecular assemblies. 4. Structural characterization of n-alkyl thiol monolayers on gold by optical ellipsometry, infrared spectroscopy, and electrochemistry.* J. Am. Chem. Soc., 1987. 109(12): p. 3559-3568.

17. Snyder, R.G., S.L. Hsu, and S. Krimm, *Vibrational spectra in the C-H stretching region and the structure of the polymethylene chain.* Spectrochim. Acta, 1978. 34A: p. 395-406.

18. Snyder, R.G., H.L. Strauss, and C.A. Elliger, *C-H Stretching modes and the structure of n-alkyl chains. 1. Long, disordered chains.* J. Phys. Chem., 1982. 86: p. 5145-5150.

19. Schlenoff, J.B., M. Li, and H. Ly, *Stability and self-exchange in alkanethiol monolayers.* J. Am. Chem. Soc., 1995. 117(12528-12536).

20. Kakiuchi, T., M. Iida, N. Gon, D. Hobara, S.-I. Imabayashi, and K. Niki., *Miscibility of adsorbed 1-undecanethiol and 11-mercaptoundecanoic acid species in binary self-assembled monolayers on Au(111).* Langmuir, 2001. 17: p. 1599-1603.

21. Folkers, J.P., P.E. Laibinis, and G.M. Whitesides, *Self-assembled monolayers of alkanethiols on gold: comparisons of monolayers containing mixtures of short and long-chain constituents with CH_3 and CH_2OH terminal groups.* Langmuir, 1992. 8: p. 1330-1341.

22. Stranick, S.J., S.V. Atre, A.N. Parikh, M.C. Wood, D.L. Allara, N. Winograd and P.S. Weiss, *Nanometer-scale phase separation in mixed composition self-assembled monolayers.* Nanotechnol., 1996. 7: p. 438-442.

4 Insulator to metal transformation in nanometal inks

4.1 Introduction

Metal NP inks have potential applications especially as inter-connects and conductive electrodes in plastic electronics, apart from other numerous applications. In order to realize the application of these metal NP inks as conductive electrodes, the key aspect to be understood is its insulator to metal transformation characteristics. There have been plenty of research done on other traditional aspects of the metal NPs,[1-8] but with little focus on the T_p characteristics, recently.[9-13] Here, we show the behaviour of T_p with respect to ligand shell composition and structure, which lead us to some of the fundamental understanding of mechanism coalescence process in metal NPs.

4.1.1 Insulator-to-metal transformation temperature (T_p)

The temperature for the insulator–to–metal transformation can be defined as the mid-temperature for the percolative transition (T_p) at which a large increase in σ_{dc} occurs when plotted on the log σ_{dc}–linear T scale for temperature increased at some specified ramp rate, usually between 1–10ºC min^{-1}. σ_{dc} can be extracted from the current-voltage characteristics.[13]

Because this transformation is irreversible and kinetically controlled, the T_p depends on the temperature ramp rate and any isothermal hold, and is best represented on a temperature–time–transformation (TTT) diagram. Nevertheless, T_p measured at a suitable ramp rate provides a useful technological value and can be reproducibly measured for thin films (spin-cast or printed pads) using four-point-probe electrode patterns, and for long lines using two-point probes, and

therefore to quantify the behavior of the metal NP films. The T_p measured this way corresponds closely (within 10ºC) with the temperature for σ_{dc} to cross the 10^4 S cm^{-1} threshold for useful "metallic" conductivity which is within 0.02–0.1 of the bulk conductivity of most metals. For reference the bulk σ_{dc} = 6.3 (Ag), 6.0 (Cu), 4.5 (Au), 1.4 (Ni), 1.1 (Pd) and 0.95 (Pt) x 10^5 S cm^{-1}. As the transformation is kinetically limited, holding the metal NP film at a lower temperature but for a correspondingly long time can drive the transformation forward, as is well known particularly in the case of commercial Ag NP films: holding the film at 150ºC for 1 h to burn-off the dispersant at the ambient to produce a similar transformation as a few minutes at 250ºC.

The as deposited nano-Au films give $\sigma_{dc} \approx 10^{-7}$–$10^{-6}$ S cm^{-1}, and are in the insulator regime,[2, 14-17] due to the expected tunneling or charge-hopping[18] across the alkyl ligand shell between the clusters before annealing. Upon annealing to below T_p, σ_{dc} increases to 4x10^{-4} S cm^{-1}, and then more sharply over a small temperature range of 10ºC to reach nearly the bulk conductivity of the metal for Au NPs.

A recent development of polar solvent dispersible MHDA+MUL–Au NPs exhibits a T_p of 210ºC.[12, 13] However, this is considerably high as the back plane substrates for organic semiconductor devices are compatible with low temperatures (for e.g. < 170ºC for PET, polyethyleneterephthalate substrates). It is, therefore, decided to develop metal NP inks which have a T_p in the range of 140 – 170ºC. A new concept of metal NPs protected by sparse monolayer of ionic ligands that can achieve extremely high water- and polar-solvent-dispersibility has been developed (see chapter 3). These NPs are extremely soluble in polar solvents (> 200 mg mL^{-1} in ethylene glycol) and water (>

60 mg mL^{-1}) exhibits the lowest possible sintering temperature ever reported in the literature ($T_p \approx$ 145ºC).

From the evolution of plasmon band and its shape during annealing, the key stages of metal nanocore relaxation, ligand desorption and core–core coalescence have recently been enlightened.[12] Even though these steps are fundamental to the successful coalescence of the NP films, very few details are known. Therefore the work here presents the study of insulator to metal transformation of metal NPs by conductivity measurements, supported by detailed analysis of Fourier-transform infrared (FTIR) spectroscopy and optical transmission spectroscopy.

4.2 Experimental

4.2.1 Conductivity measurements of nanometal films

For these measurements, 200–400-nm-thick films were deposited by drop casting on to lithographically patterned four-in-line substrates as shown in Fig 4.1. Advantage of using 4-in-line substrates is the near absence of contact resistance and hence an accurate conductivity measurement. The samples were dropcast in the ambient at laminar flow hood and then transferred to glove box with moisture and oxygen down to 1 ppm. The annealing was done on a four probe station which has a heating stage; the heat ramp rate was set to 1^{o} C/min. Current was injected into the outer probes and voltage measured between the inner probes. d.c. electrical conductivity σ_{dc} was extracted from the Ohmic slope of current–voltage characteristics, measured using Keithley 4200 semiconductor parameter analyser. Average thickness of the films was estimated from a Tencor profilometer. To determine the thickness, scratch marks were made on the sample surface at different places after annealing. Thickness was measured from profilometer

by scanning across the scratch mark. Finally the σ_{dc} is given by the formula $\sigma = \frac{L}{W \times t \times R}$ where *L* is the distance between the two inner lines (50 or 250 μm) , *W* is the length of the lines (2.4 or 4.8 mm), *t* is the average film thickness and *R* is the resistance.

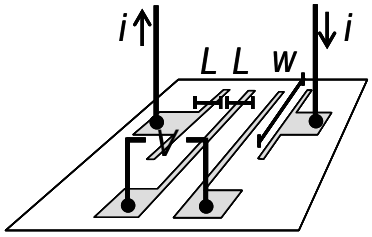

Figure 4.1 Schematic representation of 4-in-line probe substrate, used for conductivity measurements of metal NP films. Current is injected through the oute probes and the voltage measure through the inner probes.

4.2.2 Ligand shell transformation spectroscopy

Insulator to metal transformation and coalescence of metal NPs are studied using Fourier transform infrared (FTIR) spectroscopy by analyzing the transformation of key molecular vibrational bands present in the protective monolayers, with respect to temperature. FTIR spectra were taken on Nicolet 8700 FTIR spectrometer at a resolution of 4 cm^{-1} / 150 scans. Samples of Au NP films were deposited onto intrinsic silicon wafers at ambient conditions and annealed at different temperatures on calibrated hot plate, inside a N_2 glove box. The transformation characteristics were analysed after taking relative absorption cross-sections of key functional groups into consideration. The relative empirical integrated absorption cross-sections of various functional groups were determined from model compounds to be: $\nu_{as}COO^-$ (1.0), $\nu C{=}O_{acid}$ (0.9), $\delta C\text{-}OH_{alcohol}$ (0.35), and δCH_2 (0.42). See section 3.2.3 for detailed information on *relative integrated absorption*

cross-sections of various functional groups deduced from standard solid-state FTIR spectra of model compounds.

4.2.3 Optical transmission spectroscopy

Optical transmission spectra of sparse ionic monolayer protected Au NP film, MHA+MPL_Au, was collected by drop casting the ink on to a fused silica substrate, and dried at ambient. The spectra were recorded in a N_2-purged UV-Vis spectrometer. Initial film thickness was 55 nm; final thickness was 35 nm.

4.3 Results and discussion

Previous attempts to induce water dispersibility of metal NPs included the use of ω-carboxy-alkylthiols,[8, 19] , ionic-functionalized thiols,[19-22]and ethylene glycol thiols[22, 23] however the challenges still remain as very little known about the dispersibility and stability of these materials. Also the insulator to metal transformation temperature is higher for these materials, hence unsuitable for the plastic electronics applications. Recent report show that the stable dispersions at the required concentrations can be achieved in water and other polar solvents by using mixed ω-carboxy - and ω-hydroxy-alkylthiols (ω-mercaptohexadecanoic acid MHDA and ω-mercaptoundecanol MUL).[13] These materials, MHDA+MUL–Au NPs, exhibit a percolative insulator-to-metal transition $T_p \approx 210$ºC (from the dc electrical conductivity σ_{dc} diagram).[13] This is a practical measure of the coalescence temperature and or insulator to metal transformation.

4.3.1 Electrical conductivity, $\sigma_{d.c}$ of MHA+MPL–Au NP film

By employing sparse ionic monolayer assembly, the T_p of Au NPs have been reduced to 145ºC (Fig. 4.2). This is measured from the MHA+MPL–Au NP film, deposited on 4-in-line glass substrates, that shows the sharp transition at ≈ 145ºC. The as deposited film, at room temperature

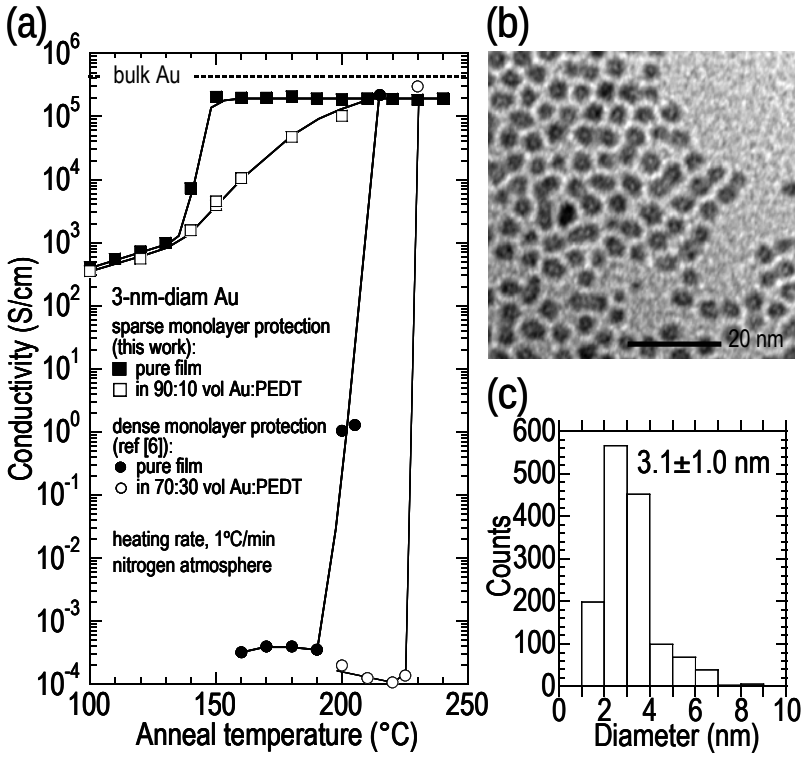

Figure 4.2. dc electrical conductivity $\sigma_{d.c.}$ diagram (a) DC conductivity of MHA+MPL–Au NP thin films measured as a function of heat-treatment temperature, compared to dense monolayer-protected MHDA+MUL–Au NP thin films. (b) TEM image. (c) Size distribution histogram.

shows the minimum $\sigma_{d.c.}$ ≈ 60 S cm^{-1}. This is relatively higher compared to the conventional dense monolayer protected Au NPs (for e.g. 10^{-5} S cm^{-1} for MHDA+MUL–Au NPs). High $\sigma_{d.c.}$ in as deposited MHA+MPL–Au NP film is due to the short electron tunneling gap between adjacent nanocores, shell thickness t = 6.7±0.75 Å, compared to t = 8.2±1.2 Å for MHDA+MUL–Au NPs.[13] When the film is annealed to 140 – 150ºC, $\sigma_{d.c.}$ increased rapidly to ≈ 2x10^5 S cm^{-1}. This is due to

desorption of ligand shells from the nanocore surface, which leads to the cold neck formation between the adjacent nanocores (Fig. 4.3). The cold sintering of nanocores leads to the formation of percolative conduction path, which essentially facilitate the conduction electron transport through relatively ordered Au atoms. T_p of MHA+MPL–Au–PEDT:PSSH composite films are upshifted by 10ºC for Au/PEDT ratio 90/10 v/v, which is due to the compatiblisation effect with the polymer matrix.[13] The maximum conductivity achieved in this metal NP films are nearly one-half of its corresponding bulk conductivity. This is due to the scattering of free conduction electrons, arising from the nanocrystaline morphology (see section 4.3.4 for details) and grain boundaries of the film, compared to electronic mean free path ≈ 40 – 50 nm in Au and Ag.

In comparison with MHDA+MUL–Au, the MHA+MPL–Au NP systems exhibit low T_p. The low *Tp* of these systems is due to the sparse ionic monolayer assembly, which is about 25% of the monolayer density on conventional monolayer protected Au NP systems. By employing the sparse ionic ligand shell, the inter molecular ionic interaction, hydrogen bonding, and vanderwalls forces have been greatly reduced to achieve the lower T_p value for MHA+MPL–Au NP inks. Further details on how the T_p varies with respect to above aspects are presented in the following sections.

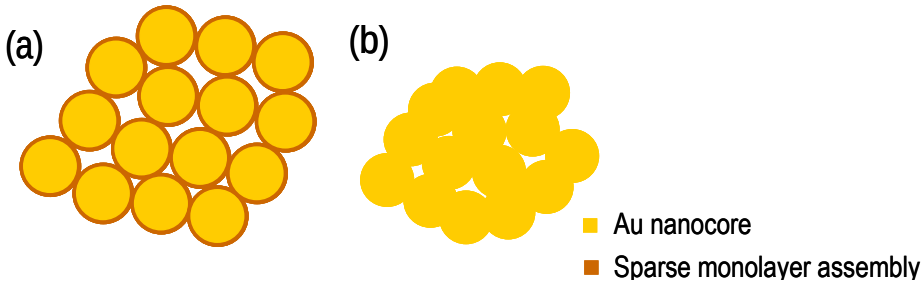

Figure 4.3 Schematic representation of coalescence of nanocores: (a) Un-coalesced Au matrix: as deposited film Au NPs protected by sparse ionic monolayer assembly (b) Coalesced Au matrix: formation of percolative conduction path after desorption of ligand shells from the nanocore surface.

4.3.2 Ligand shell transformation spectra of nanometal inks

Different monolayer-protected Au NP systems with similar range core diameters (2.4–3.8 nm) were studied on the course of development of low T_p nanometal ink. Table 4.1 summarizes the T_p, ultimate film conductivity, and other properties obtained for these materials. Contrary to the behavior of alkylthiol- protected Au NPs,[10] reducing the ω-carboxyl ligand chain length does not reduce T_p. For example, T_p for ω-mercaptohexanoic acid (MHA)-protected Au NP is 220ºC, similar to long-chain MUA_{acid} protection,[13] and considerably higher than alkylthiol protection of similar lengths (130 and 180ºC respectively for butanethiol (BT) to decanethiol (DT), see Table 4.1 entries 1a, 1b, 1d, 2a and 2b). This turns out to be due to extensive stabilisation of the ligand shell by hydrogen bonding and inter-molecular ionic interaction. The MHA–Au NPs were produced and purified in mixed acid+salt form, which is confirmed from integrated FTIR intensities of the $\nu_{as}COO^-$ and $\nu C{=}O_{acid}$ bands at 1567 cm^{-1} and 1700 cm^{-1} respectively, corrected by relative empirical absorption cross-sections, are in agreement with XPS measurements (70±15 mol% salt form).

On the quantitification of FTIR spectra of these ligand shells, the effects of metal nanocores on their vibrational absorption cross-sections have been considered. The optical modeling study shows that the absorption cross-sections are uniformly enhanced across the vibrational spectrum by a significant factor depending on shell thickness.[24] This effect is practically constant across the entire vibration spectrum.

FTIR spectra shows the onset of ligand elimination at 190ºC (Figs. 4.4b and 4.5b) and reaches >80% completion by 200ºC. Experimentally, the intensity evolutions of all five key functional-group

Table 4.1 Summaries of Au NP inks from this work

S/No	Shell notation	Protection thiol (feed mol ratio, if relevant)	T_p (ºC)**[a]**	Actual ligand shell composition (mol ratio)**[b]**	Remarks**[c]**
1a	MHA_{salt}	$HOOC(CH_2)_5SH$	220	COOH(0.3), COO^-(0.7)	d = 28 ± 09 t = 7.8± 0.75
1b	MHA_{salt}	$HOOC(CH_2)_5SH$	210		d = 125 ± 22
1c	MPA_{salt}	$HOOC(CH_2)_2SH$	210		
1d	MUA_{acid}	$HOOC(CH_2)_{10}SH$	210	COOH (1.0)	d = 33 ± 10 [d]
1e	MHA_{acid}	$HOOC(CH_2)_5SH$	170	COOH (1.0)	[d]
1f	MPA_{acid}	$HOOC(CH_2)_2SH$	125	COOH (1.0)	[d]
2a	BT	$CH_3(CH_2)_3SH$	130		d = 38 ± 12
2b	DT	$CH_3(CH_2)_9SH$	180		d = 25 ± 7 t = 7.3 ± 0.9
3a	MHA+BT	$HOOC(CH_2)_5SH$: $CH_3(CH_2)_3SH$ 1 : 10	200	COOH(0.04), COO^-(0.04), BT(0.92)	d = 24 ± 8 t = 9.3 ± 1.4
3b	MHA+BT	$HOOC(CH_2)_5SH$: $CH_3(CH_2)_3SH$ 1 : 20	190		
4	MHA+MPL	$HOOC(CH_2)_5SH$: $HO(CH_2)_3SH$ 1 : 10	145	COOH(0.31), COO^-(0.52), OH(0.17)	d = 32 ± 10 t = 6.7 ± 0.75
5	MHA+MPA	$HOOC(CH_2)_5SH$: $HOOC(CH_2)_2SH$ 1 : 1	160		
6a	MHA+MBL	$HOOC(CH_2)_5SH$: $HO(CH_2)_4SH$ 1 : 1	190		
6b	MHA+MBL	$HOOC(CH_2)_5SH$: $HO(CH_2)_4SH$ 1 : 10	180	COOH(0.66), COO^-(0.03), OH(0.31)	d = 27 ± 07

[a] T_p is the percolation temperature taken to be the mid-point of the morphological insulator-to-metal transition measured in dc electrical conductivity plotted on the log scale. The average heating rate was 1ºC min^{-1} on a hotplate calibrated with melting-point standards, in a N_2 glovebox. Films were 200–400-nm thick and deposited on four-in-line-electrode patterns fabricated on glass substrates. Accuracy and repeatability, ±10ºC.

[b] Composition mole ratio of the ligand shell obtained from FTIR terminal group analysis: COOH = acid and COO^- = salt forms of □-carboxyl groups, and OH = □-hydroxyl groups; expressed as mol ratio of the total SAM.

[c] d is the average NP Au-core diameter in Å, measured by TEM; t is the average shell thickness in Å, taken to be half of the inter-particle spacing for contact pairs.

[d] Maximum conductivity of this film is less than $5x10^4$ S cm^{-1}. For other films, the maximum conductivity is more than $2x10^5$ S cm^{-1}.

bands ($\nu CH_2+\nu CH_3$, $\nu C=O$, νCOO^-, $\delta S–CH_2$)[25] track each other remarkably well. This indicates a piecewise elimination of the ligands either by desorption or fragmentation. Since carboxylate salts have insignificant vapor pressures, fragmentation must constitute an important pathway in the MHA_{salt}–Au NPs. The constancy of the $\delta S–CH_2$ band positions (± 2 cm^{-1}) rules out formation of significant quantities of trapped disulfides, which is expected to have vibrational shifts of $\delta S–CH_2$ of a few wavenumbers. The spectra indicate residual MHA salt derivatives (with downshifted νCOO^-) even at 220ºC. Retention of residual organic ligands is a universal feature of all the Au NP systems, probably as a result of occlusion within the coalescing Au matrix.

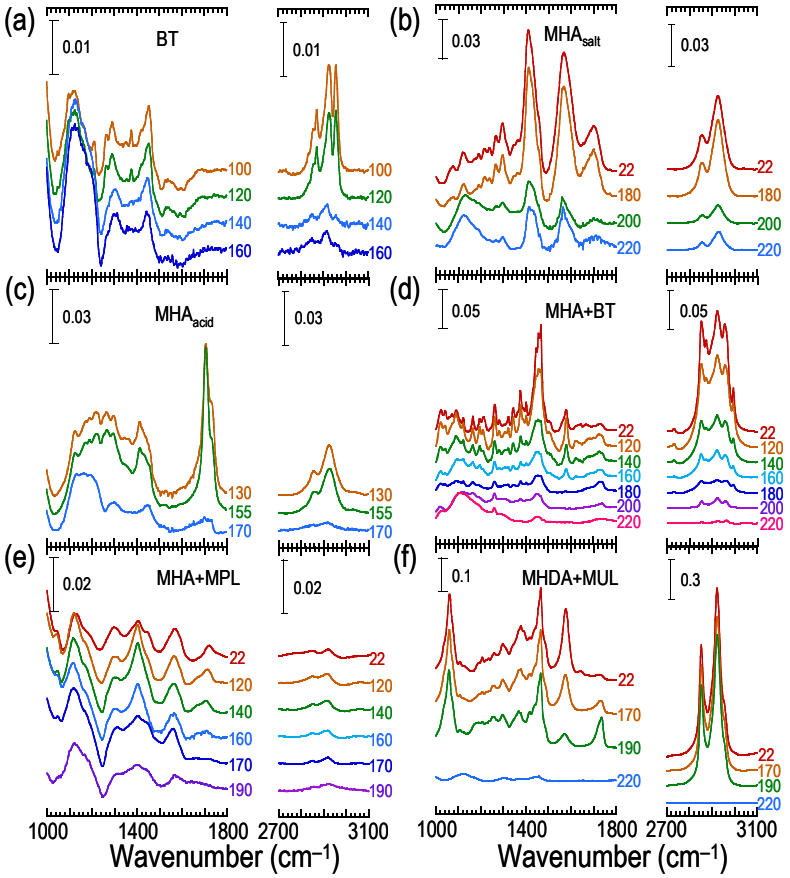

Figure 4.4 Molecular transformation: Molecular transformation of the Au NP ligand shell measured by FTIR on thin films deposited on intrinsic Si wafer as a function of heat-treatment temperature. Samples were annealed at the indicated temperatures for 10 min in the glovebox (pO_2, H_2O < 1 ppm) before transfer to the spectrometer. Descriptions of the ligand shells are given in Table 4.1

COOH-terminated Au NPs (i.e., MHA_{acid}–Au) was prepared by acidification of water soluble MHA_{salt}–Au NPs with concentrated HCl. The T_p of this material is ≈ 170^{0}C (Table 4.1, entry 1e) which is 50ºC lower than that of MHA_{salt}–Au NPs. FTIR shows (Fig. 4.4c and 4.5c) the elimination onset at 155ºC. In both MHA_{salt}– and MHA_{acid}–Au NPs, the alkyl chain conformations are disordered (ν_sCH_2 2854–2858 and $\nu_{as}CH_2$ 2924 cm^{-1}; compared with all-*trans* values of 2846–2850 and 2915–2920 cm^{-1}, and liquid values of 2856 and 2928 cm^{-1} respectively).[26-30] Hence the lower T_p of MHA_{acid}–Au is a tail group effect due to a weaker intermolecular interaction compared to the ionized tail group, rather than differences in chain conformation.

To investigate whether T_p can further be decreased by disrupting the hydrogen bonding, we prepared Au NPs protected by a mixture of MHA and hydrophobic BT ligands in the molar ratio of 1:10–1:20 (Table 4.1, entries 3a and 3b). These NPs are however not dispersible in H_2O or MeOH but in toluene. While pure BT–Au NPs show T_p ≈ 130ºC, MHA+BT–Au NPs surprisingly show T_p ≈ 190–200ºC even at large MHA dilutions. From FTIR, the ligand ratio [MHA]/[BT] incorporated into the ligand shell was found to be 0.085±0.015 (with 50 mol% of MHA in salt form) for a feed ratio of 0.10. During annealing, BT desorbs first over ≈ 120–160ºC (similar to pure BT–Au NPs), followed by overlapping loss of MHA_{acid} and MHA_{salt} over 140–200ºC (Fig. 4.4d and 4.5d). The T_p is pinned to the near complete loss of MHA and so 10 mol% in the shell can remarkably elevate T_p by 60–70ºC. This suggests a preferred ionic and/or hydrogen bonding between MHA on neighboring NPs that hold apart the Au cores and suppress coalescence, which could be useful for some applications. We then investigated the MHDA+MUL–Au NP systems which exhibits the T_p ≈ 210ºC (Fig. 4.2). This is consistent with the FTIR spectra (Fig. 4.4f & 4.5f) which show the onset of

elimination of ligand shells at 190ºC and near completion of elimination at 210ºC. The higher T_p value of these materials syetems, similar to MHA_{salt}–Au NPs, is due to extensive stablisation of ligand shells due to the intermolecular ionic interaction, hydrogen bonding and van der Waals interactions. Similar behaviour is noticed for MUA_{acid}–Au systems, $T_p \approx 210$ºC (Table 4.1, entry 1d). In the limit of MHA_{salt}–, MPA_{salt}–Au NPs, the insulator to metal transformation of these films lies on the same regime, T_p = 210ºC (Table 4.1 entry 1a & 1c). However films of these NPs after acidification exhibit very different T_p, 170ºC for MHA_{acid}– and 125ºC for MPA_{acid}– Au NPs (Table 4.1 entry 1e & 1f). It is understood that the intermolecular ionic interaction is predominant, compared to hydrogen bonding and van der Waals interactions

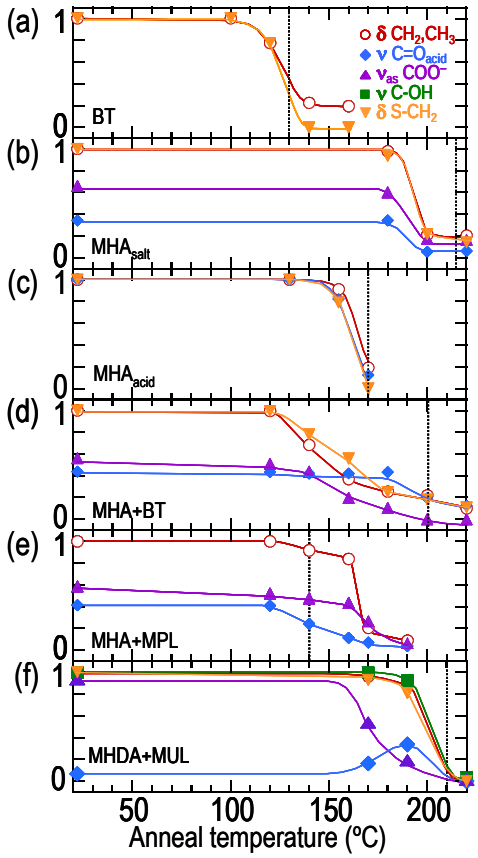

Figure 4.5 Temperature evolution of key FTIR band intensities: All trends were normalized to a starting value of 1, except for $\nu_{as}CO_2^-$ and $\nu C{=}O_{acid}$ which were normalized to a total of 1 using empirically determined absorption cross-sections.

We then investigated Au NPs protected by a mixture of MHA and hydrophilic 3-mercaptopropan-1-ol (MPL) ligands. Interestingly, sparse monolayer protected MHA+MPL–Au NPs exhibit $T_p \approx 145$ºC (Table 4.1, entry 4), which is the lowest temperature achieved to date for water-dispersible Au NPs. FTIR spectra (Fig. 4.4e & 4.5e) show the onset of elimination of ligands at 130ºC, but the complete elimination of ligands close to 160ºC. This effect is similar to the MHA_{salt}–Au NP films where the ionic (carboxylate salt) groups have insignificant vapour pressures, hence fragmentation must be the decomposition path way. Traces of signatures of key vibrational bands are still seen in the FTIR spectra, which are due to the universal feature of these NP metal films, may be due to occlusion.

To show that the sparse monolayer principle is general and T_p varies with its degree of sparcity of the monolayer, we investigated a mixture of MHA and the short-chain 3-mercaptopropionic acid(MPA) in the 1:1 feed ratio. MPA is also miscible in water in all proportions. The T_p is slightly higher ≈ 160ºC, due to the higher MHA in the shell (Table 4.1 entry 5). For a mixture of MHA and ω-mercaptobutanol (MBL), in which MBL is less soluble (60 mg mL^{-1}) than MPL, but more than MHA, T_p increases to 170–190ºC (Table 4.1 entry 6a and 6b). FTIR gave a shell [MHA]/[MBL] = 2.2±0.4, which though still considerably depleted in MBL than the feed [MHA]/[MBL] of 0.1, is less so than with MPL as co-ligand.

4.3.3 Insulator to metal transformation in sparse monolayer protected Ag NP inks

The ionic sparse monolayer concept is general for metal NPs as the same has also been demonstrated with Ag NPs (Fig. 4.6). MHA+MPL–Ag NPs were prepared by the reduction of

$AgNO_3$ solution in water-methanol 1:1 vol/vol, in the presence of desired mixture of thiols. Ag/S thiol ratio was kept at 2. MHA+MPL–Ag NPs of 14±5 nm have been obtained. The insulator to metal transformation temperature for these Ag NP film was studied by the conductivity measurements by depositing the solution on the 4-in-line substrates. Interestingly, MHA+MPL–Ag NPs exhibit T_p (≈155ºC) in the similar region as MHA+MPL–Au NP inks (Fig. 4.6).

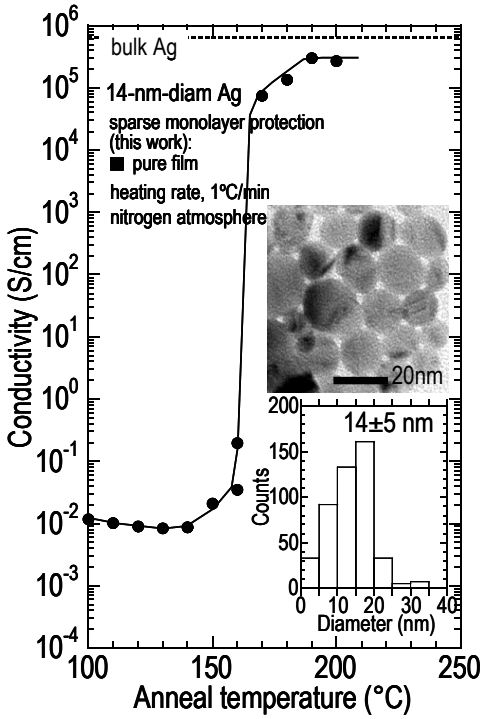

Figure 4.6 Sparse monolayer-protected Ag NPs. DC conductivity of MHA+MPL–Ag NP thin films measured as a function of heat-treatment temperature in a four-probe configuration. Insets: TEM image and size distribution histogram.

4.3.4 Optical transition spectra of MHA+MPL–Au NP inks

In thin films, plasmon coupling becomes important and can be used to probe film quality and the extent of insulator-to-metal transformation. As-deposited metal NP films that are still protected by a ligand shell show a plasmon band that is only slightly red-shifted from the dilute solution position.

In thin films, deposited at room temperature, the λ_{max} will be at ≈520 to 540 nm[12, 13] and the same will red–shifts and broadens when the inter–particle gap is reduced. The sparse monolayer

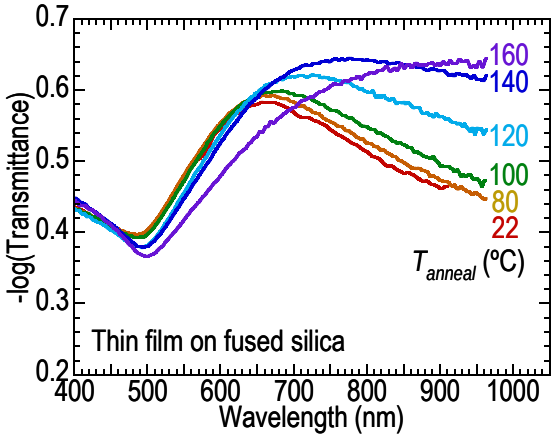

Figure4.7 Optical transmission spectra of MHA+MPL sparse-monolayer protected nano-Au film deposited on fused silica as function of heat treatment

protected MHA+MPL–Au NP film shows that the λ_{max} located at 656 nm (fig. 4.6); however the solution phase spectra show that the same nanometal inks λ_{max} located at 525 nm. In the solution phase, MHA+MPL–Au NPs dispersed well in the medium and hence the coupling of plasmon oscillation is suppressed. However in thin–films, the sparse–monolayers lying on the surface of NPs that reduces the inter–particle gap to a greater extent which leads to the coupling of dipole oscillations between the particles that results in red–shit and broadening of plasmon band. Optical modeling shows that this band red shifts with increased coupling between Au NPs.[12] The as-deposited film is already golden in color (however this does not necessarily imply core-core coalescence)[12] and insolubilized, with $\sigma_{dc} \approx 60$ S cm^{-1} due to short tunneling gap ($2t$ = 1.3 nm) between the NPs. This effect is consistent with the optical transition spectra of the as deposited MHA+MPL–Au films that show the corresponding plasmon band position λ_{max} at 656 nm. Reduced

inter particle gap in thin film leads to the high conductivity due to the tunneling of electrons and the large red-shift of plasmon band due to the increased coupling between adjacent cores. When annealed to $T_p \approx 140$ºC, the plasmon band red shifts and broadens while an underlying Drude tail emerges which marks the onset of coalescence to a final "nanograined" bulk continuous film (Fig. 4.7). The effect is self consistent with FTIR analysis that shows the near complete elimination of ligand shells from nanocore surface at T_p, and dc electrical conductivity $\sigma_{d.c.}$ measurements that shows the rapid increase in the conductivity of film to 2×10^5 S cm^{-1} at T_p. The final film is not bulk, but nanostructured or near bulk–like, as evidenced by vestiges of plasmon resonance even at 160ºC.

4.4 Summary

In summary, we have understood the insulator to metal transformation in sparse-ionic monolayer protected water and polar solvent dispersible Au NPs can be coalesced to high conductive state at as low as 145°C. We have also studied from the detailed FTIR analysis that the insulator to metal transformation can be controlled by ligand shell structure, ligand chain length and ligand inter-molecular stabilization effect. This enables us to conduct the fundamental study on coalescence of metal NPs, with respect to thermodynamic size effect and surface melting mechanisms (see chapter 5).

4.5 References:

1. Brust, M. and C.J. Kiely, *Some recent advances in nanostructure preparation from gold and silver particles: a short topical review.* Colloids and Surf. A, 2002. 202 p. 175–186.
2. Brust, M., D. Bethell, C.J. Kiely, and D.J. Schiffrin,, *Self-assembled gold nanoparticle thin films with nonmetallic optical and electronic properties.* Langmuir, 1998. 14: p. 5425-5429.
3. Brust, M., M. Walker, D. Bethell, D.J. Schiffrin, and R. Whyman, *Synthesis of thiol-derivatised gold nanoparticles in a two-phase Liquid–Liquid system.* J. Chem. Soc., Chem. Commun., 1994: p. 801 - 802
4. Daniel, M. and D. Astruc, *Gold nanoparticles: assembly, supramolecular chemistry, quantum-size-related properties, and applications toward biology, catalysis, and nanotechnology.* Chem. Rev. , 2004. 104: p. 293-346.
5. Hostetler, M.J., J.J. Stokes, and R.W. Murray, *Infrared spectroscopy of three-dimensional self-assembled monolayers: n-alkanethiolate monolayers on Au cluster compounds.* Langmuir, 1996. 12: p. 3604-3612.
6. Hostetler, M.J., J.E. Wingate, C.J. Zhong, J.E. Harris, R.W. Vachet, M.R. Clark, J.D. Londono, S.J. Green, J.J. Stokes, G.D. Wignall, G.L. Glish, M.D. Porter, N.D. Evans, and R.W. Murray, *Alkanethiolate gold cluster molecules with core diameters from 1.5 to 5.2 nm: Core and monolayer properties as a function of core size.* Langmuir, 1998. 14: p. 17-30.
7. Sardar, R., A.M. Funston, P. Mulvaney and R.W. Murray, *Gold nanoparticles: past, present, and future.* Langmuir, 2009. 25: p. 13840–13851.
8. Weisbecker, C.S., M.V. Merritt, and G.M. Whitesides, *Molecular self-assembly of aliphatic thiols on gold colloids.* Langmuir, 1996. 12: p. 3763-3772.
9. Greer, J.R. and R.A. Street, *Mechanical characterisation of solution-derived nanoparticle silver ink thin films.* J. Appl. Phys., 2007. 101: p. 103529(1-5).
10. Huang, D., F. Liao, S. Molesa, D. Redinger, and V. Subramanian, *Plastic-compatible low resistance printable gold nanoparticle conductors for flexible electronics.* J. Electrochem. Soc., 2003. 150: p. G412-G417.
11. Perelaer, J., A.W. M. de Laat, C.E. Hendriks and U.S. Schubert, *Inkjet-printed silver tracks: low temperature curing and thermal stability investigation.* J. Mater. Chem., 2008. 18: p. 3209-3215.
12. Sivaramakrishnan, S., B.T. Anto, and P.K.H. Ho, *Optical modeling of the plasmon band of monolayer-protected nanometal clusters in pure and in polymer matrix thin films as a function of heat treatment.* Appl. Phys. Lett., 2009. 94: p. 091909.

13. Sivaramakrishnan, S., Chia P.J., Yeo Y.C., Chua L.L., and Ho P.K-H, *Controlled insulator-to-metal transformation in printable polymer composites with nanometal clusters.* Nat. Mater., 2007. 6: p. 149-155.
14. Cliffel, D.E., F.P. Zamborini, S.M. Gross, and R.W. Murray, *Mercaptoammonium-monolayer-protected, water-soluble gold, silver, and palladium clusters.* Langmuir, 2000. 16: p. 9699-9702.
15. Musick, M.D., C.D. Keating, M.H. Keefe, and M.J. Natan *Stepwise construction of conductive Au colloid multilayers from solution.* Chem. Mater., 1997. 9: p. 1499-1501.
16. Musick, M.D., C.D. Keating, L.A Lyon, S.L. Botsko, D.J. Peña, W.D. Holliway, T.M. McEvoy, J.N. Richardson, and M.J. Natan, *Metal films prepared by stepwise assembly. 2. Construction and characterization of colloidal Au and Ag multilayers.* Chem. Mater., 2000. 12: p. 2869-2881.
17. Terrill, R.H., T.A. Postlethwaite, C.-H. Chen, C.-D. Poon, A. Tarzis, A. Chen, J.E. Hutchison, M.R. Clark, G. Wignall, J.D. Londono, R. Superfine, M. Falvo, C.S. Johnson, Jr., E.T. Samulski, and R.W. Murray, *Monolayers in three dimensions: NMR, SAXS, thermal, and electron hopping studies of alkanethiold stabilised gold clusters.* J. Am. Chem. Soc., 1995. 117: p. 12537-12548.
18. Abeles, B., Sheng P., Coutts M. D., Arie Y., *Structural and electrical properties of granular metal films.* Adv. Phys., 1975. 24: p. 407-461.
19. Chen, S. and K. Kimura, *Synthesis and characterization of carboxylate-modified gold nanoparticle powders dispersible in water.* Langmuir, 1999. 15: p. 1075-1082.
20. Kim, K.-S., D. Demberelnyamba, and H. Lee, *Size-selective synthesis of gold and platinum nanoparticlesusing novel thiol-functionalised ionic liquids.* Langmuir, 2004. 20: p. 556-560.
21. Templeton, A.C., S. Chen, S.M. Gross, and R.W. Murray, *Water-soluble, isolable gold clusters protected by tiopronin and coenzyme A monolayers.* Langmuir, 1999. 15: p. 66-76.
22. Yonezawa, T., S. Onoue, and N. Kimizuka, *Preparation of highly positively charged silver nanoballs and their stability.* Langmuir, 2000. 16: p. 5218-5220.
23. Zubarev, E.R., J. Xu, A. Sayyad, and J.D. Gibson, *Amphiphilic gold nanoparticles with v-shaped arms.* J. Am. Chem. Soc., 2006. 128: p. 4958-4959.
24. Sivaramakrishnan, S., B.T. Anto, and P.K.H. Ho, *Unpublished results*. 2009.
25. Colthup, N.B., L.H. Daly, and S.E. Wiberley, *Introduction to infrared and Raman spectroscopy*. 1990, San Diego: Academic Press, Inc.
26. Bertilsson, L. and B. Liedberg, *Infrared study of thiol monolayer assemblies on gold: preparation, characterisation, and functionalisation of mixed monolayers.* Langmuir, 1993. 9: p. 141-149.
27. Miller, F.A. and C.H. Wilkins, *Infrared spectra and characteristic frequencies of inorganic ions.* Anal. Chem., 1952. 24: p. 1253–1294.

28. Porter, M.D., T.B. Bright, D.L. Allara, C.E.D. Chidsey, *Spontaneously organized molecular assemblies. 4. Structural characterization of n-alkyl thiol monolayers on gold by optical ellipsometry, infrared spectroscopy, and electrochemistry.* J. Am. Chem. Soc., 1987. 109(12): p. 3559-3568.

29. Snyder, R.G., S.L. Hsu, and S. Krimm, *Vibrational spectra in the C-H stretching region and the structure of the polymethylene chain.* Spectrochim. Acta, 1978. 34A: p. 395-406.

30. Snyder, R.G., H.L. Strauss, and C.A. Elliger, *C-H Stretching modes and the structure of n-alkyl chains. 1. Long, disordered chains.* J. Phys. Chem., 1982. 86: p. 5145-5150.

5 Coalescence of monolayer protected metal NPs

5.1 Introduction

Metal NPs are known for the melting point depression compared to its bulk material. This is due to the large surface area to volume ratio compared to its bulk metal that essentially alters their thermal behaviours, which is commonly known as thermodynamic size effect.[1-7] Metal NPs have larger fraction of its total atoms on the surface (see section 2.3.1); however this scenario tells that each atom of metal NP has less number of neighbour atoms compared to that of bulk. This leads to reduced average cohesive energy per atom, which is proportional to the melting point of any material.[8, 9] Hence the metal NPs have depressed melting points. This melting point depression due to thermodynamic size effect on various metals has experimentally proven by many researchers across decades. For the same reason, metal NP surfaces can melt at low temperatures. Surface melting temperature of metal NPs decreases with increase in radius of curvature of NPs.[10, 11] Number of adjacent atoms increases with the increase in radius of curvature of NPs, which results in increase of average cohesive energy per atom, hence the surface melting temperature.

However these mechanisms are true for the melting behaviour of metal NPs, but the insulator to metal transformation or coalescence temperature of monolayer protected metal NPs doesn't comply with this. Thermodynamic size effects are negligible for NPs larger than 50-nm-diameter (T_m lies within 20ºC of bulk melting temperature T_m^o), but becomes significant for d < 5–20 nm, depending on the metal. For the minimum useful core diameter d = 3.2 nm, $T_m \approx$ 675ºC for Au, and 280ºC for Ag [1, 2, 12] which are much higher than what can be tolerated in a number of

technologies. Therefore it is clear that while both the depression of the nanocore melting and the surface melting are manifestations of the thermodynamic size effect of the NPs; they do not actually play a role in nano-Au coalescence and certainly not in the present commercially available nano-Ag inks with $d \approx 50$ nm. Theory of thermodynamic size effect is well understood and reviewed in chapter 2 (section 2.5). Contradictorily, thermodynamic size effect has been widely and frequently asserted in the literature for the mechanism of coalescence of monolayer protected metal NP films.[13-21] In this chapter we explain with experimental evidence on the mechanism of coalescence of monolayer protected metal NPs.

5.2 Experimental

5.2.1 Differential scanning calorimetry

Different monolayer protected Au NP samples, ≈ 5 mg, were dried on aluminium pans at 50ºC on a hotplate at ambient. The thermograms were collected at a ramp rate of 20ºC min^{-1} under nitrogen atmosphere.

5.2.2 Conductivity measurements of nanometal films

$\sigma_{d.c.}$ of metal NPs of different core diameters and similar protective ligand shells are measured by depositing 200–400-nm-thick film on to 4-in-line glass substrates. See experimental 4.2.1 for further details.

5.3 Results and discussion

5.3.1 Insulator-to-metal transformation, T_p: Lack of dependence on metal core size

The bottleneck step in the insulator–to–metal transformation during thermal annealing of Au NPs is the elimination of the ligand shell, and not melting of the metal nanocore, or even of the surface melting of the core. It is clearly understood that the depressed melting temperature (T_m > 500ºC for a core diameter $d \approx 3$ nm) is not low enough to account for the transformation in Au NPs. This is also demonstrated by the near invariance of T_p with NP core size (Fig. 5.1). 12.5 and 2.8 nm core–diameter MHA_{salt}–Au NPs were prepared by varying Au/S ratio 6 and 2 respectively. Both nanometal inks were soluble in water, and the conductivity of these inks was measured by depositing the film onto 4-in-line glass substrates. Interestingly, both the films exhibit similar $Tp \approx$ 210 – 220ºC. Practically, the depressed melting point of d = 12.5 nm Au NP is T_m > 1000ºC. [1, 2, 12] However we have annealed the film only to 210ºC for few minutes to achieve the insulator to metal transformation due to coalescence of metal nanocores to give $\sigma_{d.c.} > 10^5$ Scm^{-1}. This behaviour is similar to the MHA_{salt}–Au NPs of d = 2.8 nm. From the FTIR analysis (fig. 4.4b and 4.5b), we have understood that the insulator to metal transformation temperature is close to the near completion of elimination of ligand shells for MHA_{salt}– and other Au NPs. This is self consistent with our current observation of invariance of T_p with respect to core diameter. MHA+MPL–Ag NPs of core diameter 14 nm exhibit the T_p at ≈ 155ºC (fig. 4.6), which is very much less than the depressed melting of Ag NPs of similar core diameter (T_m > 450ºC for d = 14 nm). It is well understood from these experiments that the coalescence temperature T_p is not controlled by both T_m and surface melting mechanisms.

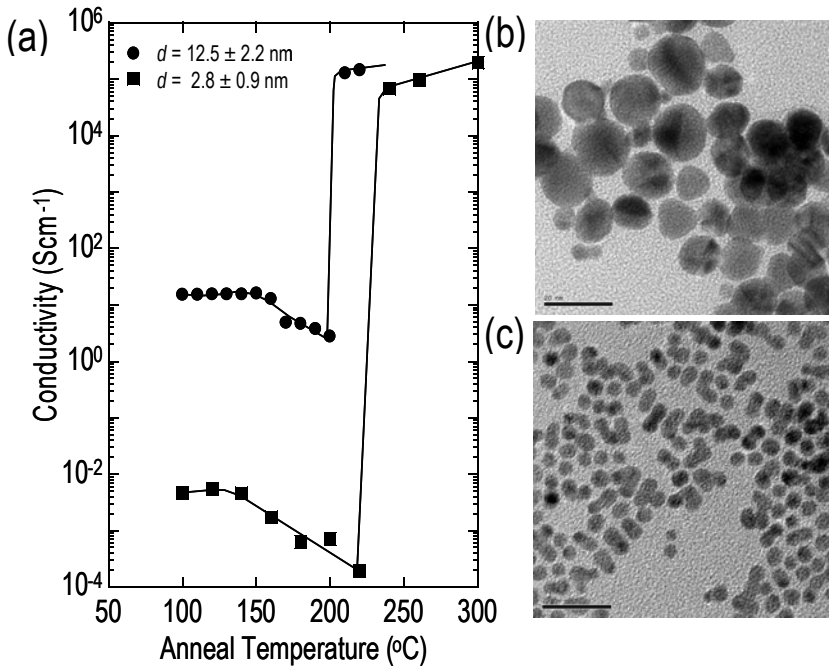

Figure 5.1 Invariance of T_p with respect to core diameter: (a) DC conductivity of MHA_{salt}–Au NP thin films of different core diameters, measured as a function of heat-treatment temperature. (b) and (c) Transmission electron micrograph of MHA_{salt} – Au NPs of diameter 12.5 and 2.8 nm, respectively.

5.3.2 T_p: Dependence on the ligand shell structure

However the T_p depends strongly on the nature of the dispersant (Table 4.1) for similar core diameters (d = 2.4–3.8 nm, standard deviation ±30%). Molecular dispersants (i.e., self-assembled monolayers) can potentially give much lower T_p than polymeric dispersants. The key processes and extent of elimination of the ligand shell can be measured by FTIR as a function of annealing (Figs. 4.4 and 4.5). FTIR shows the $\delta S–CH_2$ bands (*ca*. at 1215 and 1265 cm^{-1}) remain unchanged in frequencies while their intensities track the νCH_2 intensity throughout the transformation. This rules out the early occurrence of a separate Au–S bond scission step to give trapped disulfides and/or partial fragmentation intermediates within the shell that desorbs at elevated temperatures. Instead FTIR together with T_p data, obtained from the conductivity

measurements, indicates that Au core coalescence occurs shortly after the simultaneous dissociation of Au–S and elimination of the shell. This picture is supported by DSC (fig. 5.2), where the thermogram shows that exotherm are self–consistent with respective T_p data of nanometal inks. The calculated heat flow of 0.4–0.5 J m^{-2} of NP surface area (taking into account of the distribution histogram) corresponds to 70–85 kJ mol^{-1} normalized to thiol ligands (assuming projected cross-section area of thiol 28 $Å^2$), which considerably exceeds the enthalpy of the ligand shell dissociation reactions. For example, $2Au_{met}–SR \rightarrow 2Au_{met}$ + RSSR[22-24] is only 16 kJ mol^{-1} exothermic (bond strengths: $Au_{met}–SR$, 126 kJ mol^{-1};[25] RS–SR, 285 kJ mol^{-1}[26]). Therefore the enthalpy of transformation is dominated by the enthalpy of coalescence which is of the same order of magnitude as the surface energy of Au (1.5 J m^{-2}) [1, 2, 27, 28] The close coincidence of the exotherm with the FTIR transformation (fig. 4.4 and 4.5) shows that coalescence occurs with shell elimination.

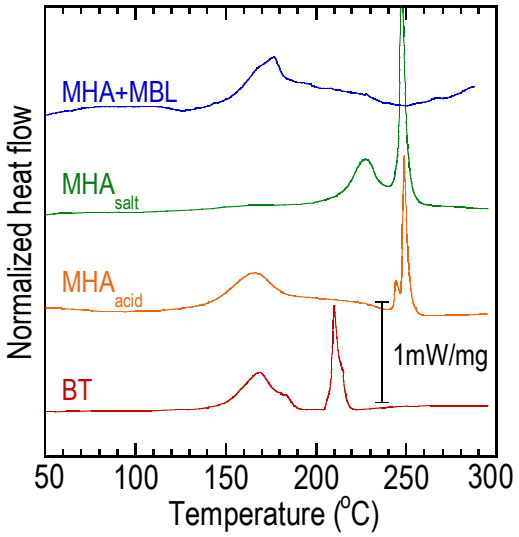

Figure 5.2 Thermogram of nanometal inks: Differential scanning calorimetry of Au NPs, conditions: 3–5 mg, in N_2 at 20°C min^{-1}.

5.3.3 T_p: Ligand chain-length effect.

For monolayer ligand-shell-protected, organic-solvent dispersible Au NPs, T_p increases with alkyl-chain length[29] in unfilled NP films for alkylthiol-protected Au NPs: from 130ºC for butanethiol to 180ºC for decanethiol protection. These simple alkyl thiol ligands have no functional groups such as hydroxyl or carboxyl moieties, which are free from the inter-molecular ionic & hydrogen bonding effects. Hence the T_p of these simple alkylthiol protected metal NPs are controlled by Au-S bond scission together with van der Waals interaction between the molecular ligands.

For commercially-available Ag NPs, T_p is typically considerably higher, 240–300ºC. With appropriate engineering to give a sparse protection monolayer, this can remarkably be lowered to 140ºC. The ultimate conductivity attainable is within a factor of 2 of the bulk conductivity, due to the final nanocrystalline morphology of the film which scatters the conduction electrons much smaller than the 40–50-nm mean free path[30] of the conduction electrons in bulk single crystals, but this is not an issue with most of the applications.

5.3.4 T_p: Ligand intermolecular stabilization effect.

For ω–carboxyl ligands (which has a carboxyl group at the tail end of the alkyl chain) decreasing the chain length does not reduce T_p. For example, T_p for MHA protected Au NP is 220ºC, similar to the longer chain MHDA,[31, 32] and considerably higher than the corresponding alkylthiols. This is due to extensive stabilization of the ligand shell by hydrogen–bonding and ionic interaction (vide infra).

The T_p increases by *ca*. 100ºC across the series: butanethiol (BT) < mixed mercaptohexanoic acid and mercaptopropanol (MHA+MPL) < acid form of mercaptohexanoic acid (MHA_{acid}) < mixed

mercaptohexanoic acid and butanethiol (MHA+BT) < salt form of mercaptohexanoic acid (MHA_{salt}), along which the shell thickness varies very little (BT: 8.6 Å, MHA: 7.8 Å) for the similar Au core sizes (d = 2.4–3.8 nm).

FTIR shows the onset of the elimination of the BT ligand to be 110ºC and to reach completion by about 140ºC from the loss of the CH_2 stretching (ν CH_2) and bending (δ CH_2) vibration intensities and also the loss of the S–CH_2 bending (δ S–CH_2) intensity at the head-group. The T_p occurs at ca. 130ºC near the completion of the elimination. For the ω-functionalized alkyl thiols, the elimination temperature can be greatly increased by 100 ºC due to intermolecular stabilization of the ligand shell by hydrogen bonding and/or ionic interaction. The T_p are found to shift correspondingly to near the completion of elimination of the ligand shell.

For MHA-salt ligand elimination occurs at an onset of 190ºC and reaches >80% completion by 200ºC. The intensity evolutions of all five bands νCH_2+νCH_3, νC=O, νCOO^-, δS–CH_2 track each other remarkably well (fig. 4.4 and 4.5), which indicates a piecewise elimination of each ligand molecule either by desorption or fragmentation. DSC shows an exotherm onset at 210ºC and peak at 225ºC (Fig. 5.2) that is slightly upshifted by the dynamic ramp rate compared to the quasi–isothermal heating (average rate of 1ºC min^{-1}) used in the FTIR and σ_{dc} measurements. The T_p is 220ºC. For MHA ligand, the T_p is 170^{0}C which is 50ºC lower than MHA_{salt}–Au NPs. FTIR shows the elimination onset at 155ºC (fig. 4.4 and 4.5), and the corresponding DSC exotherm peaks at 165ºC (fig. 5.2). This indicates that the bottleneck step in the coalescence of the metal NP film is elimination of the protection shell. Hence the lower T_p of MHA_{acid}–Au is to a weaker intermolecular interaction compared to the ionized tail group rather than differences in chain conformation.

Mixed ligand shell of MHA and hydrophobic BT ligands shows T_p at ≈ 190–200ºC even at large MHA dilutions while pure BT–Au NPs show T_p ≈ 130ºC. During annealing, BT desorbs first over ≈ 120–160ºC similar to pure BT–Au NPs, followed by overlapping loss of MHA_{acid} and MHA_{salt} over 140–200ºC. T_p occurs near the complete loss of MHA, and so 10 mol% in the shell can remarkably elevate T_p by 60–70ºC. This suggests an interesting ionic, hydrogen bonding and/or *inter*-NP bonding between MHA on neighboring NPs that hold apart the Au cores suppressing coalescence.

5.3.5 T_p: Sparse ligand shells.

Sparse ligand shells can introduce a built-in porosity that facilitates a lowering of the T_p below the temperature required for the elimination of a functionalized shell, while retaining good solvent characteristics. This can be achieved in a simple way by templated assembly of the shell, as described in chapter 3. For sparse ionic monolayer-protection however, T_p can be obtained below the temperature of elimination of the shell. This occurs because as the shell becomes sparse enough, sintering between adjacent cores can occur through the porous shell. This is one of the reasons for the signatures of key functional groups are still active in the FTIR ligand shell transformation spectra (fig. 4.4 and 4.5). A mixture of MHA and hydrophilic MPL ligands give T_p ≈ 145ºC, while providing sufficient surface ion density for high dispersibility in water. As the density of the ionic monolayer grows, e.g. through a mixture of MHA and ω-mercaptobutanol (MBL) the T_p increases to 170–190ºC, and the DSC exotherm upshifts correspondingly to 175ºC (fig. 5.2).

5.3.6 T_p: Role of surface melting?

For Au NPs suspended in vacuum, molecular dynamic simulations have revealed the occurrence of enhanced mobility and loss of correlation of the surface atoms at a “surface-melting”

phenomenon well below T_m.[12, 33-35] However, for ligand-protected NPs, the covalent bonding of the ligand molecules may have a significant effect on the surface atoms, and the role of surface melting is unclear. Because the structure at the Au–S head group is practically identical for some of these members, we can also rule out surface melting as the driving mechanism for this ligand shell elimination. Otherwise these members should exhibit similar T_p irrespective of the ligand shells structure effects! Therefore control of the ligand shell structure is central to controlling T_p. Once the NP becomes partially "bare", core coalescence occurs by direct contact of the nanocores.

5.4 Summary

The underlying mechanism for the coalescence of the metal NPs therefore is due to contact between "bare" surfaces of the NP exposed by the volatilization or displacement of the dispersant shell, and has nothing to do with the nanosize effects. The driving force for the coalescence is the surface-energy reduction of the nano-metal made possible by the elimination of the intervening ligand shell. The key to reduction of the coalescence temperature therefore lies in moderating the stability of this ligand shell and not in generating smaller nanoparticles. Developing refined means to control the properties and disintegration of the ligand shell will be most directly beneficial to the nano-metal ink technologies.

5.5 Reference:

1. Buffat, P. and J.P. Borel, *Size effect on the melting temperature of gold particles.* Phys. Rev. A, 1976. 13: p. 2287-2296.
2. Castro, T., Reifenberger, R., Choi, E., Andres, R. P., *Size-dependent melting temperature of individual nanometer-sized metallic clusters.* Phys. Rev. B, 1990. 42: p. 8548-8556.
3. Coombes, C.J., *The melting of small particles of lead and indium.* J. Phys. F: Metal Phys., 1972. 2: p. 441-449.
4. Lai, S.L., Guo J.Y., Petrova V.V., Ramanath G, Allen L.H., *Size-dependent melting properties of small tin particles: nanocalorimetric measurements.* Phys. Rev. Lett., 1996. 77: p. 99-102.
5. Takagi, M., *Electron-diffraction study of liquid-solid transistion of thin metal films.* J. Phys. Soc. Jpn., 1954. 9: p. 359-363.
6. Allen, G.L., R.A. Bayles, W.W. Gile and W.A. Jesser, *Small particle melting of pure metals.* Thin Sold Films, 1986. 144: p. 297-308.
7. Couchman, P.R. and W.A. Jesser, *Thermodynamic theory of size dependence of melting temperature in metals.* Nature, 1977. 269: p. 481-483.
8. Qi, W.H. and M.P. Wang, *Size effect on the cohesive energy of nanoparticle.* J. Mater. Sci. Lett., 2002. 21: p. 1743-1745.
9. Sun, C., Y. Wang, and B. K. Tay, *Correlation between the melting point of a nanosolid and the cohesive energy of a surface atom.* J. Phys. Chem. B, 2002. 106: p. 10701-10705.
10. Frenken, J.W.M. and J.F. van der Veen, *Observation of surface melting.* Phys. Rev. Lett., 1984. 54: p. 134-137.
11. Sakai, H., *Surface-induced melting of small particles.* Surf. Sci., 1996. 351: p. 285-291.
12. Ercolessi, F., W. Andreoni, and E. Tosatti, *Melting of small gold particles: mechanism and size effects.* Phys. Rev. Lett., 1991. 66: p. 911-914.
13. Dearden, A.L., Smith P.J., Shin D.-Y., Reis N., Derby B., O'Brien P., *A low curing temperature silver ink for use in ink-jet printing and subsequent production of conductive tracks.* Macromol. Rap. Commun., 2005. 26: p. 315-318.
14. Fuller, S.B., E.J. Wilhelm, and J.M. Jacobson, *Ink-jet printed nanoparticle microelectromechanical systems.* J. Microelectromech. Syst., 2002. 11: p. 54 - 60.
15. Gamerith, S., A. Klug, H. Scheiber, U. Scherf, E. Moderegger, E.J.W. List, *Direct ink-jet printing of Ag-Cu nanoparticle and Ag-precursor based electrodes for OFET applications.* Adv. Funct. Mater., 2007. 17: p. 3111-3118.

16. Greer, J.R. and R.A. Street, *Mechanical characterisation of solution-derived nanoparticle silver ink thin films.* J. Appl. Phys., 2007. 101: p. 103529(1-5).
17. Ko, S.H., J. Chung, H. Pan, C.P. Grigoropoulos and D. Poulikakos, *Fabrication of multilayer passive and active electric components on polymer using inkjet printing and low temperature laser processing.* Sensors and Actuators A: Physical, 2007. 134: p. 161-168.
18. Li, Y., Y. Wu, and B.S. Ong, *Facile synthesis of silver nanoparticles useful for fabrication of high-conductivity elements for printed electronics.* J. Am. Chem. Soc., 2005. 127: p. 3266-3267.
19. Wu, Y., Y. Li, and B.S. Ong, *Printed silver ohmic contacts for high-mobility organic thin-film transistors.* J. Am. Chem. Soc., 2006. 128: p. 4202-4203.
20 Wu, Y., Y. Li, B.S. Ong, P. Liu, S. Gardner, B. Chiang, *High-performance organic thin-film transistors with solution-printed gold contatcs.* Adv. Mater., 2005. 17: p. 184-187.
21. Zhao, N., M. Chiesa, and H. Sirringhaus, *Self-aligned inkjet printing of highly conducting gold electrodes with submicron resolution.* J. Appl. Phys., 2007. 101: p. 064513.
22. Hostetler, M.J., J.E. Wingate, C.J. Zhong, J.E. Harris, R.W. Vachet, M.R. Clark, J.D. Londono, S.J. Green, J.J. Stokes, G.D. Wignall, G.L. Glish, M.D. Porter, N.D. Evans, and R.W. Murray, *Alkanethiolate gold cluster molecules with core diameters from 1.5 to 5.2 nm: Core and monolayer properties as a function of core size.* Langmuir, 1998. 14: p. 17-30.
23. Nishida, N., M. Hara, H. Sasabe and W. Knoll, *Thermal desorption spectroscopy of alkanethiol self-assembled monolayers on Au(111).* Jpn. J. Appl. Phys., 1996. 35: p. 5866-5872.
24. Nuzzo, R.G., B.R. Zegarski, and L.H. Dubois, *Fundamental studies of the chemisorption of organosulfur compounds on Au(111): Implications for molecular assembly on gold surfaces.* J. Am. Chem. Soc., 1987. 109: p. 733-740.
25. Lavrich, D.J., S.M. Wetterer, S.L. Bernasek and G. Scoles, *Physisorption and chemisorption of alkanethiols and alkyl sulfides on Au(111).* J. Phys. Chem., 1998. 102: p. 3456-3465.
26. Steudel, R., *properties of sulfur-sulfur bonds.* Angew. Chem. Int. Ed., 1975. 14: p. 655-720.
27. Dick, K., T. Dhanasekaran, Z. Zhang, and D. Meisel, *Size-dependent melting of silica-encapsulated gold nanoparticles*, J. Am. Chem. Soc., 2002. 124: p. 2312-2317.
28. Sambles, J.R., *An electron microscope study of evaporating gold particles; the Kelvin equation for liquid gold and the lowering of melting point of solid gold particles.* Proc. R. Soc. Lond. A, 1971. 324: p. 339-351.
29. Huang, D., F. Liao, S. Molesa, D. Redinger, and V. Subramanian, *Plastic-compatible low resistance printable gold nanoparticle conductors for flexible electronics.* J. Electrochem. Soc., 2003. 150: p. G412-G417.
30. Ashcroft, N.W. and D.N. Mermin, *Solid State Physics*. 1976, Philadelphia: Saunders College.

31. Sivaramakrishnan, S., B.T. Anto, and P.K.H. Ho, *Optical modeling of the plasmon band of monolayer-protected nanometal clusters in pure and in polymer matrix thin films as a function of heat treatment.* Appl. Phys. Lett., 2009. 94: p. 091909.
32. Sivaramakrishnan, S., Chia P.J., Yeo Y.C., Chua L.L., and Ho P.K-H., *Controlled insulator-to-metal transformation in printable polymer composites with nanometal clusters.* Nat. Mater., 2007. 6: p. 149-155.
33. Arcidiacono, S., N.R. Bieri, D. Poulikakos, C.P. Grigoropoulos, *On the coalescence of gold nanoparticles* Int. J. Multiphase Flow 2004. 30: p. 979–994.
34. Lewis, L.J., P. Jensen, and J.L. Barrat, *Melting, freezing, and coalescence of gold nanoclusters.* Phys. Rev. B, 1997. 56: p. 2248-2257.
35. Kofman, R., P. Cheyssac, A. Aouaj, Y. Lereah, G. Deutscher, T. Ben-David, J.M. Penisson and A. Bourret, *Surface melting enhanced by curvature effects.* Surf. Sci., 1994. 303: p. 231-246.

Outlook

The work in this thesis addresses a central question on how to control the insulator to metal transformation temperature T_p of nanometal inks. We have demonstrated by templating sparse ionic monolayer ligand shells, the T_p can be reduced to a lowest ever reported value of 150ºC for water and polar solvent dispersible nanometal inks, at par with commercial standards, which is an essential requirement for plastic electronics applications. Further scope of this work lies on the study of behaviour of T_p with respect to anneal time on an isothermal process. This enables us to widen the scope of our understanding about T_p. Currently we are working on this "Time–Temperature–Transformation (TTT)" of nanometal inks to understand how T_p behaves with isothermal annealing process.

Secondly, our work show that the T_p can be tuned by controlling the inter-molecular ionic forces, hydrogen bonding and van der Waals forces for similar core diameter metal NPs, in chapter 4. This enables us to address the fundamental understanding of nanometal core–core coalescence in NP meal films. We demonstrate the thermodynamic size effect and surface melting mechanisms are the manifestations of coalescence process in the monolayer protected metal NP films, in chapter 5. The invariance of T_p with respect to core diameter, together with differential scanning calorimentry measurements, clearly demonstrates the coalescence is a ligand desorption dominated process.

List of publications

Publications arising from this work

1. B.T. Anto, S. Sivaramakrishnan, L.L. Chua, and P.K.H. Ho, Hydrophilic Sparse Ionic Monolayer-Protected Metal Nanoparticles: Highly Concentrated Nano-Au and Nano-Ag Inks that can be Sintered to Near-Bulk Conductivity at 150 °C, *Adv. Funct. Mater.* 20, 296 (2010)
2. B.T. Anto, L.L. Chua, S. Sivaramakrishnan, L.Y. Wong, R.Q. Png, P.K.H. Ho, Printable Metal Nanoparticle Inks for Thin-Film Metallization: Physicochemical Aspects, Handbook of nanophysics, Ed: Klaus D. Sattler, Taylor & Francis (CRC Press), 2010. (*invited book chapter*)

Publications not related to this thesis

3. S. Sivaramakrishnan, B.T. Anto, and P.K.H. Ho, Optical modeling of the plasmon band of monolayer-protected nanometal clusters in pure and in polymer matrix thin films as a function of heat treatment, *Appl. Phys. Lett.* 94, 091909 (2009)

Patent Applications

4. P.K.H. Ho, L.L. Chua, R.H. Friend, B.T. Anto, L.Y. Wong and R.Q. Png, "Metal nanoparticle inks", U.S. Provisional Application No. 61/267,498 (2009)
5. P.K-H. Ho, L.L. Chua, R.H. Friend, J.C. Tang, B.T. Anto, R.Q. Png and P.J. Chia, "Sterically Hindered Photocrosslinkers", U.S. Provisional Application No. 61/266,561 (2009)

Conference presentations

6. B.T. Anto, S. Sivaramakrishnan, L.L. Chua, P.K.H. Ho, Sparse monolayer protected metal nanoparticles: a general route to high water dispersibility and low solid-sate coalescence temperature, ICMAT 2009, Singapore (poster presentation)